A MEASUREMENT OF THE e/π RATIO DIFFERENCE BETWEEN SHORT (250 ns) AND LONG (2.2 μs) INTEGRATION TIMES WITH THE D0 URANIUM-LIQUID ARGON CENTRAL CALORIMETER

By

Bo Pi

A DISSERTATION

Submitted to
Michigan State University
in partial fulfillment of the requirements
for the degree of

DOCTOR OF PHILOSOPHY

Department of Physics and Astronomy

1992

Abstract

A Measurement of the e/π Ratio Difference Between Short (250 ns) and Long (2.2 μs) Integration Times with the D0 Uranium-Liquid Argon Central Calorimeter

By

Bo Pi

The difference of the ratios of the high energy electron and pion responses (e/π) in the D0 Uranium-liquid Argon central calorimeter is measured using the D0 calorimeter trigger readout (short integration time: 250 ns) and precision readout (long integration time: 2.2 μs). This measurement found a 5% difference in the e/π ratio between short and long integration times, with estimated uncertainty of 2.3%.

This dissertation is dedicated to the heroic students and civilians who died in Beijing on June 4, 1989.

Acknowledgments

There are many people who provided support and help to make this work possible. In particular, I would like to thank my advisor Maris Abolins, for his wise advise and patient guidance, throughout many years of my graduate school. I also would like to say special thanks to Dan Edmunds and Philippe Laurens, for their friendship and caring support.

I would like to thank all my friends at D0 test beam: Bob Hirosky, John Borders, Scott Snyder, Terry Heuring, Terry Geld, Marcel Demarteau, Welanthantri Dharmaratna, Mike Tartaglia and Dan Owen, whose hard work made this research possible.

Special thanks to Rich Astur, Steve Jerger, Kate Frame and John Borders, who spent countless hours reading and correcting this dissertation. Special thanks to Carol Edmunds and Sarah Laurens for those great dinners. I also would like thank Dolores Foote, Teresa Thomas and Lisa Ruess whose support made my school years easier.

I would like to thank T. D. Lee and the men and women who worked to make the CUSPEA program possible, and without whom, my graduate study here at Michigan State University would not have been possible. I would also like to thank the National Science Foundation for its continued support throughout these years.

Most of all, I would like to thank my parents, to whom I owe my life and wisdom.

Table of Contents

List of Figures

List of Tables

Chapter 1
Introduction

Over the last 15 years, there has been a trend by which the high energy physics experiments have changed from the spectrometer to the calorimeter. Some major discoveries, e.g. the existence of the intermediate vector boson W and Z, became possible as a result of this development. The new generation of experiments increases the emphasis on the calorimeter more than ever, and the performance of the calorimeter becomes the major factor in discriminating experiments. This dissertation is a study of one of the most important issues affecting calorimeter performance: the ratio of the electron and pion responses (e/π), using the D0 Uranium-liquid Argon central calorimeter. A short introduction will be given on the Fermi National Accelerator Laboratory and the D0 experiment.

The Fermi National Accelerator Laboratory has the highest energy proton (p) anti-proton ($\bar{p}$) collider in the world[1]. The accelerator has two operational modes: fixed target and collider. When the accelerator operates in the fixed target mode, it provides a 800 GeV proton beam to the fixed target experiments at the rate of $2\text{x}10^{13}$ protons/second. In the collider mode, the accelerator can accelerate and store both proton and anti-proton beams at 900 GeV in the Superconducting Tevatron ring, and steer them to a head-on collision. The collision creates a center of mass energy of 1.8 TeV. The luminosity has reached a maximum of $1.5\text{x}10^{30}/(cm^2 \cdot s)$, and is expected to reach $5.0\text{x}10^{30}/(cm^2 \cdot s)$ in 1992. There are a total of 6 interaction points (A B C D E

F) around the accelerator ring. Low beta focus magnets have been installed at two of these points, B0 and D0, in order to get the maximum luminosity. Two big experiments, CDF (B0) and D0, are installed at these interaction areas.

The D0 experiment[2](Figure 1.1), designed with very specific physics goals in mind, utilizes the most recent developments in detector technology. The detector's performance is greatly improved from previous collider detectors. The D0 detector was designed to provide optimal measurement of leptons (electrons, muons and their neutrinos) and hadrons (jets) produced in high-energy collisions of protons and anti-protons at Fermilab. It is based on a Uranium- liquid Argon calorimeter organized in projective towers surrounding the interaction region over nearly the full 4π solid angle. The fine longitudinal segmentation of the calorimeter helps the electron discrimination and energy measurement in the large background of pions. A tracking system also covers nearly the full 4π solid angle of the interaction region. A transition radiation detector (TRD) is built inside the tracking system, to further improve the identification of electrons. Neutrinos, which escape undetected, reveal their presence in the form of an imbalance in the transverse momentum summed over the full detector, and the quality of this measurement is crucially dependent on the good resolution and uniformity of the calorimeter. Muons, on the other hand, are identified by their characteristic ease of penetration through the thick calorimeter as well as through the layers of iron comprising the toroidal magnetic spectrometer outside the calorimeter. The latter provides a measurement of the muon's transverse momentum over much of the solid angle, including a determination of the sign of its charge.

The calorimeter is the central part of the detector system. Its performance is critical to many physics measurements of the experiment. Because of its importance, we have done three test beam experiments to expose different parts of the calorimeter to high

energy electron and pion beams. These test beam experiments gave us opportunities to study the calorimeter response in great detail.

The design of the D0 calorimeter is based on the most recent knowledge of the hadronic showers. In the past several years, we have begun to understand the various processes involved in a hadronic shower at a fairly detailed level. However, in order to quantify this knowledge, precise experimental results are needed. It has been predicted that the response of hadron showers in neutron rich material (like Uranium) will increase as a function of the time over which the calorimeter signal is integrated. The existence of this phenomenon has been verified by several groups[29,30,31], and in the case of Uranium-liquid Argon calorimeters, the HELIOS collaboration is the only experiment that has done a study on this subject[14]. But its measurement are not very precise. This dissertation is a study of the time dependence of a hadronic shower in the D0 Uranium-liquid Argon calorimeter. The e/π ratio of the D0 Uranium-liquid Argon calorimeter has been measured with the fast calorimeter trigger electronics (250ns integration time) and the precision calorimeter electronics (2.2μs integration time), and with particle energies ranging between 15 and 150 GeV.

The D0 calorimeter, as well as the properties that affect the e/π ratio, will be described in the next Chapter. Chapter 3 is a description of the D0 calorimeter electronics system. It will include a discussion of the difficulties with the fast calorimeter trigger electronics, as well as the solution. Chapter 4 is a description of the D0 calorimeter test beam facility and the configurations of the two test beam runs in the period 1990 to 1992. The analysis of the 1991-1992 (load-two) test beam run data will be presented in Chapter 5, including discussions of the various corrections applied to the final e/π ratio measurement. In Chapter 6, the final result of the e/π ratio measurement with different integration times will be presented, as well as a description of the detector Monte Carlo simulation and a discussion of the results.

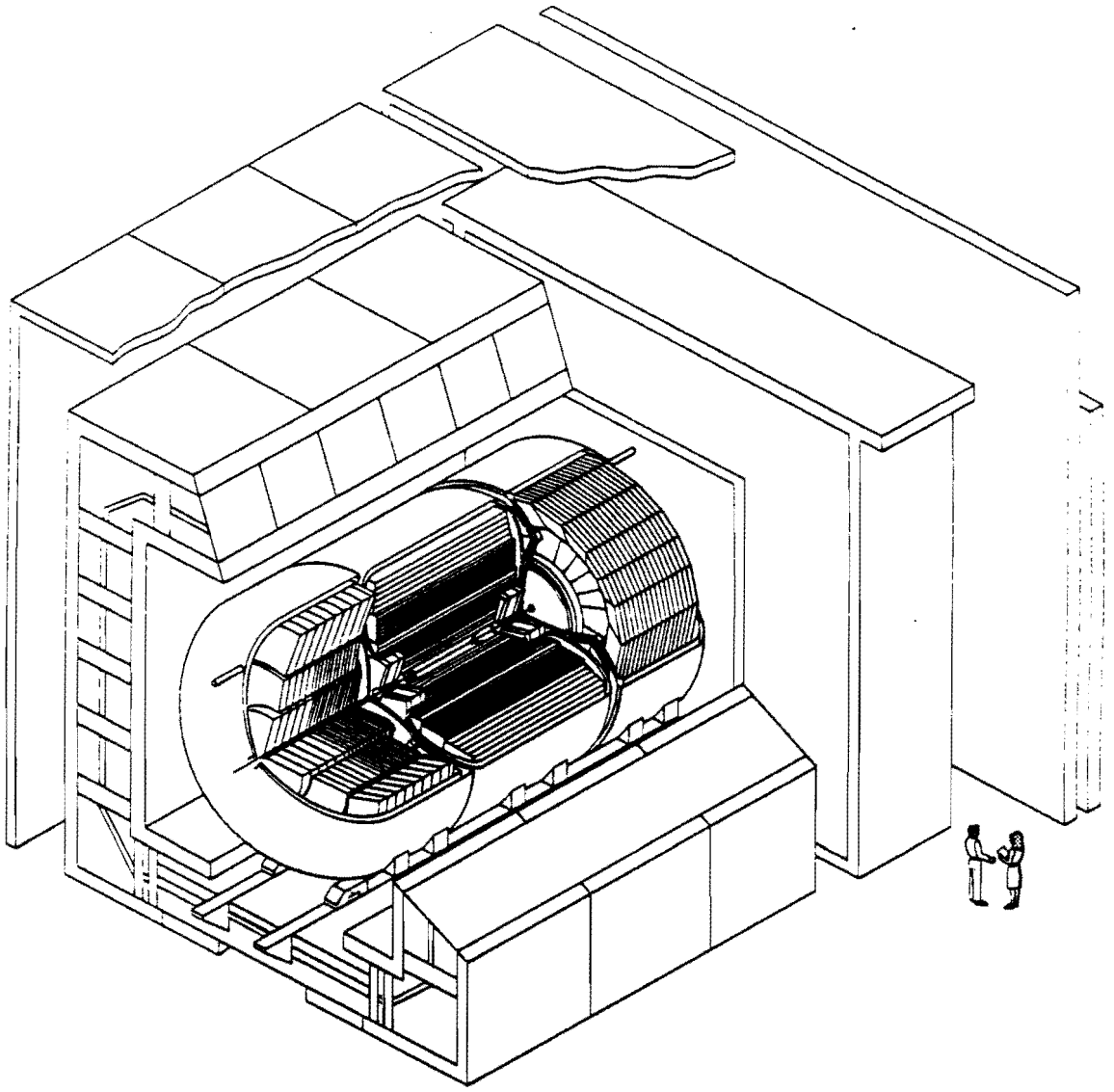

Figure 1.1 D0 detector

Chapter 2
D0 calorimeter

2.1 General calorimeter principles

Conceptually, a calorimeter is a block of matter that intercepts a high energy particle and has sufficient thickness to cause the particle to interact and deposit all its energy inside the detector volume in a subsequent cascade or "shower" of increasingly lower energy particles. Figures 2.1 and 2.2 show a GEANT[3] Monte Carlo simulation of a 50 GeV electron and pion shower in the D0 central calorimeter, and they demonstrate the complexity of high energy particle showers. Eventually, most of the incident energy is dissipated and appears in the form of heat. Some (usually a small fraction) of the deposited energy goes into the production of a more practical signal (e.g., scintillation light, ionization charge). It is an important feature of a calorimeter that this signal be proportional to the initial energy. In principle, the uncertainty in the energy measurement is governed by statistical fluctuations in the production of the detectable signals (e.g. ionization charge), and the fractional resolution (σ/E) improves with increasing energy (E) as $\sqrt{E}$. In Chapter 1, it was noted that calorimetric detectors offer many other attractive capabilities, apart from the energy response. These properties are listed as following[8]:

A) Calorimeters are sensitive to neutral as well as charged particles.

B) The size of the detector scales logarithmically with particle energy E, whereas for magnetic spectrometers the size scales with particle momentum $\sqrt{P}$.

C) With segmented detectors, information on the shower development allows precision measurements of the position and the angle of the incident particle.

D) The differences in the patterns of energy deposition of electrons, muons, and hadrons can be exploited for particle identification.

E) The fast time response allows operation at high interaction rates, and the patterns of energy deposition can be used for real-time event selection.

2.2 High energy particle shower in the calorimeter

In this section, I will briefly summarize the mechanisms of high energy particle interactions with materials.

2.2.1 High energy electromagnetic shower.

The electromagnetic (EM) interacting particles include photon (γ), electron (e^-) and positron (e^+). At high energy (kinetic energy E_k> a few hundred MeV), photon, electron and positron showers are very similar except for the first interaction. For the high energy photon the first interaction will be to produce an electron and positron pair. For the high energy electron and positron, the first interaction will likely be bremsstrahlung which produces high energy photons. In general, the photons lose their energy through the following processes:

A) Pair (e^+, e^-) production.

B) Compton scattering.

C) Photoelectric effect.

The electrons and positrons lose their energy through:

A) Bremsstrahlung.

B) Ionization.

C) Multiple scattering.

The EM shower is a chain of these interactions, and it will keep on going until all the energy of the initial particle is dissipated. All of these processes are governed by one of the best established theoretical framework in physics: quantum electrodynamics, and they can be calculated from theoretical formulas with good precision.

2.2.2 High energy hadronic shower

For hadronic interacting (HD) particles (hadrons: pions, protons, etc.), the interactions with material are more complicated than electromagnetically interacting particles. When a high energy hadron hits a block of matter, the hadron will interact with one of its nuclei. In this process, mesons are usually produced (π, K, etc.), and these particles may go on to produce a chain of interactions themselves. Some of the particles produced in a hadron shower interact exclusively electromagnetically (e.g. π^0, η). Therefore, hadron showers in general contain a component that propagates electromagnetically. The fraction of the initial hadron energy converted into the electromagnetic component may vary strongly from event to event depending on the detailed processes occurring in the early phase of the shower development. The hadrons (e.g. proton, π^+, π^-) produced in a hadron shower interact with nuclei and transfer a part of their energy to the nuclei. The excited nuclei will release their energy by emitting a certain number of nucleons and low-energy gammas (γ's). This chain of nuclear reactions will keep on going until the energies of the hadrons fall below about 1 GeV. Then hadrons will lose their energy mostly through ionization. However, there is one exception, that is neutrons. Since a neutron is not a charged particle, it does not lose energy by ionization. These neutrons, created in the hadron showers, lose their energy exclusively through nuclear processes, i.e. either through elastic scattering off nuclei, or through capture by nuclei. The nuclei that capture the neutrons will be in an excited state, and will lose their energy either through fission or simply by emitting γ's. Fission could create more low energy neutrons and γ's.

The calorimeter signal of a hadron shower will come from the contributions of all these different processes. Some of these nuclear processes take a long time (~ μs) to finish. The theoretical calculations of these strong interaction processes are not as well understood as electromagnetic processes. Experimental results to further understand these processes in hadron showers are still needed.

2.3 Sampling fraction

In order to be able to measure the energy of an incident particle in a sampling calorimeter like D0, one has to understand the sampling fraction, or the fraction of energy deposited in the active layers through the ionization process, as well as the efficiency of the detection technique. The latter factor is determined by the saturation effect[1] and the amplifier's efficiency in detecting the signal. For the liquid Argon calorimeter, the source of the signal is the ionization charges in the liquid Argon gaps. The first factor is determined by the structure of the sampling calorimeter, the materials chosen, and the interaction cross-sections of various particles interacting with these materials. I will discuss these factors in the following sections.

Since the detectable signals in the calorimeter are produced by the ionization of various charged particles, the calorimeter response of a minimum-ionizing particle (mip) is used as a scale for the calorimeter signal. The mip is a particle that interacts with materials exclusively through the ionization process, and its energy loss per unit of mass is minimum[33]. Thus, the saturation effect is minimized. Many measurements and calculations have been done for various materials to determine their mip energy loss ($\frac{dE}{dx}$), and there is a standard table of $\frac{dE}{dx}$ for various materials. In practice, the $\frac{dE}{dx}$'s of the active and passive materials are used to determine the sampling fractions of

[1] The saturation effect in liquid Argon ionization calorimeter is caused by the charge recombination in the drifting path. It causes the detector to lose signal. It is sensitive to the applied high voltage.

a calorimeter. The active layer is the sensitive layer in which energy deposited in the layer is detected, and the passive layer is the layer of inactive materials. The sampling fraction (the mip sampling fraction) is defined as:

$$S_{mip} = \frac{\frac{dE}{dx}[one\ active\ layer]}{\left\{\frac{dE}{dx}[one\ active\ layer] + \frac{dE}{dx}[one\ passive\ layer]\right\}} \tag{2.1}$$

The low energy muon is the a known particle that behaves like a minimum-ionizing particle. Most detectors use low energy muon response to verify their sampling fractions. Throughout this dissertation, the mip sampling fraction is applied to weight the calorimeter signals unless otherwise noted.

2.4 The e/h signal ratio

For a given calorimeter, hadron showers are generally detected with an energy resolution that is worse than the electromagnetic showers. There are several reasons for the poorer hadron energy resolution. First, after the early phase of hadron showers, the initial energy of the hadrons is converted into the pure electromagnetic component (EM), and the pure hadronic component (HD). For the HD component of hadron showers, some fraction of the energy will disappear without contributing to the calorimeter signal. This is, for example, the energy spent in breaking up the nuclei, and the energy of some particles (ν, μ, and a fraction of neutrons) that are created in the showers which escape from the detector. This will cause the calorimeter response to the HD component to have a much broader distribution than the EM component, and the average response to the EM and the HD components to be different. Furthermore, the fraction of the initial hadron energy converted into the EM component fluctuates event by event; this and the unequal responses between the EM and HD components of the hadron showers further worsen the hadron energy resolution.

The calorimeter response difference between the EM and HD components of the hadron showers is characterized by the e/h ratio, defined as[10]:

$$\frac{e}{h} = \frac{(response\ of\ EM\ components)}{(response\ of\ pure\ hadronic\ components)}$$

In order to understand the $\frac{e}{h}$ ratio of a calorimeter, I will demonstrate a simple analysis of the calorimeter response to various secondary particles in a hadron shower[11]:

(a) High energy photons, which arise mainly from π^0 decays, and form the EM shower component.

(b) Ionizing hadrons (charged pions, kaons, protons, etc.).

(c) Soft neutrons.

(d) Soft γs from the nuclear processes (fission, nuclear de-excitation, etc.)..

Items (b), (c) and (d) are the pure HD components.

The mip response will be used as a scale. Relating the response of the four mentioned types of particles to mip's, the $\frac{e}{h}$ ratio can be written as[11]:

$$\frac{e}{h} = \frac{e/mip}{f_{ion}\, ion/mip + f_n\, n/mip + f_\gamma\, \gamma/mip} \qquad (2.2)$$

where f_{ion}, f_n, and f_γ are the average fractions of the energy in the pure hadronic component that are in the forms of ionizing hadrons, neutrons and nuclear γs. The calorimeter responses to various terms of Formula 2.2 will be briefly discussed in the next section. A detailed discussion can be found in [11].

2.4.1 The response to high energy electrons and photons (e/mip)

The detectable signal of the high energy electrons and photons comes from ionization in the active layers by the electrons and positrons generated in the EM shower

development. Although one might expect this signal to be equal to the mip signal, in practice they are not. The reason for this is the following.

For the relativistic charged particle with charge e, the ionization energy loss per unit of mass is given by the Bethe-Bloch equation[33]:

$$-\frac{dE}{dx} = 4\pi N_A r_e m_e c^2 \frac{Z}{A}\frac{1}{\beta^2}\left[\ln\left(\frac{2m_e c^2\gamma^2\beta^2}{I}\right) - \beta^2 - \frac{\delta}{2}\right] \tag{2.3}$$

where $\beta = \frac{v}{c}$, $\gamma = \left(1-\beta^2\right)^{-1/2}$.

In this formula, Z, A and I refer to the atomic number, the atomic weight and ionization constant in the target material, respectively, m_e, and r_e are the mass and the classical radius of the electron, v is the velocity of the incident particle, N_A is Avogadro's number, and δ is a small density effect correction. Thus the ionization energy loss per unit mass is proportional to $\frac{Z}{A}$, with some weak dependence on the other properties of the material. Because $\frac{Z}{A}$, is relatively constant, $\frac{dE}{dx}$ is approximately constant also.

Whereas, in the EM shower there are a large number of soft γs (E_K<1 MeV) produced, and the dominant process by which these soft γs to generate a detectable signal is to transfer their energy to electrons through the photo-electric process. But the cross section of the photo-electric process with K shell electrons is proportional to Z^5 [4,5]:

$$\sigma_K \propto Z^5\left(\frac{m_e c^2}{\hbar\omega}\right)^{7/2}$$

where the Z is the charge of matter, $\hbar\omega$ is the photon energy, and m_e is the electron reset mass. This means that the photo-electric process happens primarily in the high Z materials (usually passive materials) of a sampling calorimeter. The low energy photo-electrons have a very short mean free path, so they deposit their energy near where they

are produced. Only when these photo-electrons are produced near the surface of the passive materials will they be able to travel to the active material and create detectable signals.

Because of this difference in interaction cross-sections, a sampling calorimeter using materials of very different Z values in its passive and active layers will show different electron and mip response. In general, if $Z_{passive} > Z_{active}$, then $e/mip < 1.0$, and if $Z_{passive} < Z_{active}$, then $e/mip > 1.0$.

2.4.2 The response to ionizing hadrons (*ion/mip*)

In the high-energy hadron shower, the average fraction of the energy in the pure hadronic component deposited in the form of ionization is roughly[11]

$$f_{ion} \doteq \frac{Z}{A}, \tag{2.4}$$

where Z and A are the charge and atomic weight of the matter.

The simple reason for this formula is that most of the hadrons produced in a high energy hadron shower are protons and neutrons, and the probability of knocking out protons in a matter goes approximately as $\frac{Z}{A}$.

For Uranium, about 40% of the energy in the pure hadronic component is deposited in the form of ionization. The charged hadronic component is dominated by protons (70-75%)[11]. The remaining contribution comes from charged pions, kaons, etc.. The ionization energy density deposited by these charged hadrons is greater than mip's, thus the *ion/mip* signal ratio of a calorimeter is very dependent on the material of the calorimeter. For a practical calorimeter with saturation readout material (like liquid Argon, etc.), the *ion/mip* signal ratio has a range of 0.85 - 1.0[21].

2.4.3 The response to the neutrons (n/mip)

A large portion of the energy in the pure hadronic component is carried by neutrons. There are more neutrons than any charged hadronic particles produced in hadronic showers. This is simply because there are more neutrons in most nuclei. Because the neutron has no charge, it can not directly create a detectable signal through ionization as the proton does. The processes by which neutrons are produced and lose their energy[10,11] will be examined in the following.

The neutrons in the high energy hadron shower are produced through nuclear processes. Initially, fast neutrons (E_k~GeVs) are produced through nuclear processes induced by high energy hadronic particles (charged pions and protons etc.). These fast neutrons may develop quite complicated showers themselves and produce more neutrons. These neutrons will lose their energy by elastic and inelastic scattering off the nucleus. Once the neutrons slow down to soft neutrons (Ek ~ a few MeV), nuclear fission may dominate the neutron interaction processes. When the neutrons are further slowed down (Ek< MeV), nuclear neutron capture processes will dominate. In each of these processes, there is energy released in the form of soft γ's, and more neutrons may be produced.

In a calorimeter using materials containing hydrogen, the neutrons will lose about half their energy each time they scatter off a proton (hydrogen nucleus), and generate detectable signals through proton ionization. As the atomic number of the material goes up, this form of energy transfer decreases very rapidly. The neutrons take longer to lose their energy to become soft neutrons. In the case of Uranium-liquid Argon, the contribution of neutron-nucleus scattering is negligible. However the presence of Uranium significantly increases the number of neutrons in the hadron shower[10,11,12], and the soft γs produced from neutron-nucleus processes (fission, neutron capture, etc.)

will make significant contributions to the total detectable signal. On the other hand, the processes of slowing down and capturing the neutrons take a relatively long time, on the order of μs[18]. In order to detect the signals from these contributions, the calorimeter has to have an integration time on the order of μs.

In summary, the *n/mip* signal ratio depends on the materials of the calorimeter and the signal integration time.

2.4.4 The response to nuclear gamma's ($\gamma/mips$)

The γs from the nuclear processes induced by charged hadrons and neutrons are in the energy range of a few MeV. These soft γs are produced mostly in the passive materials (Uranium, etc.). Their contribution to the detectable signal is through the same photo-electric process as the soft γs in EM showers (Section 2.4.1). If a high Z material is used as the passive material and a low Z material is use for the active material, this form of signal is suppressed as described in Section 2.4.1.

2.4.5 The experimental concerns

Because all hadronic particle showers contain pure electromagnetic and pure hadronic components. In practice, the calorimeter response of the pure electromagnetic component "e" is measured with high energy electrons, and the response of the pure hadronic component "h" is measured with high energy charged pions. For high energy hadron showers the relation between the e/h ratio and the e/π ratio is[11]

$$\frac{e}{\pi(E)} = \frac{e/h}{1-\langle f_{em}(E)\rangle[1-e/h]} \tag{2.5}$$

where $$\langle f_{em}(E)\rangle = 0.1 \ln E(GeV). \tag{2.6}$$

This is a reasonable approximation in the energy range from 10 to 100 GeV. From now on, I will use the e/π ratio to represent the e/h ratio.

The deviation of e/π from unity will cause a calorimeter's hadronic response to have a non-Gaussian energy distribution, the energy resolution will not scale with $\sqrt{E}$ and will have a large constant term[2], and the calorimeter signal will not be proportional to the hadron energy (non-linearity)[9,11]. With experimental energies becoming larger and larger, the deviation from $\frac{e}{\pi}=1$ becomes one of the most important factors limiting a calorimeter's performance. In today's $p-\bar{p}$ hadron collider experiments, being able to precisely measure the energy of multiparticle jets (including electromagnetic and hadronic particles) becomes one of the most important factors influencing collider detector design.

2.5 D0 Uranium-liquid Argon (U/LAr) sampling calorimeter

In the past 10 years, much progress has been made in understanding the factors limiting calorimeter performance. The D0 calorimeter was designed on the basis of this new knowledge. The D0 calorimeter is built with Uranium as the absorber and liquid Argon as the active material. The choice of this combination gives maximum density, ease of calibration, straight forward projective tower segmentation, and good energy resolution. From the early studies[19, 29], the Uranium-liquid Argon combination gives nearly equal electromagnetic and hadronic energy responses. Also, the high density of Uranium is vital to the design, because it allows the overall dimensions of the detector to be kept as small as possible.

---

[2] The calorimeter energy resolution can be parametrized as $\left(\frac{\sigma}{E}\right)^2 = C^2 + \frac{S^2}{E} + \frac{N^2}{E^2}$, where C is the constant term, S is the sampling term, and N is the external noise term. An ideal calorimeter should have C=0 and N=0.

2.5.1 The e/h ratio of Uranium-liquid Argon calorimeter

One of the major reasons that D0 chose the Uranium-liquid Argon combination for its calorimeter is that it gives an e/π ratio close to one. There are several effects which cause this ratio to be close to unity:

a) Because of the large Z difference between Uranium and liquid Argon, the response of the EM particles is suppressed relative to the mip (Section 2.4.1). Our test beam measurement shows that e/mip ~ 0.7[22].

b) Because of the fission property of Uranium, a large number of neutrons are created in the hadronic showers, and they make a significant contribution to the hadronic signal[12].

Applying the above theories of high energy particle interaction with materials, I will estimate the high energy electromagnetic and hadronic particle signals in the D0 calorimeter. The mip signal will used as a scale.

For electromagnetic particles, the total detectable signals are:

70% E, where E is the total energy of the incident particle.

For the hadronic particles, the contributions to the detectable signals are:

1) From Formula 2.6, the EM component is: $\langle f_{em}(E)\rangle = 0.1 \ln E(GeV)$

2) The HD component is: $\langle f_{had}\rangle = 1 - \langle f_{em}\rangle$. From Formula 2.4, the ionization part is then $\langle f_{ion}\rangle = 40\% * \langle f_{had}\rangle$. However, the saturation effect of the calorimeter has to be considered. The estimated detection efficiency for this energy is about 90%[21].

3) The signals contributed by neutrons are estimated from theoretical calculations[18] and experimental measurements[12]. The following estimate of the neutron processes per GeV of hadronic energy are based on [12, 18];

the average number of fissions caused by neutrons is 10 fissions/GeV,

the average number of neutrons created in the shower is 45/GeV.

The detectable energy in the form of soft γs released from these neutron processes is; the average fission contribution:

7.5 MeV/fission * 10 fissions/GeV = 75 MeV/GeV,

the average neutron nucleus inelastic scattering contribution:

5 MeV/neutron * 45 neutrons/GeV = 225 MeV/GeV,

the average neutron capture contribution:

7.5 MeV/neutron cap * 45 neutrons/GeV = 338 MeV/GeV.

But the neutron capture largely happens after the neutrons slow down to the keV energy range. The processes which slow down these neutrons take up to a few μs. Brueckmann[18] has calculated that after 100 ns, ~25% of the neutrons would be captured, and nearly 100% of the neutrons would be captured after 2 μs. In the case of the D0 calorimeter, we use 2.2 μs integration time for the precision readout, and approximate 250 ns integration time for the fast trigger readout. Following Brueckmann's calculation, I calculate that after 250 ns, about 45% of neutrons would be captured. The total neutron signals between 250 ns and 2.2 μs are

250 ns:	452 MeV/GeV,
2.2 μs:	638 MeV/GeV.

These signals are in the form of soft γs, and the detection efficiency of these soft γs is only 40%[12]. Therefore the detectable soft γ signal from neutron processes between 250 ns and 2.5 μs integration time is 181 to 255 MeV/GeV.

2.5.2 Example calculation

To summarize the above estimates, I will calculate the detectable signals from 100 GeV electromagnetic particles and hadronic particles. I will use mip's sampling as a scale. It

	The detectable signal in 100 GeV electron showers (GeV)	The detectable signal in 100 GeV pion showers (GeV)
Electromagnetic component	70	35
Hadronic ionizing component		18
Soft γs from neutrons		9.1 / 12.7(250ns / 2.2 μs)
Total detectable signal	70	62.1/ 65.7 (250ns / 2.2 μs)

Table 2.1

is summarized in Table 2.1.

The electron showers are made up of 100 percent electromagnetic components. The detection efficiency for the high energy electron shower is only 70% (e/mip=0.7), so the detectable signal for the electromagnetic particles is 70 GeV.

The electromagnetic component of the pion showers is $\langle f_{em} \rangle = 0.11 \ln(E) = 50$ GeV. With the same detection efficiency as the high energy electrons (70%), the detectable signal is 70%*50 = 35 GeV.

The pure hadronic component of the pion showers is $\langle f_{hd} \rangle = (1-50\%)*100\text{GeV} = 50\text{GeV}$. In this component, the fractional energy deposited through ionization is 40%, and the detection efficiency of this signal is 90%. This yields a detectable signal of 50*40%*90% = 18 GeV. The total energy in the form of soft γs produced through neutron-nucleus processes is 0.45*50 = 22.5 GeV with 250 ns integration time, and 0.64*50 = 32 GeV with 2.2 μs integration time. The detection efficiency of these soft

γs is only 40%. This yields a detectable signal of 40%*22.5 = 9.1 GeV with 250ns integration time, and 40%*32 = 12.7 GeV with 2.2 μs integration time.

I conclude that at 100 GeV,

250 ns: $e/\pi = 70/62.1 = 1.12$,

2.5 μs: $e/\pi = 70/65.7 = 1.07$.

Therefore, a 5% e/π ratio difference between 250 ns integration and 2.2 μs integration times is expected.

In the above estimate, there are two parameters that are not known very precisely; the efficiency of detecting the signal from the ionizing hadronic component, and the efficiency of detecting the soft γs from neutron processes. But the estimate of the e/π ratio difference between short and long integration times is not sensitive to these two parameters.

2.6 D0 central calorimeter structure

The D0 calorimeter [2](fig. 2.3) is divided into three parts: one central calorimeter (CC), and two identical end calorimeters (EC). In this dissertation, I am mainly going to analyze the calorimeter test beam data taken with the CC only, so I will only describe the CC structure here. More detailed information about the D0 calorimeter structure (both CC and EC) can be found in [2].

The central calorimeter is segmented longitudinally and transversely. Longitudinally, it is constructed with three different modules named by their functions: the electromagnetic (CCEM) module, the fine hadronic (CCFH) module and the coarse hadronic (CCCH) module. Both CCEM and CCFH modules are further divided longitudinally. In the transverse dimension, all modules are subdivided into segments

with a size of $2\pi/64$ radians in azimuth and 0.1 pseudorapidity (η)[2] in the Z dimension, with the exception of the third CCEM sub-layer.

Figure 2.4 shows the central calorimeter consisting of 32 EM modules, 16 FH modules, and 16 CH modules. The shaded region shows the modules used for the 1990-1991 load-two test beam runs.

A CCEM module is shown in Figure 2.5. It has 20.5 radiation lengths (X_0) of material in 21 Uranium-liquid Argon (U/LAr) gaps, with G10 signal boards in the center of the liquid Argon gaps. There are extra G10 laminated readout boards in some U/LAr gaps. Figure 2.6 shows the U, LAr and G10 gap structure of CCEM. The Uranium plates are 3 mm thick; the LAr gaps are 0.089 inch yielding a sampling fraction of about 12.0%. The CCEM is read out in four separate sub-layers, comprised of 2.0, 2.0, 6.8 and 9.7 radiation lengths. This fine longitudinal segmentation in the early part of the array contributes to the excellent electron and pion discrimination of the calorimeter. Each CCEM module is divided into two readout segments in azimuth (ϕ), with $\Delta\phi=2\pi/64$. In the z dimension, the readout segments are made to have each tower subtend uniform $\Delta\eta = 0.1$ intervals. The exception to the transverse segmentation described above is in the third CCEM sub-layer, where the typical EM showers are at the peak of their longitudinal development. Throughout this layer, the transverse segmentation is increased twofold in both ϕ and η dimensions. This design improves the resolution of the EM shower positions and the rejection of photon hadron overlaps which mimic electron candidates.

A CC fine hadronic (CCFH) module (Figure 2.7) is comprised of 50 U/LAr gaps totaling 3.24 interaction lengths. The gaps all contain 0.236 inch 1.7% niobium 98.3% uranium alloy plates and 0.089 inch LAr gaps. This gives a sampling fraction of about 7%. For readout the module is divided longitudinally into three sub-layers of 1.36, 1.04

and 0.84 interaction lengths to try to equalize the capacitance of the readout channels. The transverse segmentation is done the same way as in the normal CCEM layers.

The main purpose of the CC coarse hadronic (CCCH) module (Figure 2.8) is to catch the longitudinal leakage of hadronic showers. For the average hadronic showers at the Fermilab collider energy, the longitudinal energy leakage is expected to be around a few percent. Since the resolution of this measurement will not have any great contribution to the overall energy resolution, the equalization of the electron and hadron responses is not important. The CCCH is made of 10 gaps of 1.625 inch copper plates and 0.089 inch LAr gaps. This gives 2.93 interaction lengths and a very coarse sampling fraction of 1.7%.

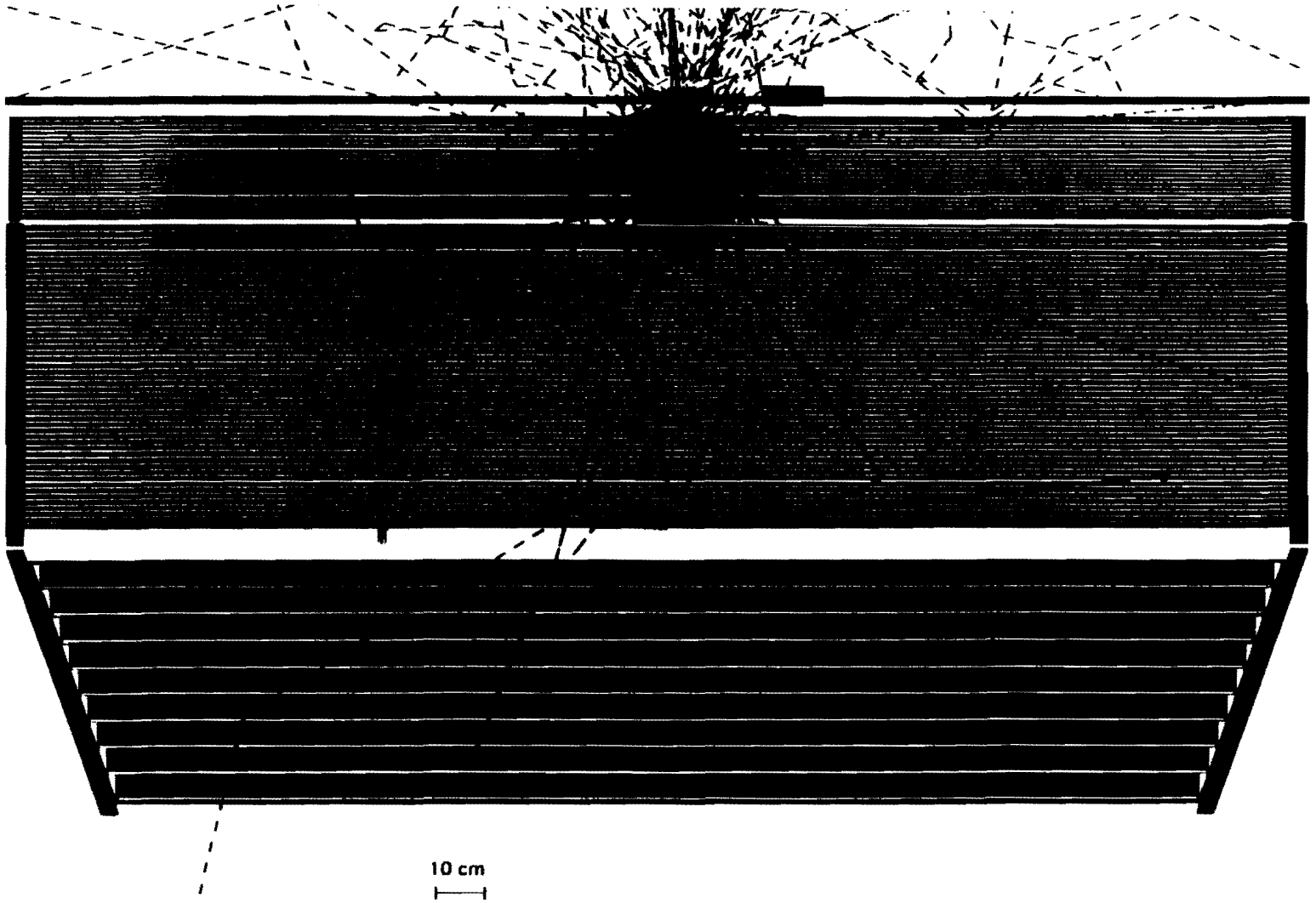

Figure 2.1 A side view of Monte-Carlo simulation of a 50 GeV electron hitting the D0 central calorimeter.

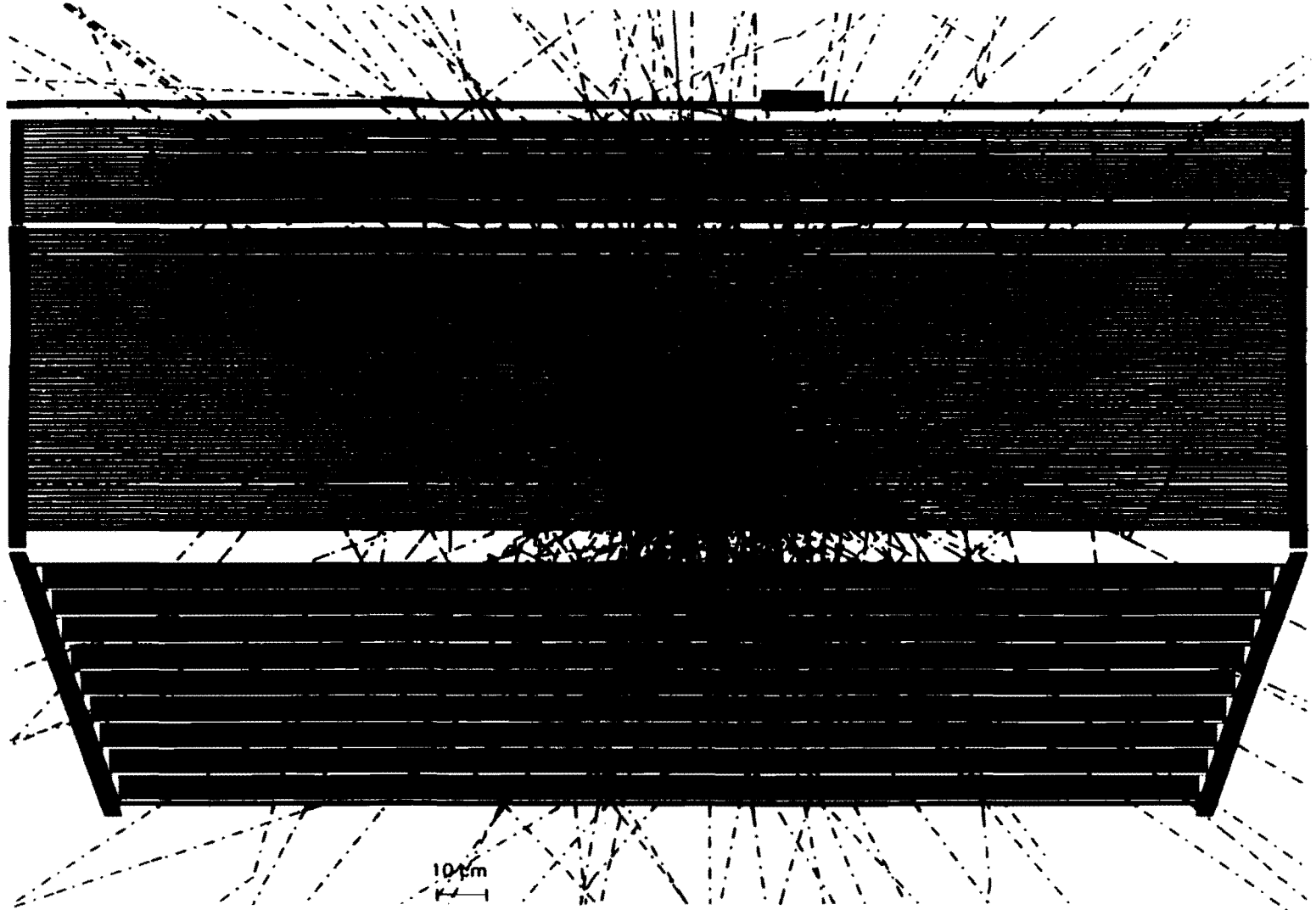

Figure 2.2 A side view of Monte-Carlo simulation of a 50 GeV pion hitting the D0 central calorimeter.

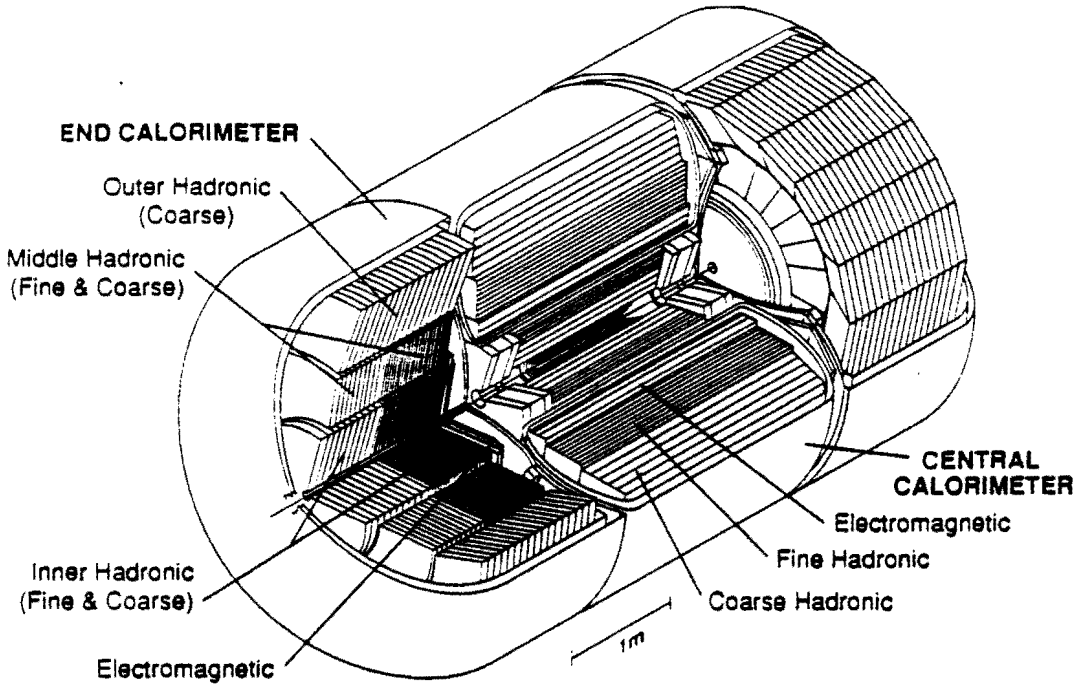

Figure 2.3 D0 liquid Argon calorimeter

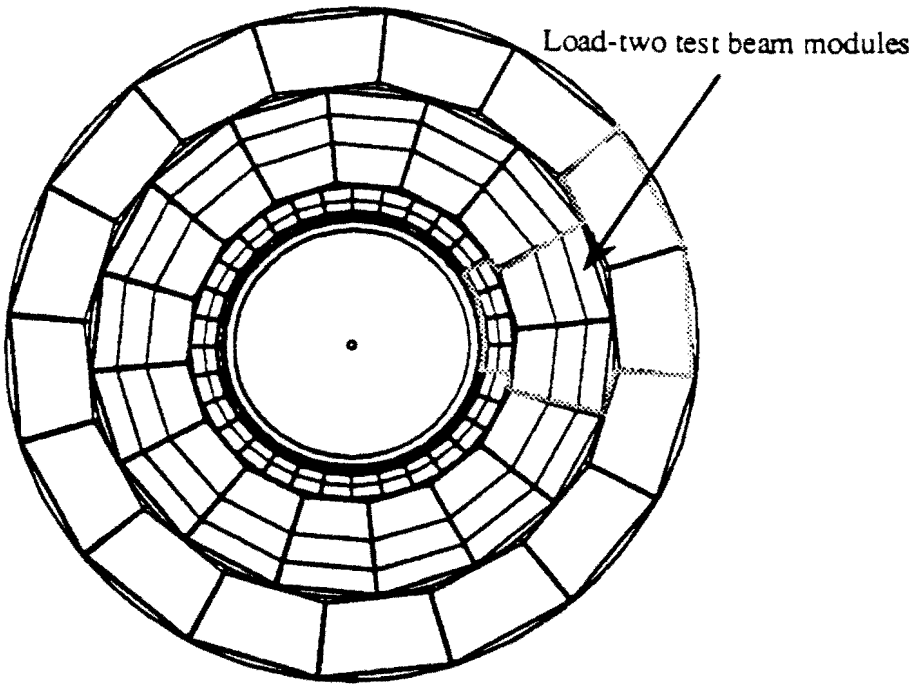

Figure 2.4 End view of the D0 central calorimeter. The inner ring is made of 32 EM modules, the middle ring is made of 16 FH modules, and the outer ring is made of 16 CH modules.

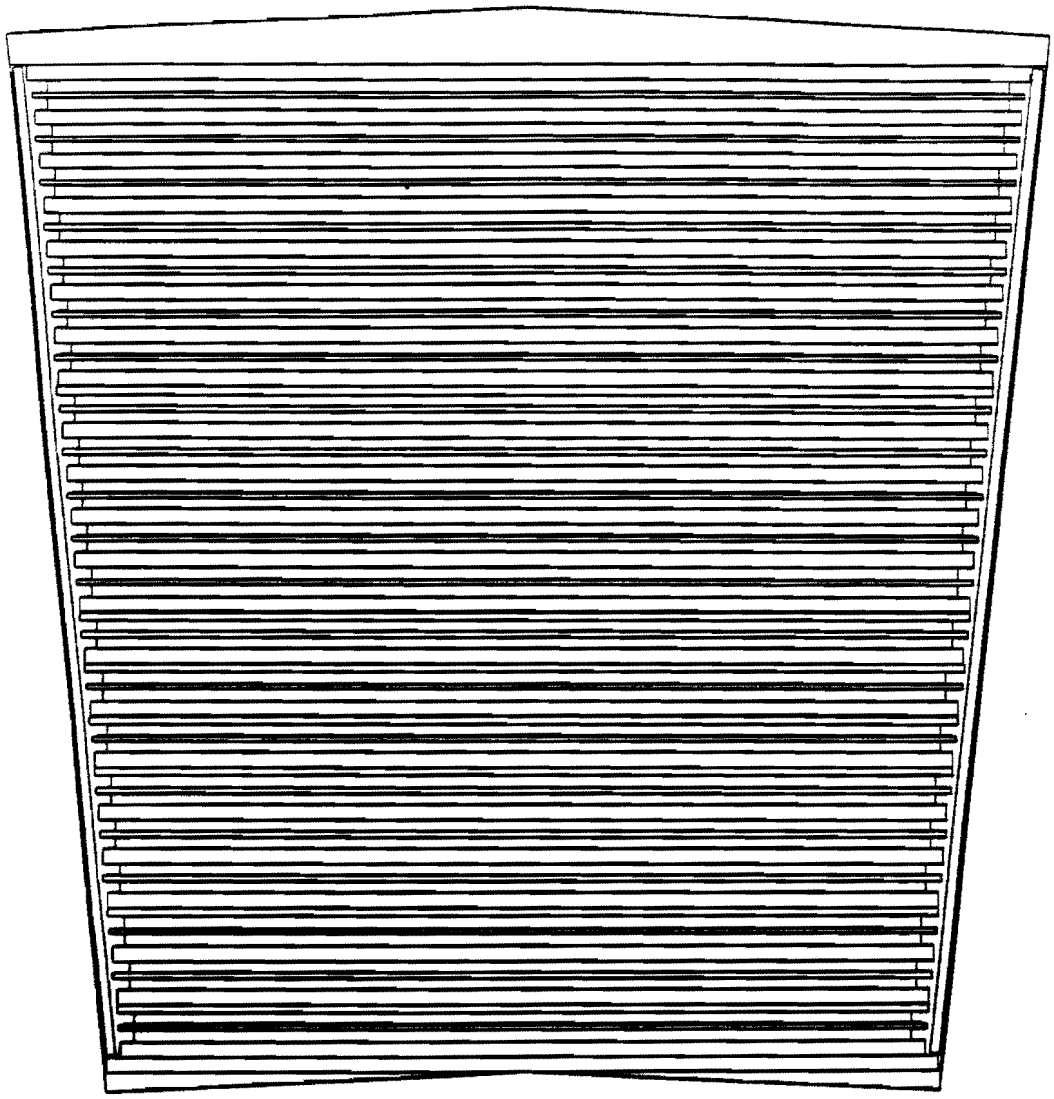

Figure 2.5 End view of a D0 central calorimeter electromagnetic module (CCEM).

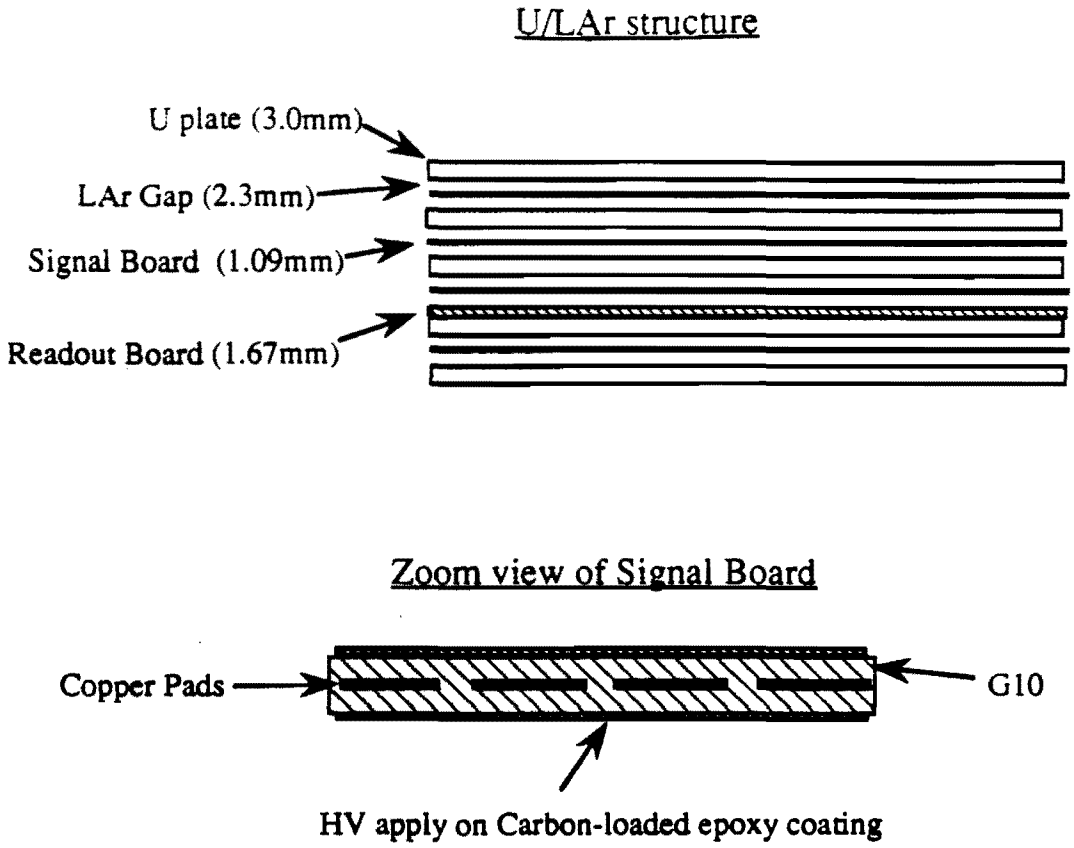

Figure 2.6 D0 central calorimeter gap structure

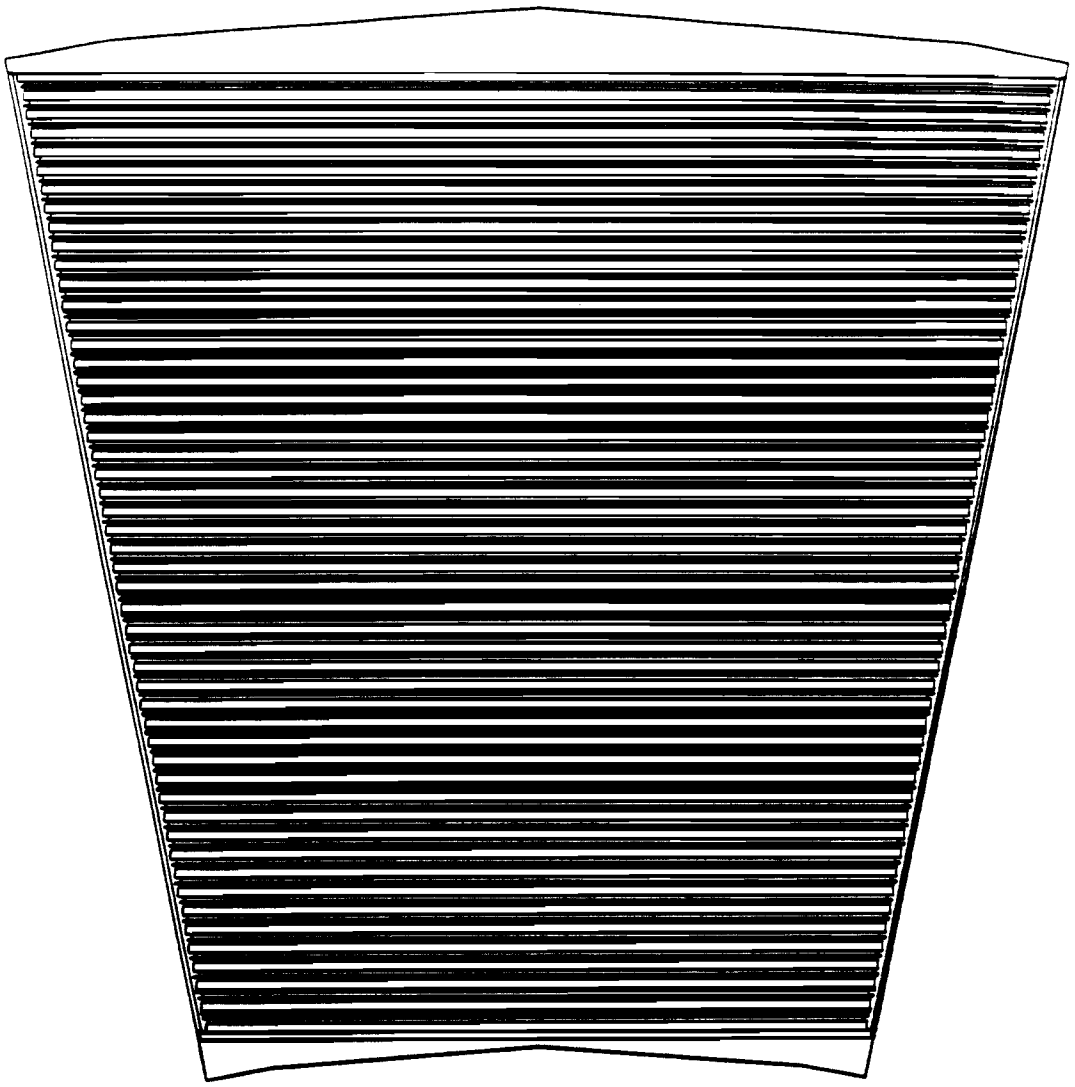

Figure 2.7 End view of a D0 central calorimeter fine hadronic module (CCFH).

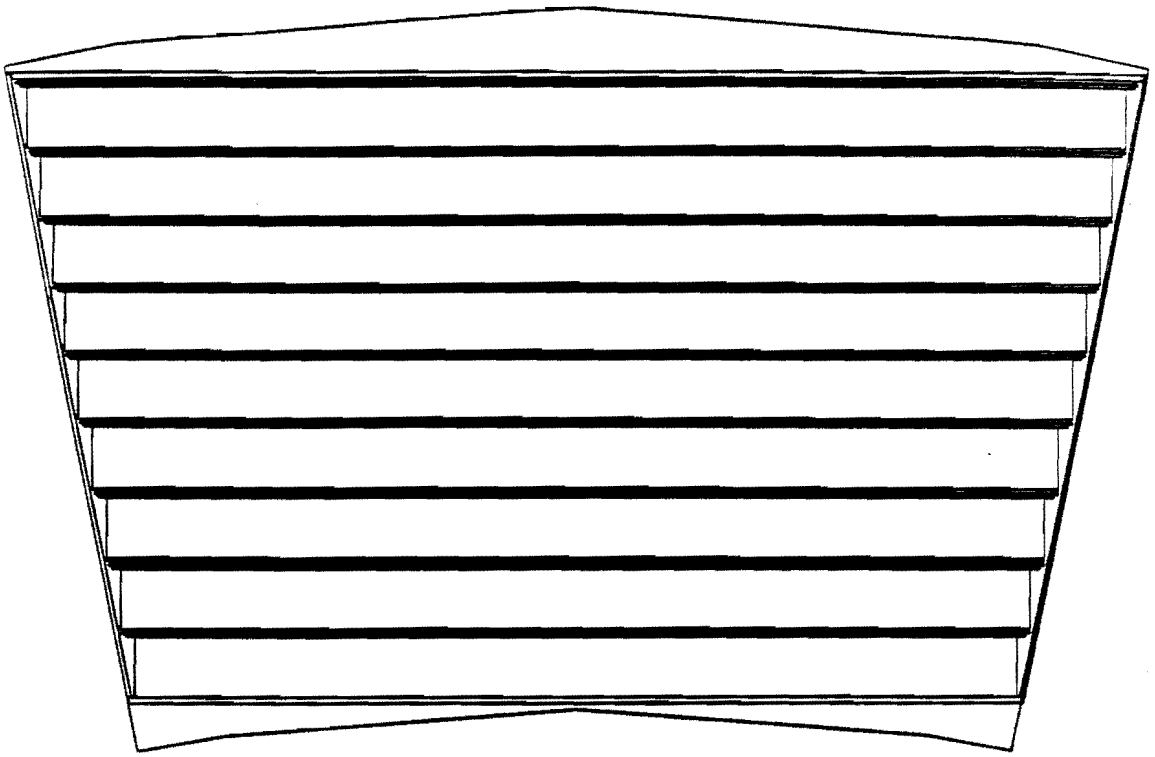

Figure 2.8 End view of a D0 central calorimeter coarse hadronic module (CCCH).

Chapter 3
D0 Calorimeter electronics

3.1 General information

The use of liquid Argon as a unity gain ionization chamber to sample EM and HD shower development offers unique advantages in maintaining the calibration of the energy response of the calorimeter. At the same time one is faced with having to measure the signals over a large dynamic range. Furthermore, the high interaction rate expected at Tevatron requires new solutions to avoid pile-up in measuring the correct signal amplitudes. The output signals are best measured in electron charges "e", and range typically from 50,000 to 500,000 e's for muons in various parts of the calorimeter and up to $6x10^8$ e's for 500 GeV electromagnetic or hadronic showers. If an accuracy of 10% is desired for single muon signals, a dynamic range of 10^5 is required. This dynamic range can be reduced by a factor of 5 by judicious longitudinal segmentation.

The D0 calorimeter parameters are[2]:

Electrons collected /MeV of energy in liquid Argon:	9450
Fraction of energy in liquid Argon in the EM calorimeter:	0.12
Fraction of energy in liquid Argon in the FH calorimeter:	0.07
EM calorimeter resolution:	$0.15/\sqrt{E}$
Hadron calorimeter resolution:	$0.50/\sqrt{E}$
Total number of readout channels:	50,000

3.2 The D0 calorimeter precision read out system

The D0 calorimeter electronics system is made of three major subsystems (Figure 3.1): the preamplifier, the base line subtracter (BLS), and the analog to digital converter (ADC). The preamplifier is a high-gain charge-sensitive amplifier, which converts the input charge to voltage. Figure 3.3a shows the circuit of the D0 preamplifier. The BLS performs the following functions. It takes a sample of the preamplifier output voltage right before the $p-\bar{p}$ interaction (this is called the base sample), and it takes another sample of the preamplifier output voltage 2.2 μs after the $p-\bar{p}$ interaction (this is called the peak sample). Then it subtracts the base from the peak, and stores the voltage in an analog buffer. Finally the two samplers are free to take samples of the next $p-\bar{p}$ interaction, and the voltage in the analog buffer is available for the ADC to digitize. The sampling time of 2.2 μs is chosen to optimize the noise and speed required for the 3.5 μs Tevatron $p-\bar{p}$ collision cycle. Another feature of the BLS is the fast trigger signal pickup circuit. It provides fast trigger signals (with shaping constant of 250 ns) for the level-one calorimeter trigger. Figure 3.3a shows the BLS signal shaping circuit and trigger pickup circuit. Figure 3.4 shows the SPICE simulation of the signal at the preamplifier input, the signal at the precision BLS samplers, the signal at the trigger pickup output, and the signal at the trigger flash ADC (FADC) input. The ADC uses 12 bits and two different amplifiers to provide a 15 bit dynamic range. References [1], [2] and [3] provide detailed descriptions of the D0 calorimeter electronic design.

Another subsystem integrated within the D0 calorimeter precision electronics is the precision calibration pulser system. Because of the large number of calorimeter channels, "off the shelf" components were used for the preamplifiers in order to keep the cost down. For example, the feedback capacitors have a variation of a few percent, the transistors used in the preamplifier have a beta value only guaranteed by the supplier to the range of 200 to 400, and the resistors used in the preamplifier are one percent

precision resistors. All these factors cause the gain of the preamplifiers to have a variation of a few percent. In order to achieve a gain uniformity of less than one percent, a precision calibration pulser system was built in the D0 calorimeter electronics. The pulser calibration system has a precision pulse generator that generates a precision pseudo-Gaussian shaped current pulse. It injects charge into each preamplifier input through a precision resistor (0.1%). The channels into which the pulser injects charge are chosen by a computer. The responses of the calorimeter electronics are read out and analyzed in order to determine the gain of each preamplifier channel. This calibration system enables us to achieve a uniformity of 0.3% for the precision calorimeter readout.

3.3 Level-one calorimeter trigger electronics

3.3.1 Introduction

The D0 level-one calorimeter trigger[16] is designed to be able to trigger on every $p-\bar{p}$ collision without introducing any dead time. In order for the other detector front-end electronic systems to be able to latch their data, the level-one calorimeter trigger decision must be made within 900 ns after each $p-\bar{p}$ collision (not counting cable delay). Instead of waiting to collect all the charge in the calorimeter liquid Argon gaps (which takes over 400 ns), a special trigger signal path is designed to provide a fast signal for the calorimeter trigger electronics. It uses a differentiator with a shaping constant of 250 ns, applied to the preamplifier output signal, to get the calorimeter energy information 250 ns after the particles hit the calorimeter. The simulated signals are shown in Figure 3.4.

In order to efficiently process the information coming out of the highly segmented calorimeter, signals from some calorimeter readout cells are grouped together to form a calorimeter "trigger tower". There are two kinds of trigger towers: the electromagnetic (EM) tower that consists of the sum of all the layers in the EM calorimeter in two units of η and ϕ segments, and the hadronic (HD) tower that consists of the sum of all the layers

in the fine hadronic (FH) calorimeter (Uranium hadronic calorimeter) in two units of η and ϕ segments. All the channels needed to form a trigger tower (both EM and HD) are contained on one BLS card. This scheme reduces the fast calorimeter trigger electronics channels to 2560 from the 50,000 individual preamplifier channels, while still retaining projective towers with adequate segmentation. The final calorimeter trigger input signals are 1280 EM and HD trigger towers that have the size of 0.2x0.2 in η and ϕ dimensions.

Figure 3.2 shows a conceptual schematic of the D0 level-one calorimeter trigger analog signal path. The key components which affect the gain of the level-one calorimeter trigger include the detector readout pad (C_d), the cable connecting the detector readout pads with the preamplifiers (T_1), the charge sensitive preamplifier with integrating capacitor C_f, the cable connecting preamplifiers with the BLS's (T_2), the trigger pickup differentiator made of C_t and R_t, the first trigger tower adder that adds all the layers of EM or HD calorimeter and the adjacent ϕ units, the second trigger tower adder that adds the adjacent η units, the trigger signal differential driver (TrgDrv) that drives the long cable carrying the signals of the EM and HD trigger towers to the calorimeter trigger electronics, the calorimeter trigger analog receiver, and the flash ADC (FADC). The digitized data passes through the digital part of the calorimeter trigger electronics to make the final trigger decision. In this dissertation, I will only discuss the analog components of the calorimeter trigger electronics, which are directly related to the measurements. The digital part of the calorimeter trigger electronics is described in [16].

3.2.2 Difficulty of fast shaping.

Without specific input impedance matching for each preamplifier, the gain of the trigger differentiator is sensitive to the variation of the preamplifier input impedance[13]. It is necessary to match each channel's gain before they are summed into trigger towers. Trigger summing resistors R_i and R_{ii} are chosen to correct the gain differences of each

channel. In the following sections, we will show how we determine the relation of trigger gain to input impedance, and some tests we have done to verify this relation.

3.2.3 SPICE[7] simulation of level one calorimeter trigger electronics

In order to understand the input impedance effects on the gain of the trigger differentiator, a detailed simulation of the level-one calorimeter trigger analog circuit (Figure 3.2 and 3.3) is done with SPICE3C1[7] (an electronics circuit simulation program) using measured parameters of the active elements. The input impedance of the preamplifier is determined by T_1 and C_d. C_f and T_2 also affect the trigger differentiator's gain. The total input capacitance of the preamplifier (C_{in}) is the sum of C_d and the capacitance of T_1. In the D0 detector system, there are only two kinds of feedback capacitors C_f: 5.5pf and 10.5pf. C_d varies from 1.0 nf to 7.0 nf. T_1 is a 50 Ω coaxial cable and its length varies from 10 to 20 feet (it is fixed at 18 feet for the test beam). I used the SPICE simulation to study the relation of the trigger differentiator's gain with each of the elements that affect the input impedance.

a) The Gain vs. C_{in}:

As shown in Figure 3.5, the gain of the trigger differentiator has a strong dependence on the C_{in} and C_f. In this figure, I use fixed T_1=18 feet, T_2=180 feet and two kinds of C_f (5.5 pf and 10.5 pf). By varying C_d, I can get different C_{in}. Under these conditions, the relation between the trigger differentiator's gain and input capacitance is:

$$G_{5.5pf} = 0.4709 - 0.0627C_{in} + 0.0311C_{in}^2 \qquad (3.1)$$

$$G_{10.5pf} = 0.4535 + 0.01575C_{in} - 0.02247C_{in}^2 + 0.00337C_{in}^3 - 0.000157C_{in}^4 \qquad (3.2)$$

I will show how to use these Formulas to correct the gain C_{in} dependence.

b) The Gain vs. L_{in}

I used the SPICE simulation to study the effect of L_{in} on the gain of the trigger differentiator. The study shows that there is only a weak dependence. The gain will change 5% per 1 μH of L_{in}. The total input inductance L_{in} is the sum of the contribution of the pads and traces of the detector module and the cable T_1. For the CC, the module pads and traces make a very small contribution to the L_{in} (on the order of 100nH); T_1 is the dominant contributor, its contribution is a fraction of μH. Therefore, only the inductance of T_1 needs to be considered in the trigger differentiator's gain correction. In the case of the test beam, where the T_1 cable had a fixed length, the inductance did not affect the uniformity of the trigger gain.

c) Resistance effect

The input resistance is generally very small, and its effect on the trigger gain is negligible.

d) Preamplifier transistor's beta effect

Because of the long cable between preamplifiers and BLS electronics (180f at the test beam), the beta value of the preamplifier output driving transistor Q3904 (Figure 3.3a) will affect the signal quality at the BLS receiving end. Any pulse shape change will affect the gain of the trigger differentiator. I have done a set of SPICE simulations to study the preamplifier transistor's beta effect. Figure 3.6a shows the calorimeter trigger response (TRG) and precision electronics response (BLS) vs. the transistor's beta values for a fixed size triangle pulse with different input capacitance. The beta effect on the BLS is very small, but the effect on the TRG is large, and the effect is dependent on the input capacitance of the preamplifier. The manufacturer guarantees that the transistor's beta value is in the range of 200 to 400. With this limit and the SPICE simulation results, I can estimate that the limits on the trigger gain variation caused by the preamplifier transistor's beta are ±5% for the EM channels, and ±8% for the HD channels.

Assuming a uniform distribution of the beta values, the variation of trigger gain is $\frac{\text{variation limit}}{\sqrt{12}}$, which is about 3% for the EM channels and 5% for the HD channels.

e) Trigger driver transistor's beta effect

The trigger cable drivers (TrgDrv) (Figure 3.3b) use the same kind of transistor as the preamplifier. It is expected that these transistors' beta values will have some effect on the trigger cable driver's gain. Figure 3.6b shows the SPICE simulation of the trigger cable driver's gain vs. beta value of one transistor. In this simulation the beta of other transistors was set to the measured value; only the beta value of transistor 2N3906 was varied. The trigger cable driver transistor's beta effect is less than 2%, with beta changes between 200 to 400. This is a much smaller effect than the preamplifier driving transistor. This is because the fast shaping of the trigger differentiator is more sensitive to the signal shape than the calorimeter trigger receiver.

3.2.4 NYU test bench measurement

To test the SPICE model, I measured the Gain vs. C_{in} relation on the D0 front-end electronics test bench (Figure 3.7) at NYU (New York University). The test was done by using a triangle shape pulser, which mimics the charge pulse shape from the real beam, to inject charge on a capacitor, which was connected to the D0 preamplifier with the standard D0 T_1 cable. By changing the capacitor, I measured the Gain vs. C_{in} relation. The test bench measurement and the SPICE simulation are shown in Figure 3.8a. The SPICE results are normalized to match the data at the Cin=3.2nf point. The maximum deviation between the simulation and the measurement is less than 2%.

3.2.5 Single channel measurement

To further test the SPICE model, I used our test beam facility to measure the trigger response with only a single preamplifier connected to the trigger tower sum. This insured that the trigger signal came from a preamplifier with known C_{in}. The measurement and SPICE simulation are shown in Figure 3.8b. The data points include different preamplifier channels with different C_{in}, C_f and different trigger cable drivers (EM and HD towers). The SPICE simulation was done with each channel's nominal specification, and was normalized to match the data at C_{in}=2.5nf point. The figure shows that the data of the EM channels (channels with $C_{in} < 3$ nf) and simulation agree well, and the data of two HD channels have about 6% deviation from the simulation. From the analysis of the preamplifier's transistor beta effect (Section 3.2.3d), the gain of the HD channels could have a variation of 5% due to the transistor beta variation. Furthermore, the single channel test has another limitation, which is the trigger signal crosstalk between preamplifier channels on the same BLS card (Section 5.2.3). Because of this crosstalk, the Trg/BLS ratio of the single preamplifier channel is sensitive to how much energy is in the nearby cells. These factors limit the precision of the single channel test.

3.2.6 Summary of trigger differentiator's gain correction

With a SPICE simulation, the trigger gain with different input impedance can be predicted to a precision of 2%. But the trigger gain has a variation caused by the individual amplifier transistor's beta value variation. The trigger gain variation will be investigated in Chapter 5 by using the test beam data.

On a special note, the precision calibration pulser system is not very useful for the trigger gain calibration, because the calibration pulser uses a pseudo-Gaussian shaped pulse

(Figure 3.9), which is chosen to minimize the systematic error from the cables and print circuit traces of the precision readout system. The charge pulse from the beam is a sharp triangle shape (Figure 3.9). Also, the calibration pulser injects the charge pulse at the input of the preamplifier, whereas the charge pulse caused by the particle showers is injected at the detector pad. Due to these differences between the calibration pulse and the beam charge pulse, the trigger differentiator has a different response to these two kinds of charge pulses. The calibration pulser system can not be used to do the quantitative study of the trigger gain. But it is still useful for checking dead channels and doing qualitative studies (like crosstalk).

3.4 The test beam trigger summing resistor selection

For the 1991-1992 test beam, we have CC modules with fixed length T_1 (18 feet) and T_2 (180 feet) cables. I used the SPICE simulation with these cable parameters to get the Gain vs. C_{in} relation ($G(C_{in},C_f)$) for the test beam. This way, the cable effects on the input impedance are included in the formula. Formulas 3.1 and 3.2 are shown in Figure 3.5.

In order to choose the R_i to correct the energy scale of each individual preamplifier channel before the first adder, a few other factors that affect the energy scales of individual channels need to be included. These factors are the sampling fractions and the gain of the trigger tower adder.

a) The sampling fractions and feedback capacitors used in calculating the CC trigger summing resistors are shown in Table 3.1.

Detector Depth	Sampling fraction (%)	Feedback Capacitance C_f(pF)
EM layer 1	12.7	5.5
EM layer 2	12.7	5.5
EM layer 3 (all sections)	12.7	10.5
EM layer 4	12.7	10.5
FH layer 1	7.0	5.5
FH layer 2	7.0	5.5
FH layer 3	7.0	5.5

Table 3.1

b) Because the trigger tower adder has a finite open loop gain A (a few $x10^2$ instead of a few $x10^6$), its gain not only depends on the summing resistor and feed back resistor, but also has a weak dependence on the total input resistance, that is, the total parallel resistance of all the summing resistors. A trigger tower adder adds 6 to 14 channels at once. The total input resistance due to this parallel resistance is much smaller than the resistance of the individual summing resistor. Figure 3.10 shows the measured relation ($H(R_{par})$) that is the adder gain normalized to R_f/R_i (ratio of feed back resistor and sum resistor) vs. total parallel input resistance (R_{par}).

An adder with a finite open loop gain, A, and feedback resistance, R_f, is shown in the following figure:

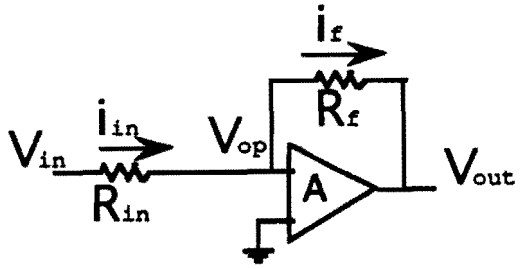

If $A \approx$ few $x10^2$ as in the case of the trigger adder, then we have

$$i_{in} \approx i_{out} \approx i,$$

$$V_{out} \approx iR_f; \quad V_{op} \approx \frac{iR_f}{A},$$

and we get

$$\frac{V_{out}}{V_{in}} = \frac{1}{(1+\frac{R_f}{AR_{in}})} * \frac{R_f}{R_{in}}.$$

The expected relation between the adder's gain H normalized to (R_f/R_i), and the total input resistance, R_{in}, is:

$$H = \frac{1}{\left(1+\frac{R_f}{A*R_{in}}\right)}. \tag{3.1}$$

The adder we used has $R_f = 3.0$ KΩ, and if we fit the data in Figure 3.10 with Formula 3.1, we get

$$H(R_{par}) = \frac{1}{\left(1+\frac{c}{R_{par}}\right)}; \quad c = 13.2 \tag{3.2}$$

where R_{par} is the total input resistance calculated from the parallel input resistors R_i.

The trigger adder's gain will be corrected according to Formula 3.2.

3.4.1 The trigger summing resistor (R_i) calculation

For energy E deposited in the calorimeter section, the voltage at the output of the preamplifier is

$$V_{preamp} = \frac{e*N_{eG}*E*Sf}{C_f}, \tag{3.3}$$

where $e = 1.6*10^{-19}$ $(Coulombs)$ is the electron charge, and

$N_{eG} = 9.45*10^6$ $(electrons/GeV)$ is number of free electrons created per GeV energy deposited in liquid Argon through the minimum ionizing process.

$$V_{adder1} = V_{preamp} * G(C_{in}, C_f) * \frac{3.0K\Omega}{R_i} * H(R_{i\_par}) \tag{3.4}$$

is the output voltage of the first adder, and

$$V_{adder2} = V_{adder1} * \frac{3.0K\Omega}{R_{ii}} * H(R_{ii\_par}) \tag{3.5}$$

is the output voltage of the second adder, where R_{i_par} and R_{ii_par} are the total parallel resistance of the first and second trigger adders.

The trigger differential driver turns V_{adder2} into a differential signal V_+ and V_- with $V_{adder2} = V_+ + V_-$.

For the test beam, the goal is to measure the energy of the incident particle (not the transverse energy as in D0), therefore, all the terminators of the calorimeter trigger analog receivers were set to have a constant attenuation factor of 2. The voltage at the trigger FADC input is: $V_{FADC} = V_{adder2}$.

I proceed by assuming ideal response of the adders ($H(R_{par}) = 1$), R_{ii} = 3.0 KΩ, and a 128 GeV dynamic range for the 8 bit FADC being equivalent to 2V on the FADC input.

$$2V = \frac{e * N_{eG} * 128 * Sf}{C_f} * G(C_{in}, C_f) * \frac{3.0K\Omega}{R_i} * \frac{3.0K\Omega}{3.0K\Omega}$$

$$R_i = 290{,}304 * \frac{Sf}{C_f} * G(C_{in}, C_f) \tag{3.6}$$

I have assumed that the energy deposited in the calorimeter is through the minimum ionizing process. In reality, since the D0 calorimeter has an e/mip ratio of 0.7, the electron signal is only 70% of the signal I estimated above. The above calculation of R_i will give us a true dynamic range of 180 GeV for the electron signal.

Once the R_i are determined, I can calculate the total parallel resistance (R_{i_par}) of the first adder input resistors R_i and $H(R_{i\_par})$. The first adder's gain change due to the small total parallel input resistance can be compensated for at the second adder to a good approximation by choosing R_{ii} as $\frac{R_{ii}}{3.0K\Omega} = \frac{1}{H(R_{i\_par})}$. For most of the trigger channels, R_{i_par} is approximately 50 Ω. The R_{ii} will be around 2.4 KΩ. The second adder will have a parallel input resistance > 1 KΩ. From Formula 3.2, the change of the second adder's gain due to the total input parallel resistance is negligible.

3.4.2 Selection of the load-two test beam trigger summing resistor

I used Formula 3.6 and the measured C_{in} to calculate the proper trigger summing resistors R_i of the load-two test beam configuration. The distribution of R_i is shown in Figure 3.11. The Figure shows that the same detector layer has approximately the same R_i value. I chose resistor values as the most probable value of the distribution, and uses only one kind of resistor for each detector layer. The values I chose for each calorimeter layers are listed in Table 3.2. The calculated resistor values for the FH layers have the largest variation, which is about 4%.

EM layer 1 & 2	1051 Ω
EM layer 3	665 Ω
EM layer 4	509 Ω
FH layer 1, 2 and 3	357 Ω

Table 3.2

After we have chosen the R_i resistors, we can use Formula 3.2 to calculate the R_{ii} values to compensate for the gain of the first adder. The result is: $R_{ii} = 2.43\ K\Omega$.

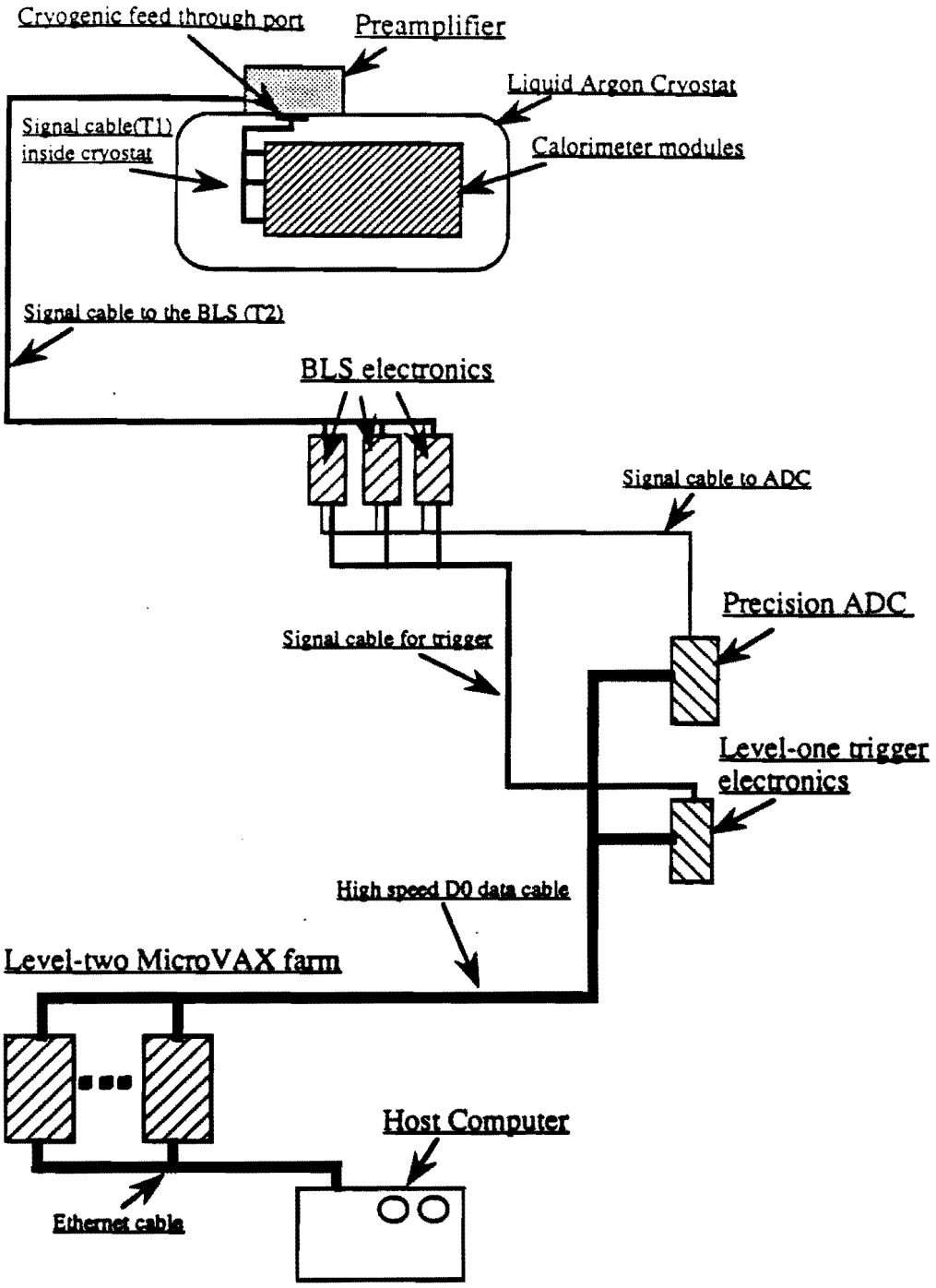

Figure 3.1 D0 calorimeter data path

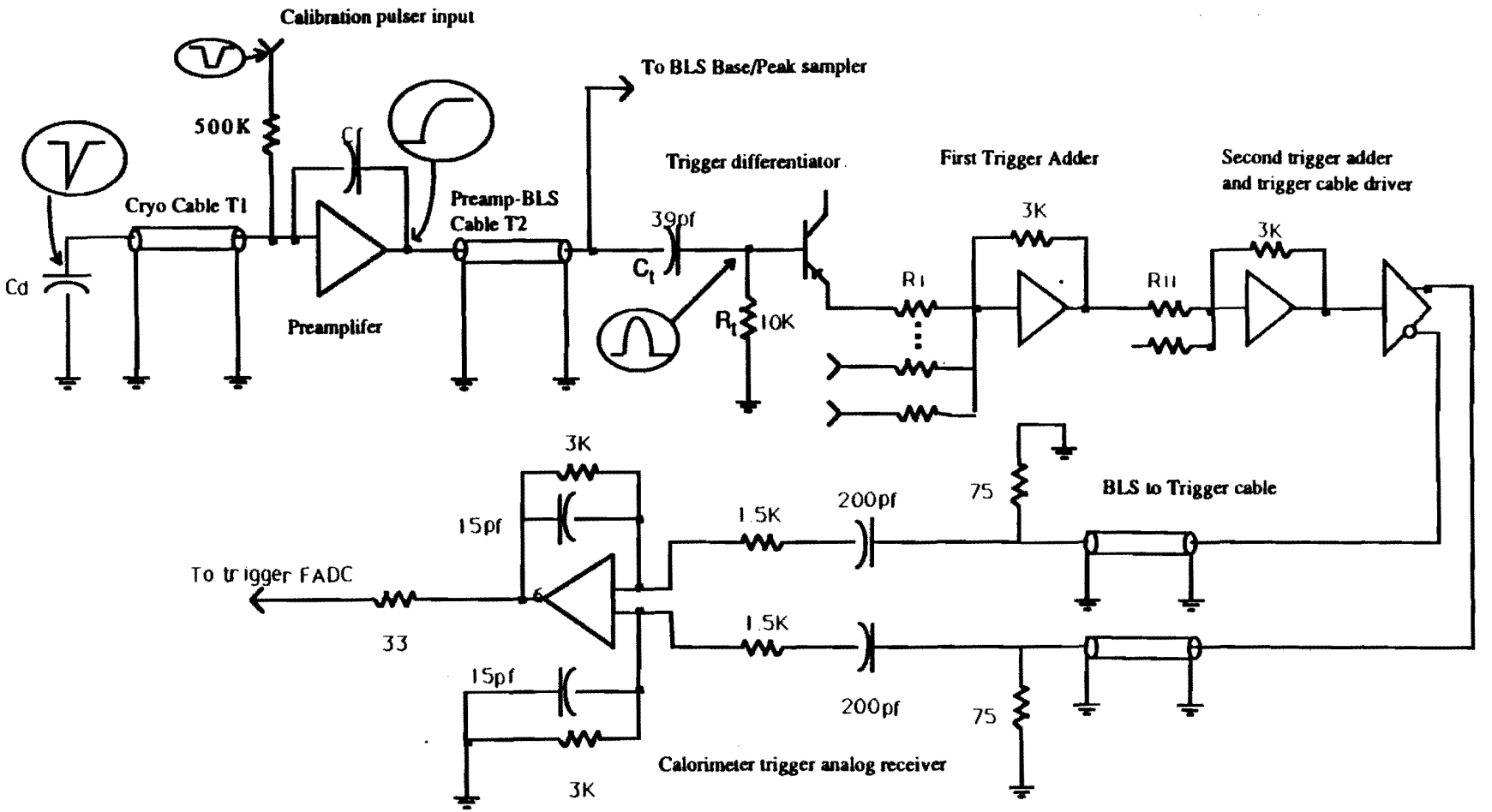

Figure 3.2 Calorimeter trigger schematic

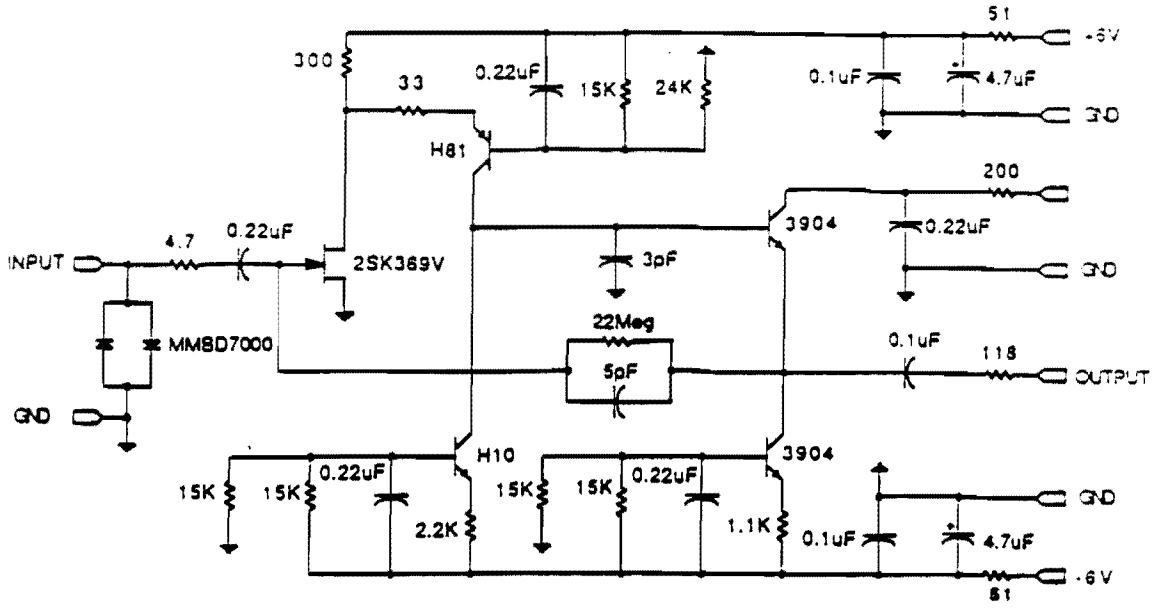

DØ calorimeter preamp (5pF version)

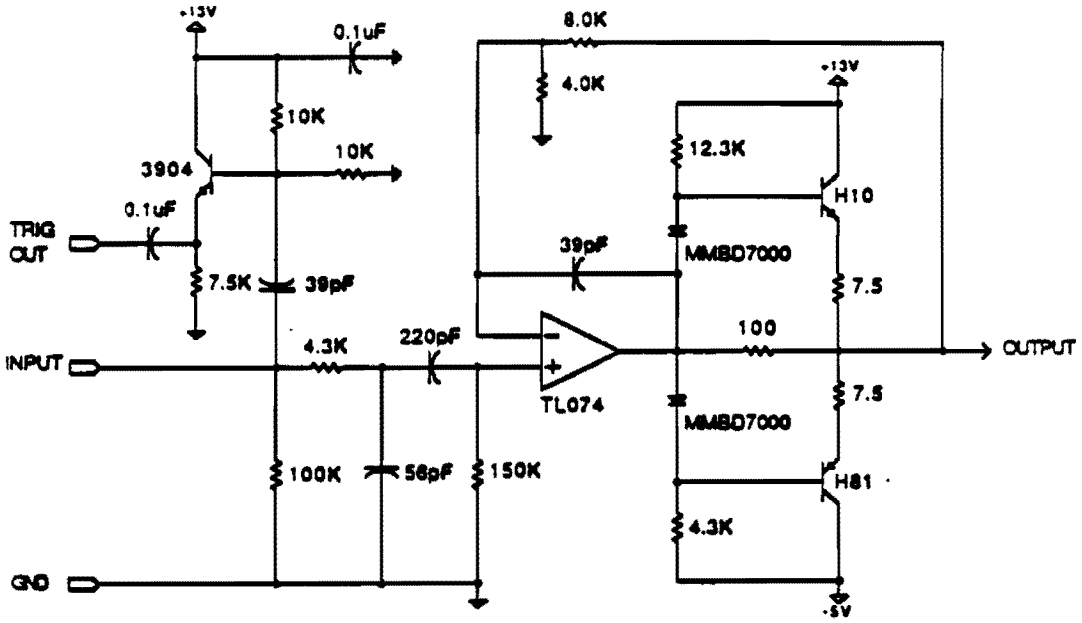

BLS signal shaping and trigger pickoff

Figure 3.3a

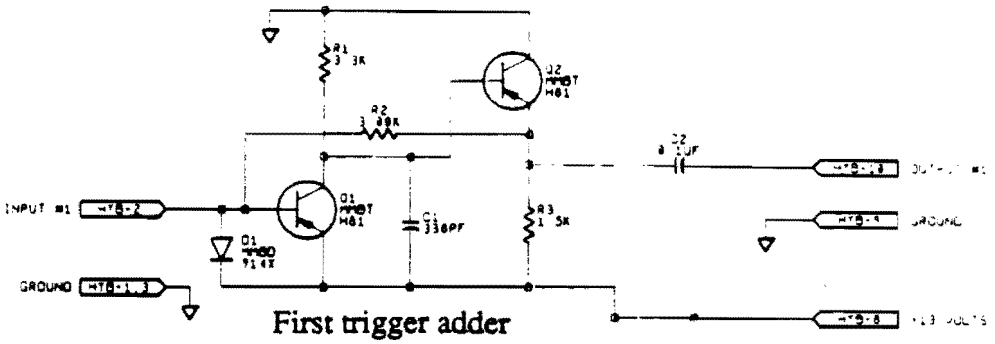

First trigger adder

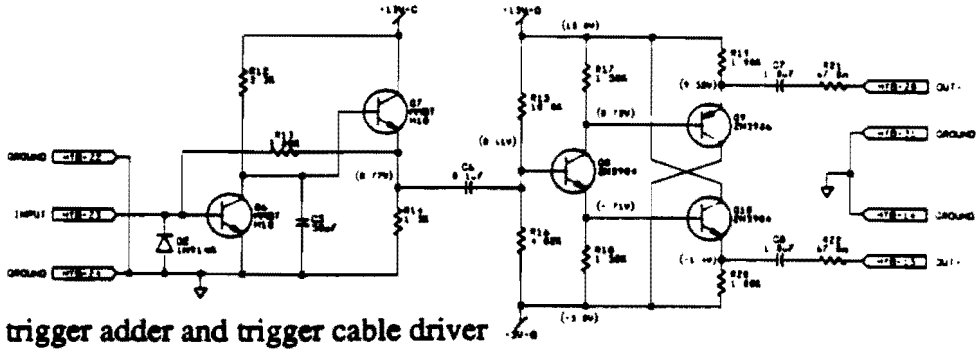

Second trigger adder and trigger cable driver

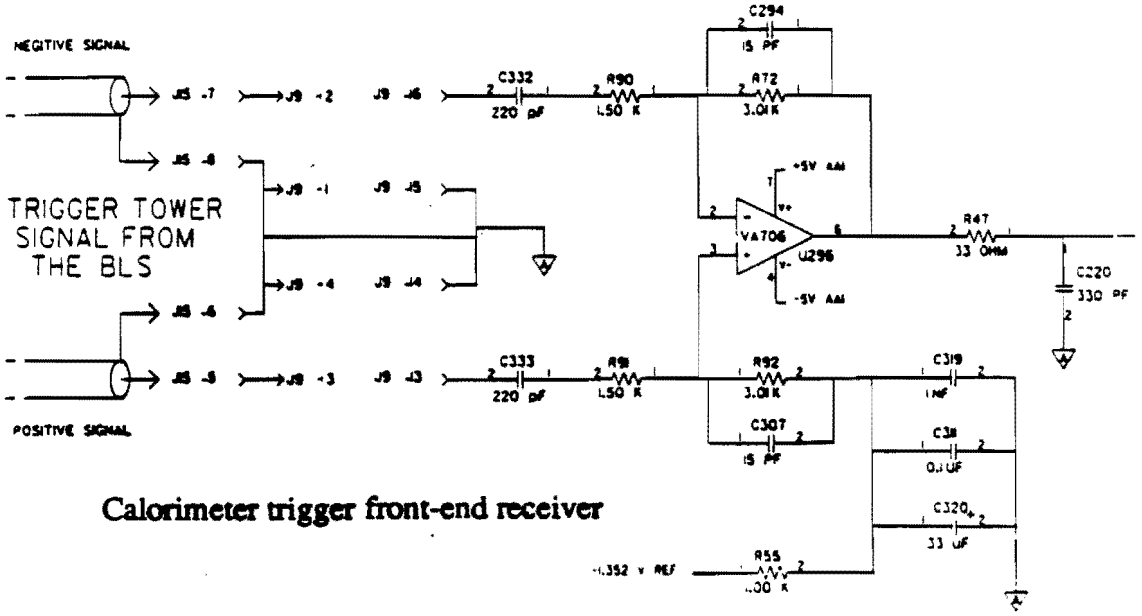

Calorimeter trigger front-end receiver

Figure 3.3b

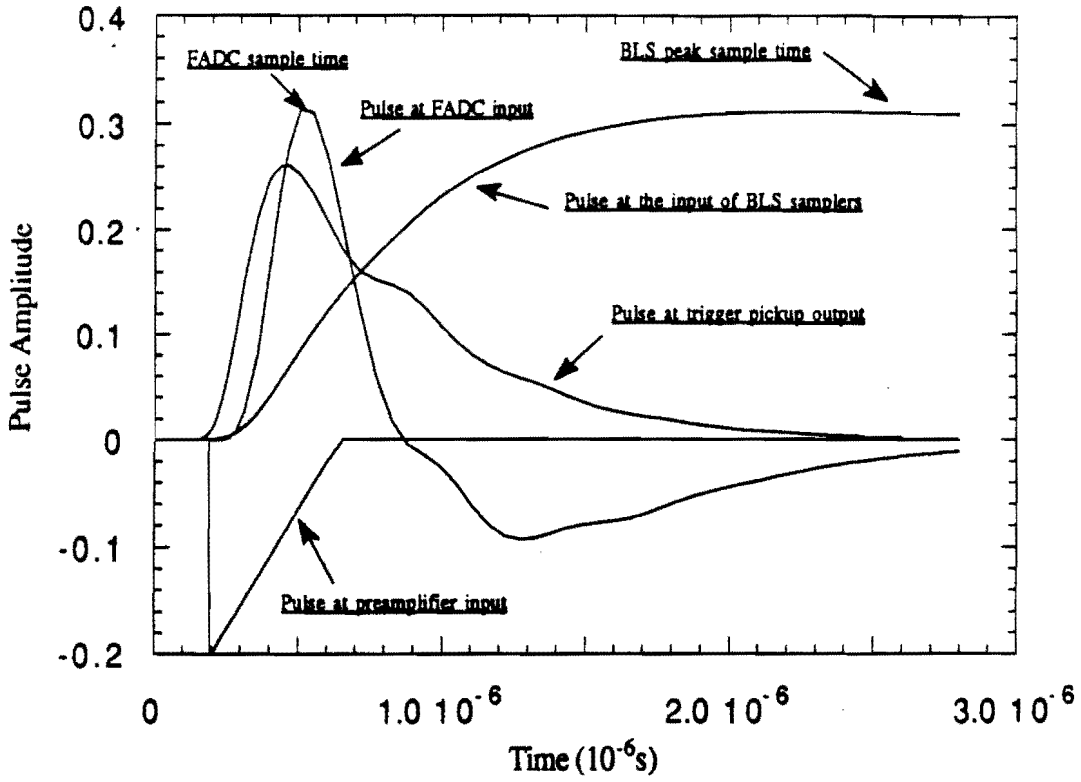

Figure 3.4 SPICE simulation of D0 electronics pulse shapes

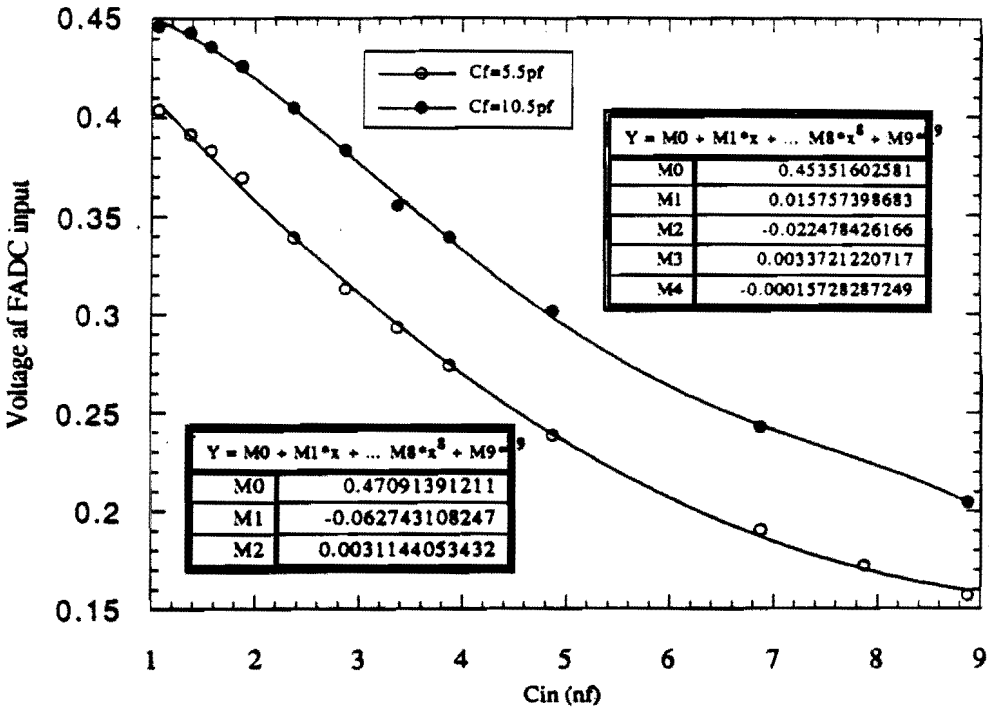

Figure 3.5 Trigger FADC input voltage vs. Input capacitance

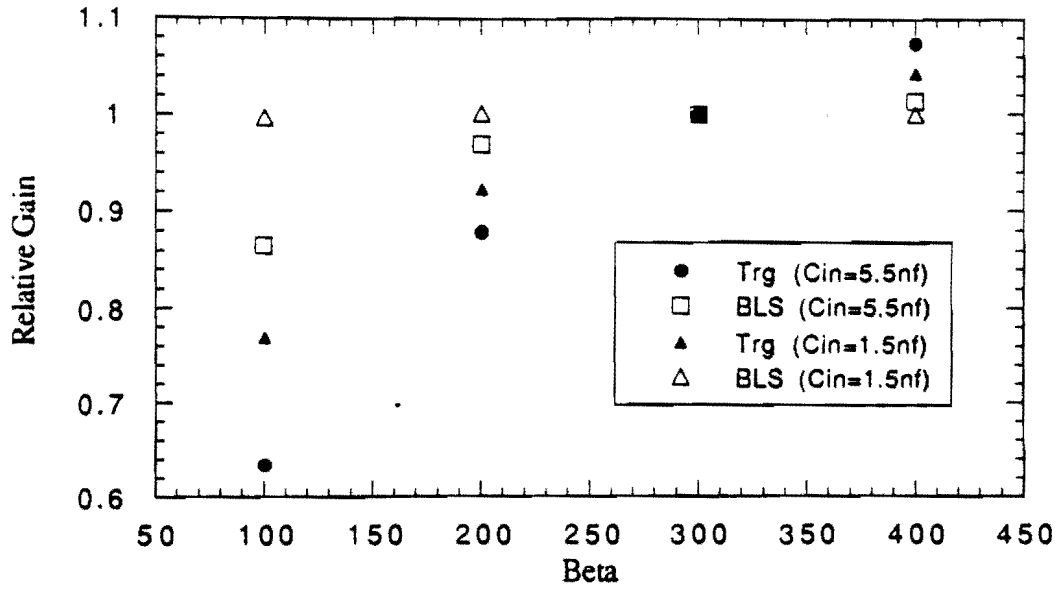

Figure 3.6a SPICE calculation of preamplifier beta effect, the differences are normalized to the beta=300 point

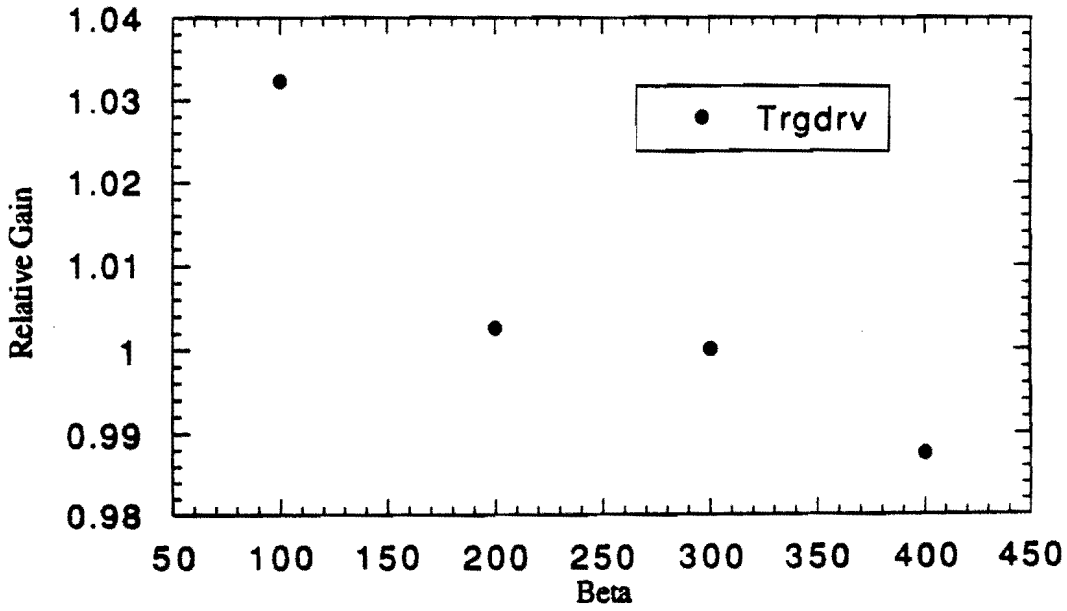

Figure 3.6b SPICE calculation of trigger driver beta effect, The differences are normalized to the beta = 300 point.

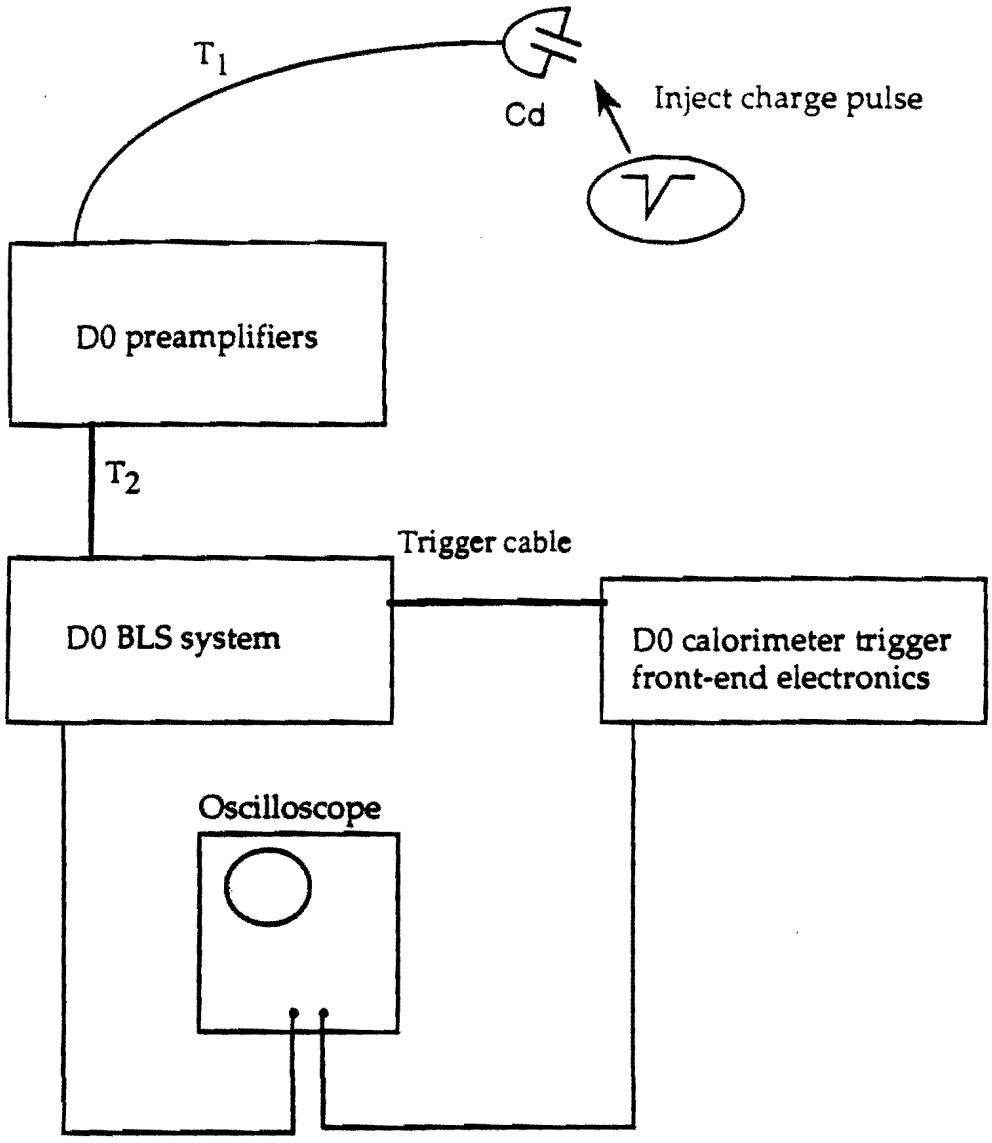

Figure 3.7 New York University D0 calorimeter electronics test bench. We use an oscilloscope to measure the trigger and BLS responses to a fixed size triangle charge pulse.

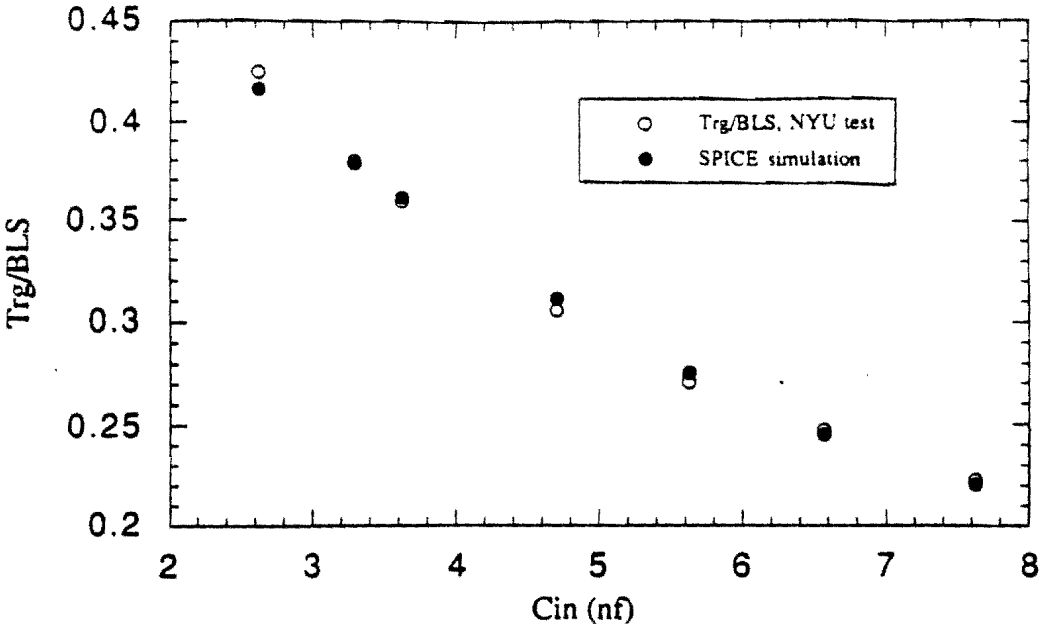

Figure 3.8a NYU test bench data

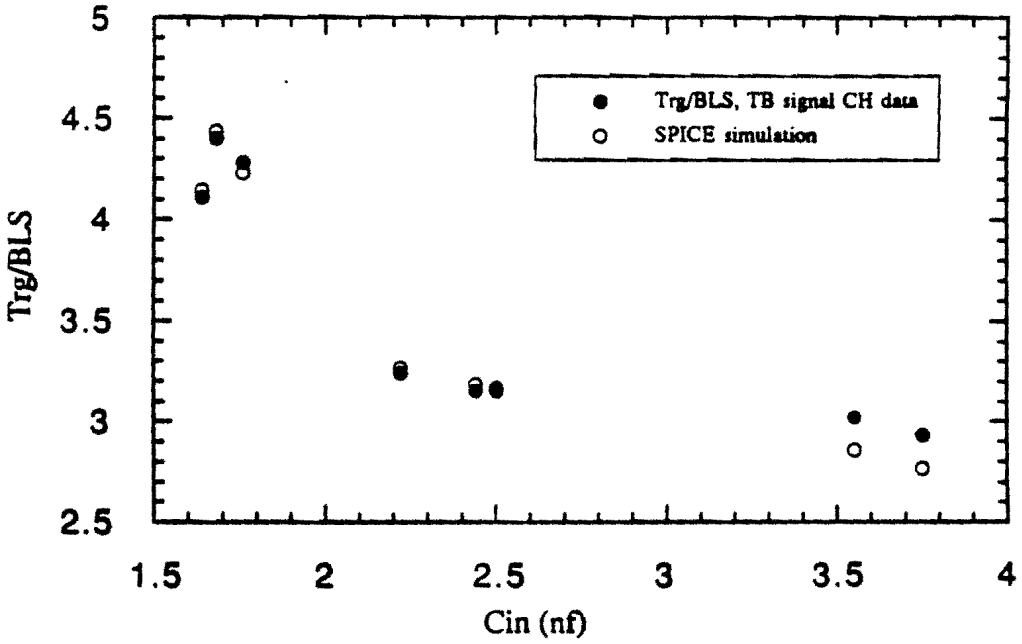

Figure 3.8b Load one single channel trigger test data

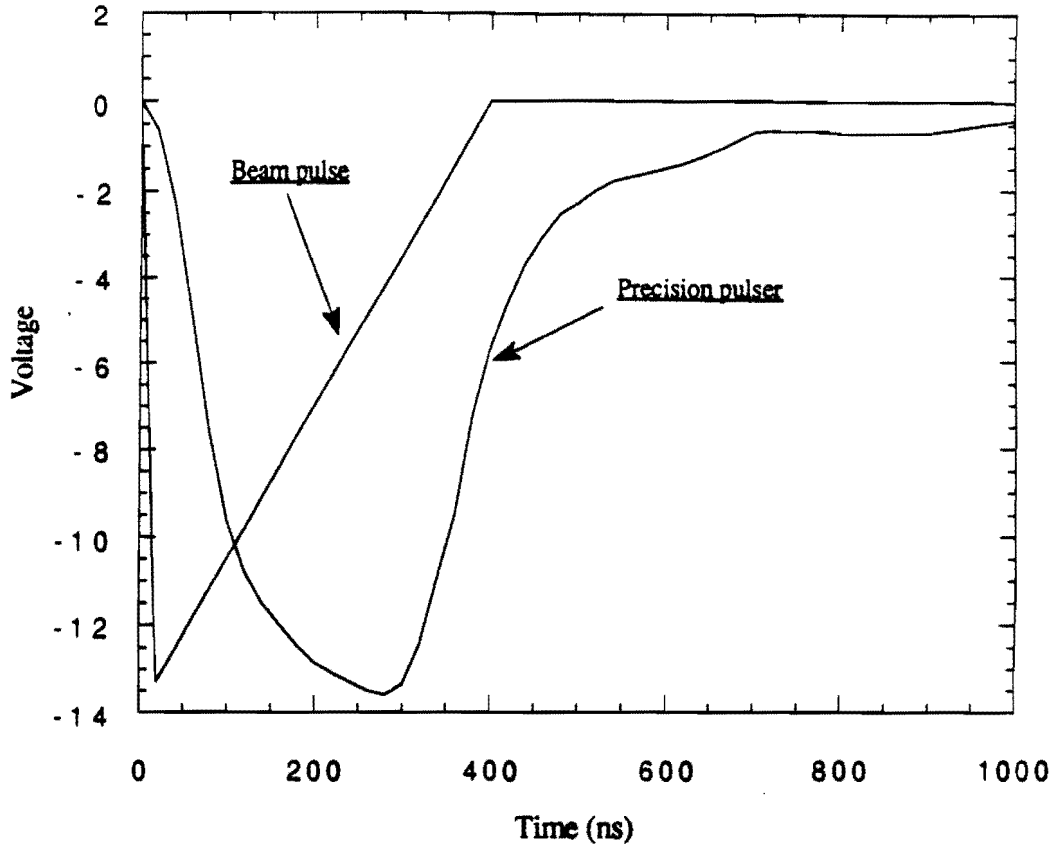

Figure 3.9 Calorimeter beam pulse and calibration pulser pulse shape

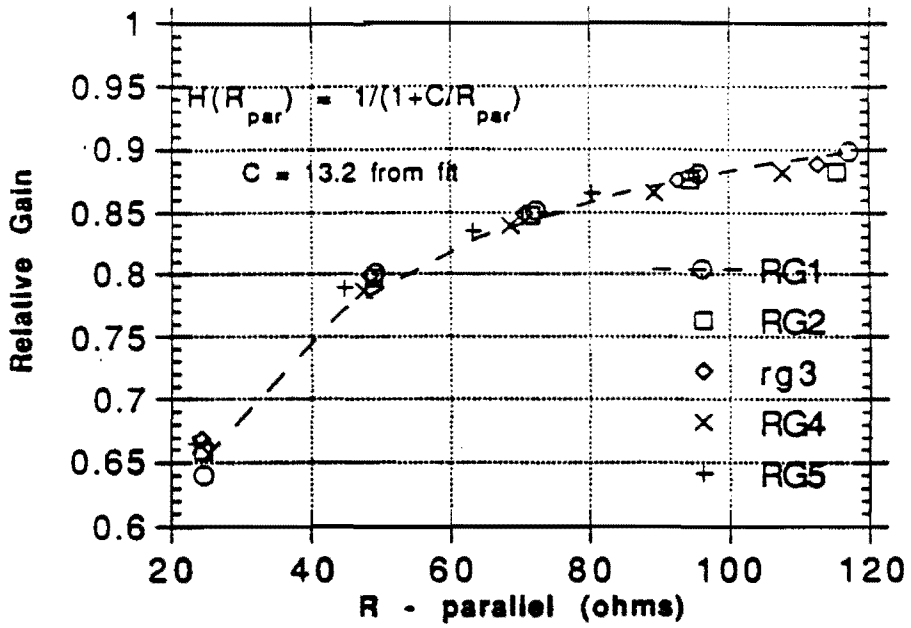

Figure 3.10 Trigger adder gain vs. total parallel input resistance.

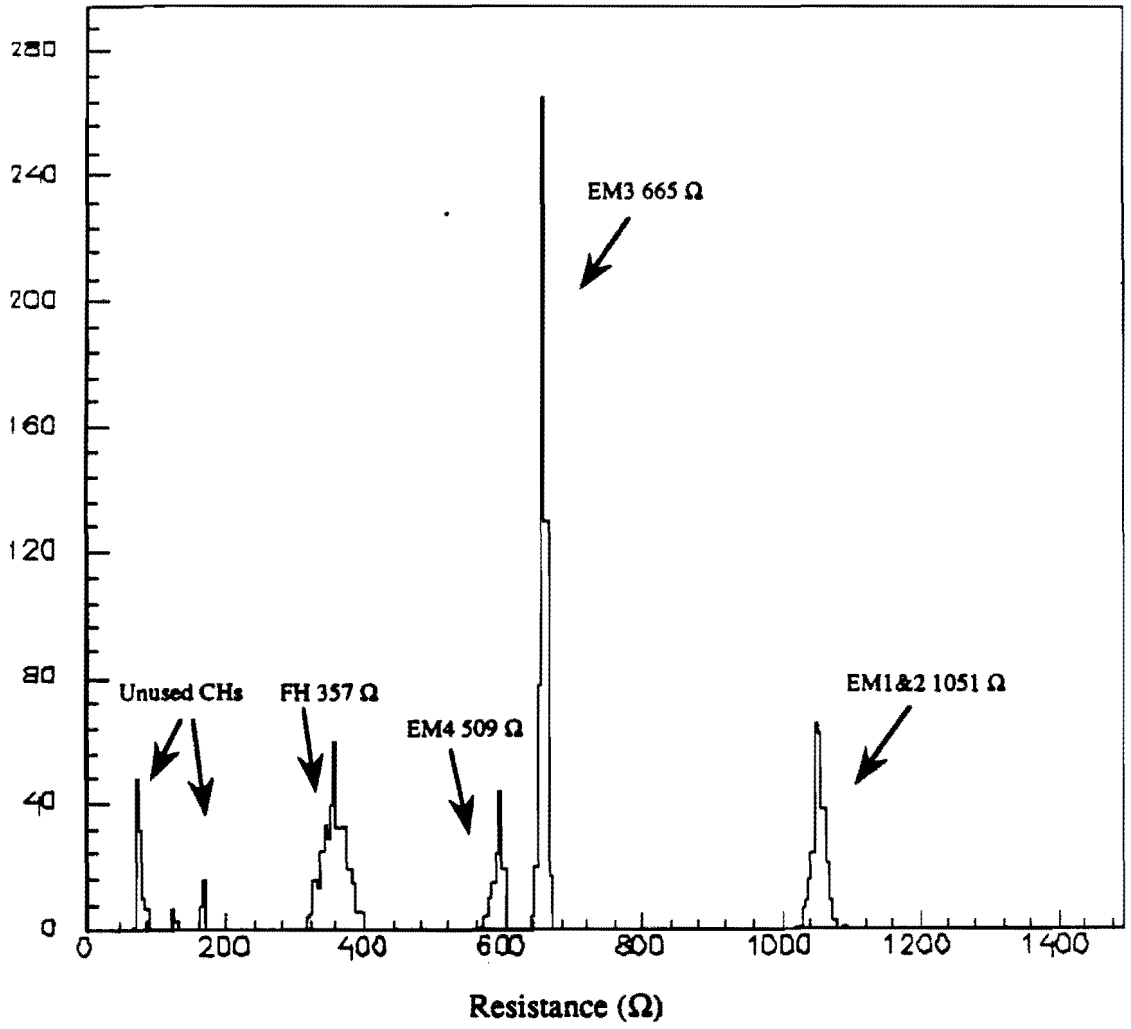

Figure 3.11 Distribution of the load-two trigger summing resistor

Chapter 4
D0 test beam experiment

4.0 General information, history of test beam experiment.

In order to verify the D0 calorimeter performance, test the electronics system, and provide the calibration for the collider experiment, there is a test beam facility to expose the D0 calorimeter modules to high energy electron and pion beams. The electronics system for the test beam is a copy of the D0 electronics system. Figure 4.1 shows the test beam cryostat, which provides the cryogenic container for the liquid Argon, as a large vessel on a transporter, which can move and rotate in three dimensions. The test modules are installed in the cryostat. By moving and rotating the transporter, we can expose different parts of the detector modules to the beam. There is a cryogenic feed-through port on the top of the cryostat, which provides a path for the electrical signals from the calorimeter module cells to the preamplifiers. The preamplifiers are installed on the upper corner of the cryostat. This layout minimizes the cable length between detector cells and preamplifiers. The electrical signal path from the detector cells to the ADC and the data acquisition (DAQ) system is shown in Figure 3.1.

There have been three test beam runs to test the D0 calorimeter module design and performance. The basic beam line instrumentation is the same for all these test beam runs, and it will be described in the following sections. This dissertation is a result of the two most recent test beam runs (1990-1992 load-one and load-two). Figure 4.4

shows the relative D0 geometric coverage of these two test beam runs. We will show briefly the module configurations of these two runs.

4.1 Beam line magnets and target wheels

The D0 test beam experiments use the Fermilab's Neutrino West (NW) secondary beam line. The layout of the NW beam line is shown in Figures 4.2 and 4.3. The primary target is in enclosure NW4, and the secondary beam is transported to experimental hall (NWA) through horizontal (east/west) bends in NW6, NW7, and NW9, with focusing elements in NW4 and NW8. To create a relatively pure electron beam, a sweeping magnet NW4S is used to remove all the charged particles, in conjunction with the insertion downstream of NW4 Lead target wheel NW4PB to convert photons. Alternatively, a relatively pure pion beam can be obtained by disabling the sweeping magnet and removing NW4PB target, and inserting Lead converters in NW6 (NW6PB) and/or NW7 (NW7PB) to preferentially scatter electrons from the beam. The final bend magnet NW9E is instrumented with a Hall probe to measure the magnetic field during the beam spill. This gives us the measurement of the beam momentum spread.

4.2 Beam trigger, veto and tags

The beam trigger signal is made of a triple coincidence of scintillators, S1, S2 and S3. The scintillator array has a 5"x5" hole in the center to serve as a halo veto. There are several other vetoes to inhibit trigger pulses. One is the calorimeter MOVING veto, which vetoes any trigger if the transporter is moving. It limits any electrical and mechanical noise that could be generated with such movement. Another is a DEAD-TIME veto, which holds any further triggers for 6 μs if a beam trigger fired. It is used to avoid multiple Base/Peak sampling. If the event is accepted, there is a 10 ms dead time veto to stop any action, and wait for the DAQ system to finish reading out all the data. Along with all the vetoes, there are several tags to monitor the beam (Figure 4.3).

The Mips tag is located directly behind the cryostat to tag particle leakage, and the Muon tag is located behind the steel absorber, to tag muons. Several Cerenkov counters are recorded as Cerenkov tags for electron identification. These are two helium Cerenkov counters (NW9CC, NWACC1), and a 3 meter long Nitrogen Cerenkov counter (NWACC2).

4.3 Proportional wire chamber tracking and Beam momentum calculation

Several Proportional wire chambers (PWC's) were installed in the beam line to determine the beam particle trajectories on an event by event basis. Their positions are shown in figure 4.3. The chambers were Fermilab standard "Fenker" chambers. Each chamber had one or two planes of 128 wires. All of the chambers we used had 1 mm wire spacing. There are total of 11 planes: 6 recording horizontal and 5 recording vertical positions. The chambers were nearly centered on the beam line, and very small adjustments were needed from beam alignment studies. Event by event momentum calculation was based upon the bend angle, measured with PWC tracks, and the NW9E magnetic field, measured from the Hall probe or by relating the NW9E read back current to the field integral. The accuracy of the momentum is limited by the measurement of the field integral BxL (B is the magnetic field and L is the length of NW9E magnet), to about 0.2%; and the precision on an event basis is about 0.25% from the PWC track resolution[22]. The RMS of the beam momentum spread is typically 1.5%, with reasonably Gaussian profiles[22].

4.4 Test beam load–one configuration

The load one test beam included an end calorimeter electromagnetic (ECEM) module, an end calorimeter inner hadronic (ECIH) module and an end calorimeter middle hadronic (ECMH) module. The ECEM and ECIH modules were arranged in the

relative positions that they have in the D0 detector, and the ECMH module was placed behind the beam hole of ECEM and ECIH modules. Figure 4.5 shows the layout of the modules in the test beam cryostat. By moving and rotating the cryostat, we could send beam to the different projective towers of the modules.

4.5 Test beam load–two configuration

The load–two test beam included four central calorimeter electromagnetic (CCEM) modules, two central calorimeter fine hadronic (CCFH) modules, two central calorimeter coarse hadronic (CCCH) modules, two ECMH and end calorimeter outer hadronic (ECOH) modules, and massless gap and inter cryostat detector (ICD) modules. These modules were arranged as they are in the D0 calorimeter. Figure 4.6 shows how the central calorimeter modules were positioned in the test beam cryostat. This arrangement makes up one eighth of the D0 central calorimeter (Figure 2.4) and the CC/EC transition region. Figure 4.7 shows the (η, ϕ) mapping of this test configuration with the D0 calorimeter (η, ϕ) coordinates, where η is in pseudo-rapidity unit, and ϕ is in the D0 index unit (it is $10\frac{2\pi}{64}\phi$, ϕ is the azimuthal angle in radian). I will use the same (η, ϕ) unit throughout this dissertation. For this study, we only use the data taken with the central calorimeter, shown in Figure 4.7 as shaded regions, and only the region marked as "trigger coverage" was instrumented with calorimeter trigger electronics. Two points where the energy scan data were taken are marked on the map.

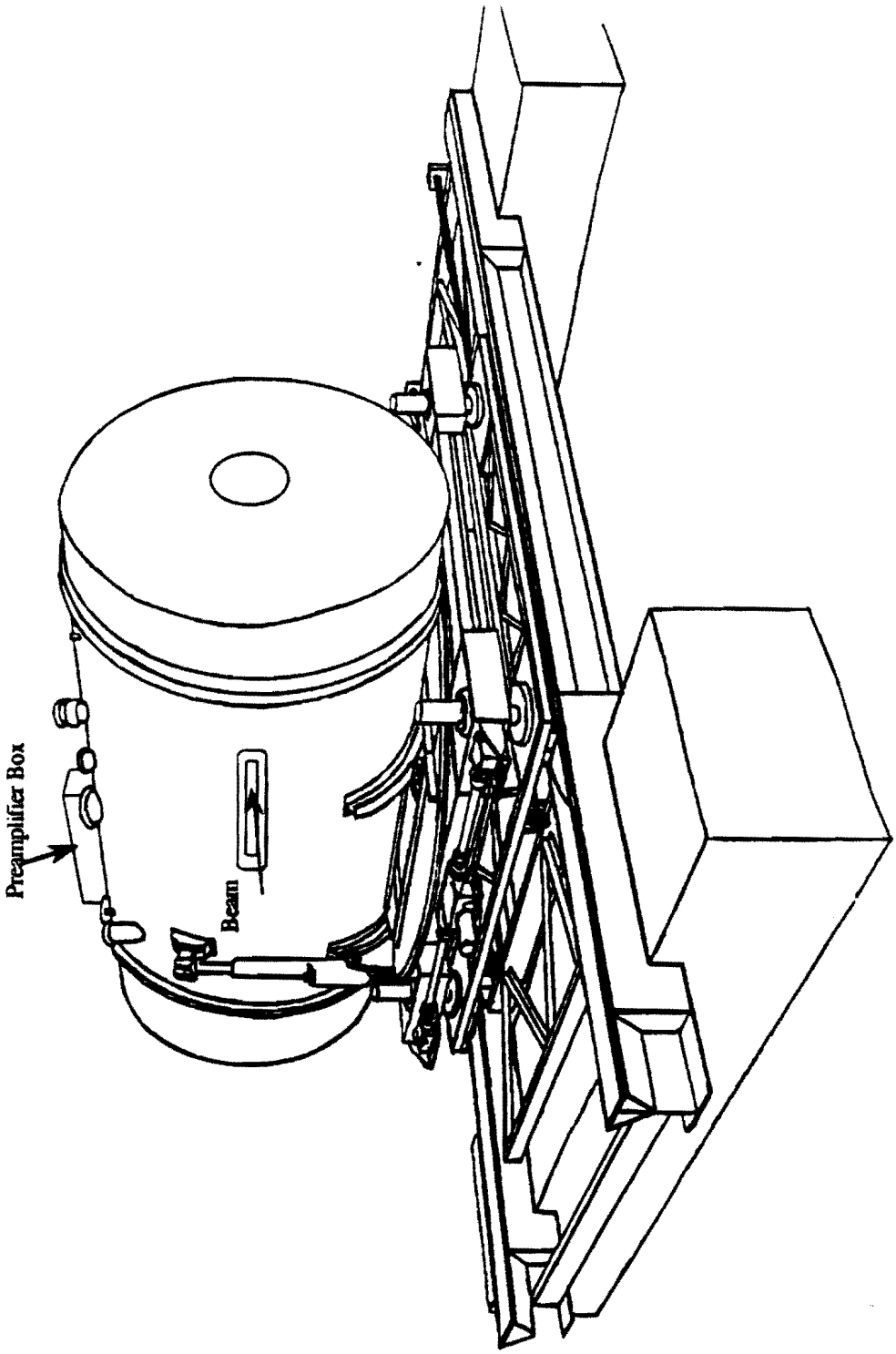

Figure 4.1 D0 test beam cryostat and transporter

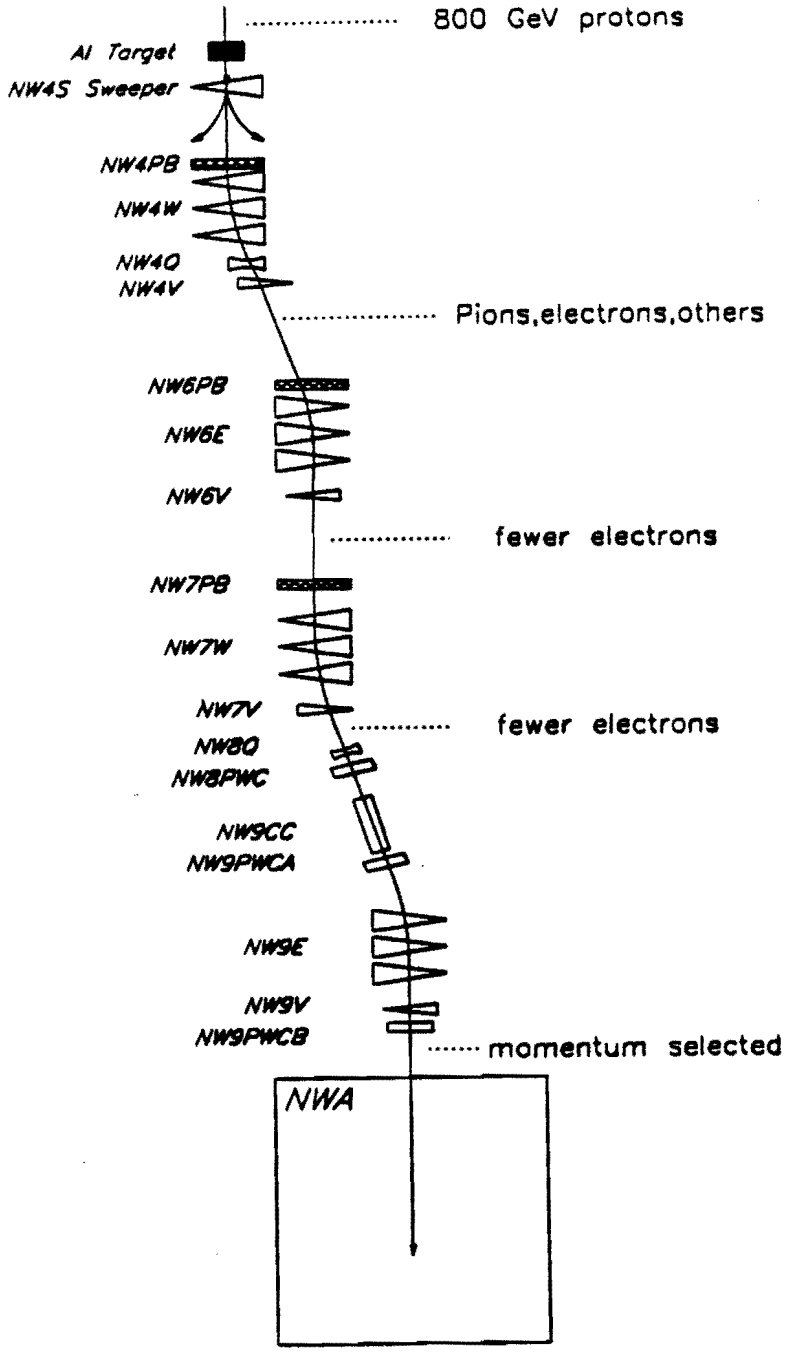

Figure 4.2 Fermilab NWA beam line

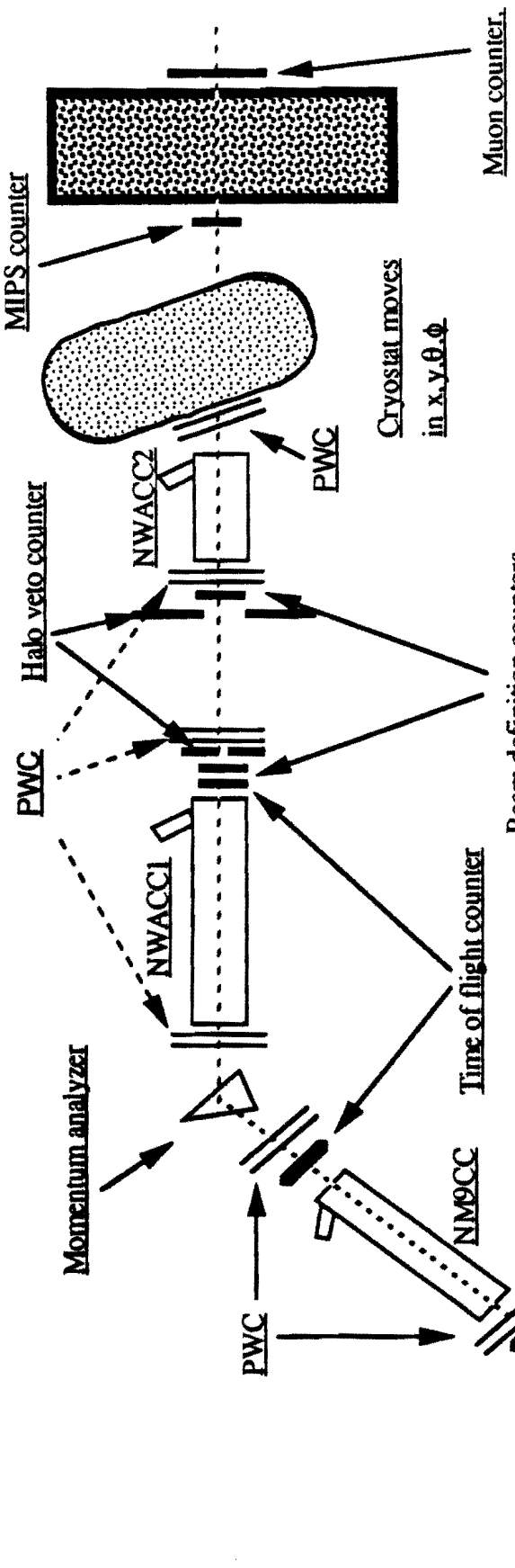

Figure 4.3 D0 Test Beam Beamline Schematic

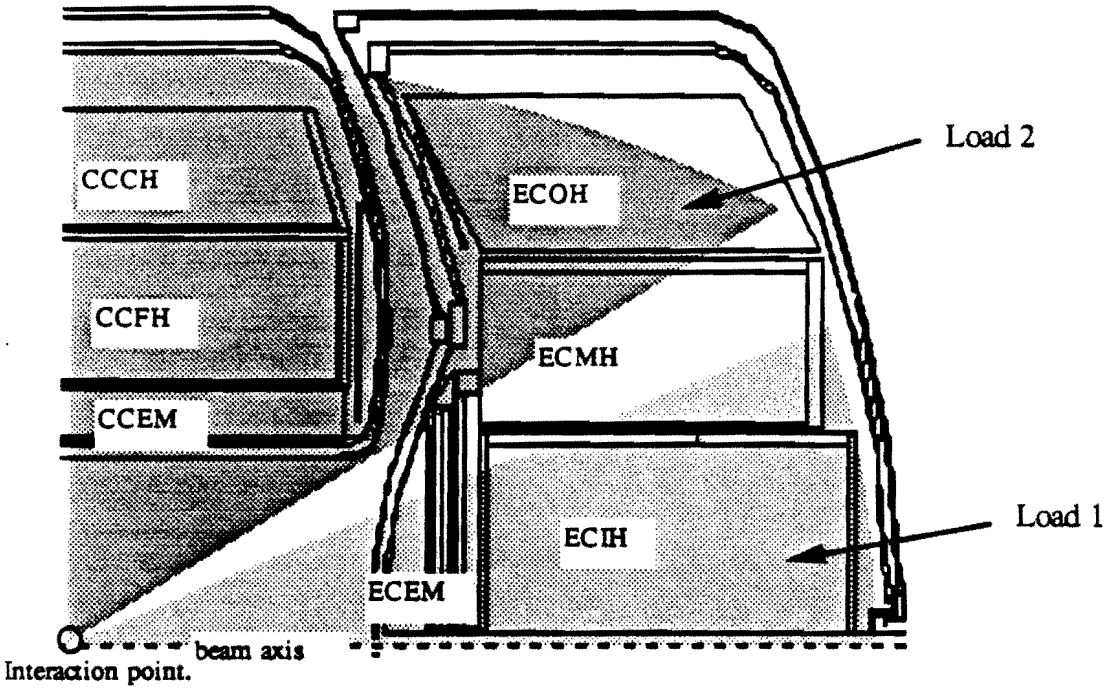

Figure 4.4 D0 calorimeter test beam scan region

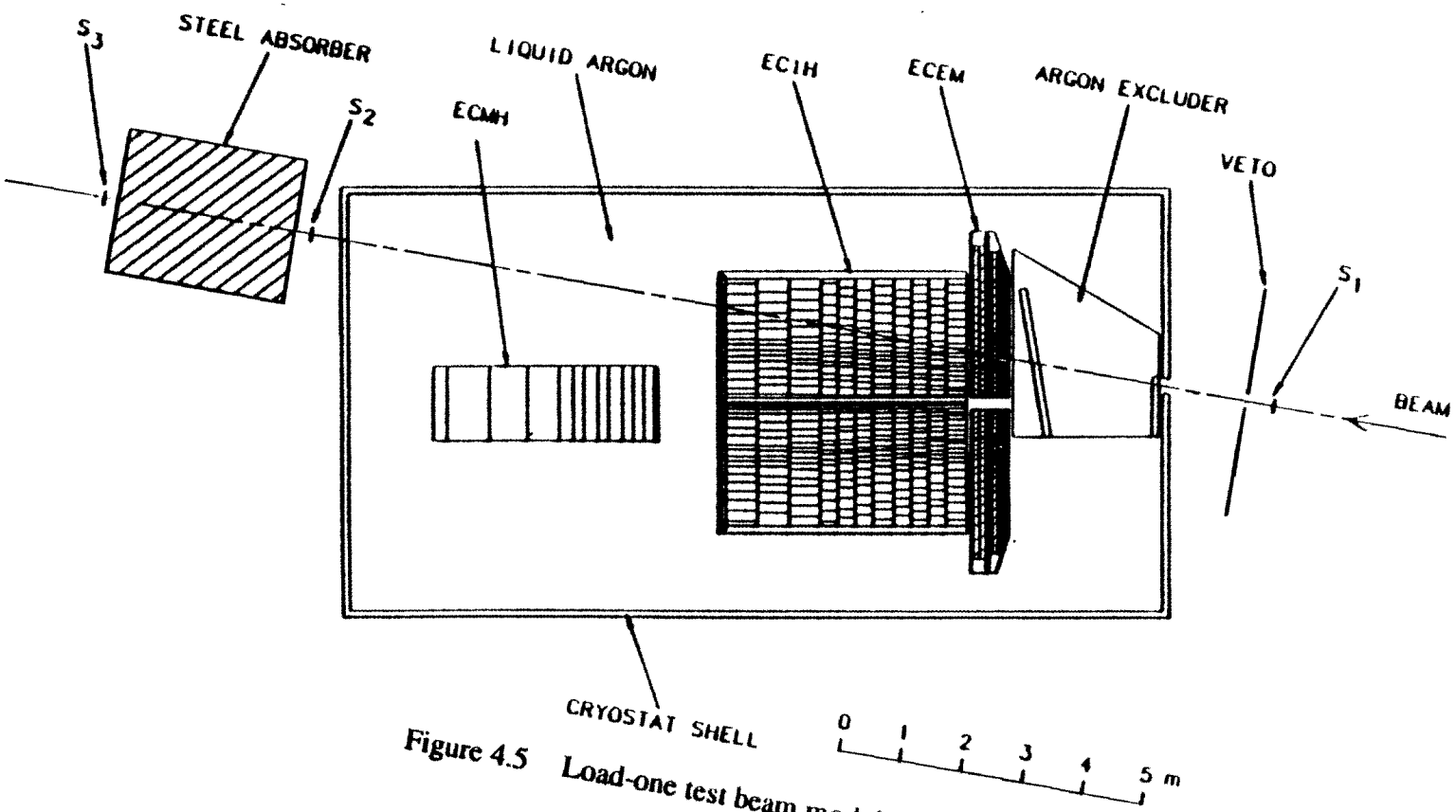

Figure 4.5 Load-one test beam module configuration.

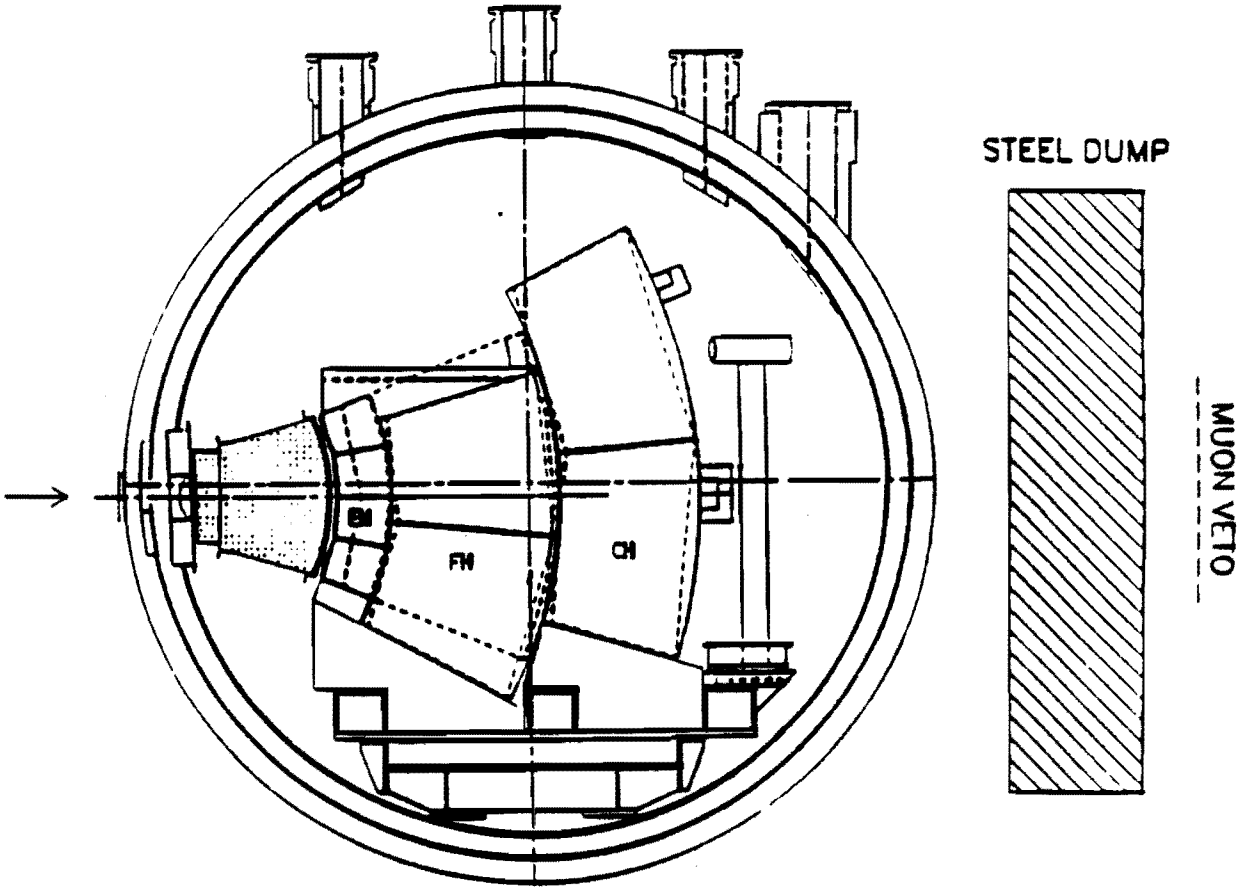

Figure 4.6 Load-two test beam module configuration.

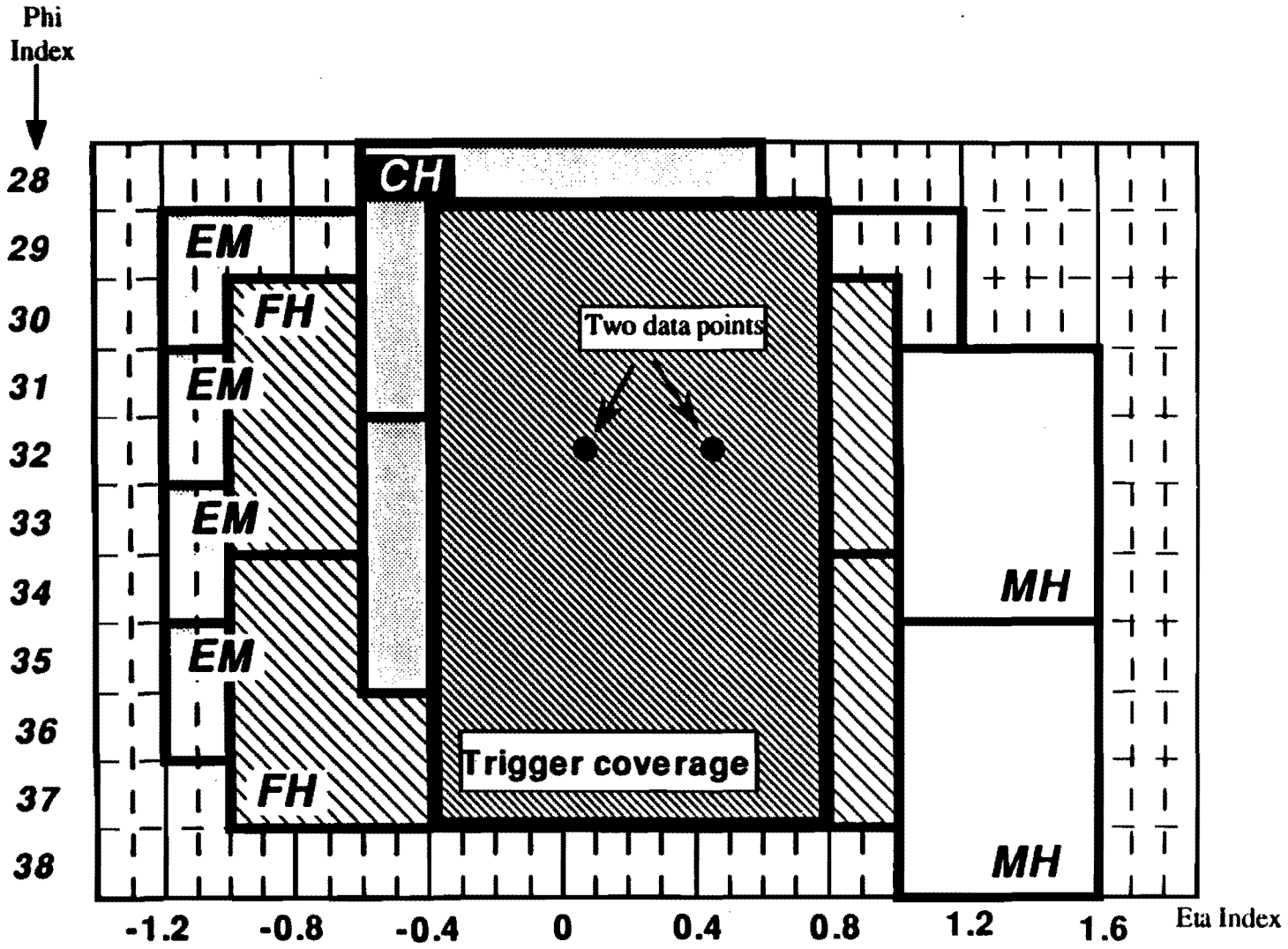

Figure 4.7 Load-two module coverage

Chapter 5
Test beam measurement

We took a large amount of data from the two loads of calorimeter modules. But we did not take useful data for the energy scan study with the trigger electronics when the load-one data was taken. This dissertation is an analysis of the load-two data. In this Chapter, I will present the load-two energy scan measurement with both trigger readout (TRG) and precision readout (BLS). I will also include published results of the load-one energy scan measurements for comparison. In order to understand the systematic error of the TRG, special data were taken to study the gain variation of the TRG. I will show the analysis of these data, and discuss the corrections I need to apply.

5.1 The general information of the load-two analysis.

In order to measure the e/π ratio, precision energy measurements of both electrons and pions are needed. The electron and the pion showers are intrinsically different. The electron showers are physically small, and measured in radiation lengths. The pion showers are relatively large, and measured in interaction lengths, which are usually 20 times larger than radiation lengths in most materials. The measurements for electrons and pions are done with different regions of detector and electronics channels. To precisely measure the e/π ratio, we have to be able to understand the uniformity of the detector response and correct for the energy leakage due to the large pion showers. However, to compare the e/π ratio difference between the fast trigger readout (TRG) and precision readout (BLS), only the uncertainties of the electronics need to be

considered. Because both readout systems are connected to the same detector region, the uncertainties caused by the detector defects are canceled out by taking the difference of the e/π ratios measured with the TRG and BLS. Therefore, we expect that the e/π ratio measurement will have an uncertainty dominated by the non-uniformity of the detector response, and energy leakage, whereas, the e/π ratio difference between the BLS and TRG will be insensitive to these factors. The uncertainty of the e/π ratio difference will be dominated by the uncertainty in the trigger electronics, since the uncertainty of the precision electronics is much smaller.

The physical reason for the e/π ratio difference between the TRG and BLS is that there is a slow signal component in the hadron shower in the Uranium-liquid Argon calorimeter. As the electron shower is almost instantaneous (finished within a few ns), the electron responses of the TRG and BLS should be the same. Using this principle, I can calibrate the TRG with the BLS data. This eliminates most of the uncertainties in the fast trigger electronics, such as the gain vs. capacitance correction and the gain variation of the trigger towers. With calibrated TRG, any difference of the e/π ratio measurements with the TRG and BLS can be attributed to the slow signal component of the pion showers in the Uranium-liquid Argon calorimeter. Figure 5.0 shows the SPICE simulation of the BLS and TRG responses to electron and pion showers. The electron shower generates a perfect triangular pulse at preamplifier input, shown with dashed lines; whereas the pion shower generates a triangular pulse with a tail at the preamplifier input, shown with solid lines. The input capacitance of the simulation is 2.0nf, and the total charge of the two input pulses is normalized. The Figure shows that the BLS is not sensitive to the input pulse shapes. Its response is the same regardless of whether the input pulses have a tail or not, whereas the TRG is different, its response being very sensitive to the leading edge of the input pulse. There are a few corrections that I need to apply to the data. These are described in detail in the following sections.

All the energy measurements shown in this dissertation are done with the following methods:

(1). The BLS data are pedestal subtracted and gain corrected. The pedestal of each channel is determined by analyzing the data taken without the beam, and the gain of each channel is determined by analyzing the data taken with the precision calibration pulser.

(2). All the beam events are required to have a good beam track (both X and Y), and a beam momentum reconstruction. Cuts are applied to the beam track position (X, Y cuts) on an event by event basis to avoid the cracks of the detector.

(3). The electron cluster is defined as the sum of 6x6 cells in the (η, ϕ) dimension (approximately 45x45 cm^2 in the front of the CCEM). The BLS electron energy measurement includes energies in all the CCEM layers and the first CCFH layer. The TRG electron energy measurement includes the EM trigger towers and the leakage energy in the first CCFH layer measured by the BLS. To minimize the systematic uncertainty, the electron energy measurement for the e/π ratio study uses the same cluster as the pion's.

(4). The pion cluster is the sum of 10x8 cells in the (η, ϕ) space (approximately 78x60 cm^2 in the front of CCEM). The BLS pion energy measurement includes energies in all the central calorimeter layers. The TRG pion energy measurement includes energies in both EM and HD trigger towers and leakage energy in CCCH measured by the BLS. There is a longitudinal leakage cut on the energy in the CCCH (E_{ch}) that is $\frac{E_{CH}}{E_{total}} \leq 25\%$.

(5). The energy in different detector layers is weighted by $\frac{1}{S_i}$ (S_i is the sampling fraction of the layer i) before it is summed together.

5.2 Corrections

5.2.1 Non-linearity of the trigger cable differential driver.

The fast trigger signals are summed into the trigger towers on the BLS cards, and sent to the CTFE (calorimeter trigger front-end) cards through the trigger cable differential drivers (TrgDrv) (shown in Figures 3.2 and 3.3). The TrgDrv is not a perfect linear amplifier over the large dynamic range required. Using the standard D0 precision calibration pulser, the linearity of the TrgDrv can be measured with the test beam electronics. Only one preamplifier channel with small detector capacitance was added to the trigger tower in order to limit the noise. The result is shown in Figure 5.1a, and can be fitted with a simple power law. From this power law relation, the following correction can be applied to the raw trigger data to eliminate the non-linearity.

$$E_{TRG\_corrected} = E_{TRG\_raw}^{0.980}$$

Figure 5.1b shows the TRG/BLS ratio of electron energy scan data before and after this correction. The simple correction improves the linearity to within $\pm 1\%$.

The uncertainty of the exponent in the correction is 10%, derived from the fit. I will show how this uncertainty affects the e/π ratio measurement. The following relations apply among the raw data (X), corrected energy (E), non-linearity deviation (α), and uncertainties of these parameters $(\delta E, \delta\alpha)$.

$$E = X^{1-\alpha} \text{ and } \delta E \approx -\delta\alpha E \ln(X) \quad \alpha \approx 2\% \quad \frac{\delta\alpha}{\alpha} \approx 10\%.$$

Since the e/π ratio is close to one, if the electron and pion showers share the same trigger towers, then any uncertainty of the e/π ratio measurement caused by the uncertainty of exponent correction is canceled. But in reality, electron showers are mostly contained in one trigger tower and pion showers are spread over several trigger towers. I assume a worst case scenario where the pion showers are spread evenly among 10 trigger towers, the uncertainties of the exponent are the same for all trigger towers. Here I assume that the exponent uncertainty is systematic rather than random. Then the uncertainty of the e/π ratio measurement caused by the uncertainty of the exponent correction can be calculated as follows.

$$E_e = X_e^{1-\alpha}, \quad E_\pi = \sum_{i=1}^{10} \left(X_\pi^i\right)^{1-\alpha}.$$

Since $E_e \approx E_\pi$ and $\alpha << 1$, I have $X_e \approx 10X_\pi^i$.

Assuming the exponent correction has a deviation of $\delta\alpha$ from the actual correction, the e/π ratio measurement caused by the exponent correction deviation can be calculated

$$\frac{E_e}{E_\pi} \approx \frac{E_e - \delta\alpha E_e \ln(E_e)}{\sum_{i=1}^{10}\left\{\left(\frac{E_\pi}{10}\right) - \delta\alpha \frac{E_\pi}{10}\ln\left(\frac{E_\pi}{10}\right)\right\}} \approx \frac{E_e}{E_\pi}(1 + \delta\alpha \ln(10)).$$

Thus, the uncertainty of the e/π ratio measurement caused by the uncertainty of the exponent correction is $10\%\alpha\ln(10) \approx 0.46\%$.

5.2.2 Sampling fraction correction

The sampling fraction of the detector is calculated using Formula 2.1, except for the first layer of the CCEM. There is a large amount of extra material (the cryostat walls are equivalent to about $2X_0$) in front of the CCEM module that needs to be included in the sampling fraction calculation. The method we used was to include the front

material in the first EM layer sampling fraction. Because of the nonlinear characteristic of the longitudinal distribution[4] of the electron showers (the rapidly increasing energy deposition per radiation length at early part of electron showers), the effect of the extra front material on the electron energy measurement is nonlinear with energy also. From an empirical study[22], we found that by incorporating 60% of the front material into the first CCEM layer sampling fraction calculation, we can have good linearity and energy resolution of the electron response. The sampling fractions I used for the test beam are calculated this way.

The sampling fractions I used to calculate the trigger summing resistors were calculated initially without knowing the detailed geometry of the test beam modules and the front materials. Since then, updated information of the modules and front materials has become available. Table 5.1 shows both the sampling fractions used to calculate the trigger summing resistors and the updated sampling fractions. Because the trigger summing resistors are calculated with the imprecise sampling fractions, the energy from the raw trigger data needs to be corrected. I will show how to do this correction.

Detector layer	The trigger resistor sampling fraction	Correct sampling fraction
EM1	12.7%	9.04%[1] (10.94%[2])
EM2	12.7%	11.97%
EM3	12.7%	11.90%
EM4	12.7%	12.35%
FH1	7.0%	6.59%
FH2	7.0%	6.90%
FH3	7.0%	6.89%
CH	1.4%	1.45%

Table 5.1

I define two sets of sampling fraction weights $\{W_i^T\}$ ($W_i^T = \frac{1}{S_i^T}$, $\{S_i^T\}$ is the sampling fraction used to calculate the trigger summing resistors, the middle column of Table

[1] Include the front materials.
[2] Module only.

5.1) and $\{W_i\}$ ($W_i = \frac{1}{S_i}$, $\{S_i\}$ is the precision sampling fraction, the right hand column of Table 5.1). For a high energy particle, the real energy deposited in the calorimeter layer i is $\{e_i\}$ and the energy measured by the trigger readout in the calorimeter layer i is $\{e_i^T\}$. I assume that the energy measured by the precision readout (BLS) is the real energy, and that the energy measured by the trigger readout (TRG) is very close to the real energy. The TRG output which is actually recorded is $E_{TRG} = \sum W_i^T \cdot e_i^T$. The precision readout measures $\{e_i\}$, and I know the $\{W_i\}$ and $\{W_i^T\}$. I seek an expression which approximates $U_{TRG} = \sum W_i \cdot e_i^T$, the trigger energy if the trigger weights had been correct, using only know quantities. An approximate expression is

$$U_{TRG} \approx Q = \sum W_i^T \cdot e_i^T \cdot \left(\frac{\sum W_i \cdot e_i}{\sum W_i^T \cdot e_i} \right). \tag{5.1}$$

The term in the parentheses gives the correction factor for using $\{W_i^T\}$ instead of $\{W_i\}$ for precision readout $\{e_i\}$. This factor should really give the correction for TRG readout $\{e_i^T\}$, since the $\{e_i^T\}$ and $\{e_i\}$ are very close. Let $W_i^T = W_i + \alpha_i$, $|\alpha_i| << |W_i|$ and $e_i = e_i^T + \varepsilon_i$; $|\varepsilon_i| << |e_i|$, then

$$Q = U_{TRG} \cdot \left(\frac{\sum W_i^T \cdot e_i^T}{U_{TRG}} \right) \cdot \left(\frac{\sum W_i \cdot e_i}{\sum W_i^T \cdot e_i} \right) = U_{TRG} \cdot \left(1 + \frac{\sum \alpha_i \cdot e_i^T}{\sum W_i \cdot e_i^T} \right) \cdot \left(1 - \frac{\sum \alpha_i \cdot e_i}{\sum W_i^T \cdot e_i} \right) \approx U_{TRG},$$

when the second order terms are dropped.

If $\frac{\varepsilon_i}{e_i} \approx 5\%$ (from the e/π ration difference measurement, Section 6.2) and $\frac{\alpha_i}{W_i} < 10\%$ (which are mostly true, as in Table 5.1), the error of the Formula 5.1 is less than 0.5%. Formula 5.1 will be used to correct the sampling fractions of the trigger readout.

5.2.3 Crosstalk between fast trigger channels

We have observed crosstalk between trigger channels on the same BLS card. Figure 5.2 shows that if two channels have a small capacitive (C_C) coupling between them and if the input resistance of the amplifier is small, there will be a crosstalk signal with a relatively short time constant[20]. Since the sampling time of the trigger readout is much earlier than the precision readout (250ns vs. 2.2μs), the trigger readout could pick- up a large fraction of the crosstalk signal. Using pulser tests I have observed the crosstalk signal at the input of the first trigger tower adder. So the crosstalk signals are amplified by the trigger tower adders. Because the trigger response is sensitive to the pulse shape and injection point, the pulser system cannot be used to study the crosstalk quantity of the beam signal. The real beam data will be used to estimate the crosstalk effect on the trigger energy measurement.

I used electron energy scan data, and looked for "excess energy" in the HD section of a trigger tower, with large amounts of energy deposited in the EM section of the same trigger tower. The "excess energy" is the energy measured by the trigger readout minus the energy measured by the precision readout. Since the crosstalk in the precision readout is negligible, the energy measured by the precision readout is real energy deposited by the electrons. In Figure 5.3, I plot the "excess energy" in the HD section of a trigger tower vs. energy in the EM section of the same trigger tower. It shows that there is a crosstalk of 2.2% signal from the EM section to the HD section.

Because the cross talk reshapes the signal, the crosstalk could effectively change the trigger energy measurement. In order to estimate the crosstalk effect on the trigger energy measurement, I will examine two extreme cases. One is that the total signal is conserved; that is, one channel's gain from crosstalk must be another channel's loss. Another case is that the total signal is not conserved; that is, because of the crosstalk

reshaping the signal and the short trigger sampling time, one channel can pick up extra signal without the other channels losing any signal.

In the first case, if the amplification is the same between two crosstalking channels, the total energy should be conserved. However, the sampling fraction differences between the EM and the HD channels and the capacitance differences between these channels cause the amplifications applied to the EM and the HD channels to be different. The trigger summing resistors chosen for the trigger adder (Table 3.2) are: EM1 & EM2 = 1051Ω, EM3 = 665Ω, EM4 = 509Ω, and FHs = 357Ω. In the case of the crosstalk picked up in the HD channels from the EM channels, the crosstalk signal is amplified by a factor of 1.7, and for the crosstalk picked up in the EM channels from the HD channels, the crosstalk signal is amplified by a factor 1/1.7. For the electrons, most of the energy is deposited in the EM sections, and the test beam data (Figure 5.3) shows that the crosstalk will give the HD section 2.2% excess energy. This means that the crosstalk signal picked up before amplification by the trigger adders in the HD section from the EM section is $\Delta\varepsilon$=2.2%E/1.7 = 1.3%E. The energy measured by the trigger readout is $E_{trg} = (E - \Delta\varepsilon) + \Delta\varepsilon * 1.7 = E + 1\%E$, which is 1% higher than the real energy. For the pions, the energy will be shared between the EM and the HD sections. If I assume that the pion energy is evenly shared between the EM and HD sections, and the crosstalk factor between the EM and the FH section is the same as measured in the electron case, then the energy of the pions measured by the trigger readout will be $E_{trg} = E + (1.7 - 1 + 1/1.7 - 1) \cdot \Delta\varepsilon/2 = E + 0.2\%E$, which is 0.2% higher than the real energy.

In the second case, where the two crosstalk channels do not conserve energy, the crosstalk signal picked up in one channel will directly contribute to increase the total energy. Following the above calculation, I get for electrons: $E_{Trg} = E + 2.2\%E$, and for pions: $E_{Trg} = E + 1.5\%E$.

The real crosstalk mechanism will likely lie in between these two cases. I will correct the trigger energy measurement by the average of these two cases; that is, 1.6% for the electrons and 0.85% for the pions. I can estimate that in the worst case, the maximum uncertainty on the e/π ratio caused by the crosstalk effect is less than 0.65% and it is caused by the uncertainty in the crosstalk mechanisms.

5.2.4 The gain variation of the trigger electronics

From the electronics circuit analysis (Section 3.2), we expect a gain variation at the individual preamplifier channel level as well as at the trigger tower level due to the variation in the transistor's beta. The trigger differentiator's gain variation caused by the beta variation is about 3% for EM channels and 5% for HD channels. The trigger cable driver's gain variation is less than 1%. These are worst case estimates, assuming a uniform distribution of beta values. In the following section, I will use the test beam data to study these variations.

1) The individual trigger tower gain variation

Ideally, the ratio of the trigger readout (TRG) and the precision readout (BLS) would be a constant over the whole detector, because it is only electronics dependent. So I can use this ratio to measure the variation of the trigger electronics, provided that the gain variation of the BLS is negligible. I used 100 GeV electron trigger tower scan data with beam directed at different trigger towers to measure the ratio of the TRG and BLS. Figures 5.4a and 5.4b show this ratio distribution for 24 trigger towers with EM and HD sections. The measurements on the HD section are done by selecting the events in which electrons go through the cracks of the CCEM modules and deposit a significant amount of energy in the CCFH modules. Because I only use one kind of trigger summing resistor for the HD channels, and the HD channels' capacitance changes systematically over η and ϕ, I expect the HD channels' gain to have a systematic

dependence on the η and ϕ of the trigger tower. I corrected this systematic (η, ϕ) dependence by using FH layer one capacitance data of each tower to calculate a correction factor for the tower.

The trigger tower scan data (Figure 5.4) show that the distribution is not very Gaussian, so I will use the RMS to characterize the data. For the EM trigger towers the RMS of the gain is 5.1%. For the HD trigger towers the RMS of the gain is 8.3%. The statistical uncertainty of each EM trigger tower gain measurement is less than 1.0%, and the statistical uncertainty of each HD trigger tower gain measurement is less than 2.0%.

These gain variations of the trigger towers are larger than expected. From the energy resolution study (next Section) and the SPICE simulation of the beta effect[Section 3.2], we expect that the trigger tower gain variations caused by the electronics are less than 3% for the EM towers and 5% for the HD towers. These expected variations are smaller than the ones shown in Figure 5.4. We found that the problem was in the trigger cable driver (Figure 3.3). The output coupling capacitors (C7 & C8) of the trigger cable drivers are defective. These capacitors are unstable, develop large leakage currents, and have a short life time (months). We overlooked this problem during the test beam experiment, but later, we had the opportunity to study the long term behavior of these trigger cable drivers at D0. We observed that the trigger tower's gain changed in the course of a few weeks, and that the trigger towers with significant gain change will go totally dead, caused by the shorting of these coupling capacitors. The rate of these failures is nearly a half percent per week. Normally, this type of capacitor has a leakage current of a few to tens of μA. Using SPICE simulation, we have seen more than a 10% gain change if the leakage current increases to 2 mA. Based on what we have observed at D0, we believe that some channels developed large leakage currents

which caused the larger than expected trigger tower gain variation observed at the test beam. The trigger tower gain variation can be expressed as:

$$\sigma_{tower} = \sqrt{\sigma^2_{preamp} + \sigma^2_{Cap} + \sigma^2_{TrgDrv}},$$

where σ_{preamp} is the fractional gain variation due to the preamplifier transistor beta variation (more discussion on this can be found in the following section). From the SPICE simulation, it is about 3% for the EM channels and 5% for the HD channels. σ_{Cap} is the gain variation due to the capacitance correction. After applying tower by tower capacitance correction for HD towers, this term is less than 2% for both EM and HD towers. σ_{TrgDrv} is the gain variation due to the trigger cable driver, which we believe is mostly caused by the defective capacitors. Using the data from Figure 5.4, I can conclude that the EM trigger tower variation is dominated by σ_{TrgDrv}, and the large HD trigger tower variation is caused by a combination of the large σ_{preamp} term and the σ_{TrgDrv} term.

All of the test beam data I used for this dissertation were taken during a one and a half week period. During this short period, the change of the trigger electronics gain due to the change of the leakage currents of the coupling capacitors should be very small. I can use the trigger tower scan data to correct the energy scan data to eliminate the large trigger tower gain variation. Furthermore, the electron and pion energy scan data at the same energy were taken consecutively, so any time dependence of the trigger electronics gain will be canceled in the e/π ratio measurements.

2) Individual preamplifier channel gain variation.

In the previous section, I have discussed the trigger tower gain variation observed using electron trigger tower scan data. From the SPICE simulation, I expect that the beta of the preamplifier's output driver transistor and the capacitance of the feed back capacitor

will affect the trigger gain. But there is no direct measurement of these effects with the trigger data, because the trigger tower is the sum of many preamplifier channels. I will use the calorimeter energy resolution to estimate the gain variation due to these factors.

The method is the following. As mentioned early, the calorimeter fractional energy resolution can be parametrized as

$$\left(\frac{\sigma}{E}\right)^2 = C^2 + \frac{S^2}{E} + \frac{N^2}{E^2} \tag{5.1}$$

where σ is the variation by fitting the energy distribution with a Gaussian, E is the energy of the beam, C is the constant contribution from systematic errors such as gain variation, S is due to the statistical error in the energy sampling, and N represents energy independent contributions to σ such as electronics noise. Assuming these parameters to be independent, and fitting the resolution vs. energy relation with (5.1), I can determine the constant term, which gives an upper limit of the gain variation. The results of the fit on the electron and pion energy scan data of both the BLS and TRG are shown in Figure 5.14. All the energy measurements are done by using the methods described in section 5.1. The gain of individual trigger towers is corrected using the 100 GeV electron trigger tower scan data. This eliminates the contribution of the trigger cable driver's gain variation. The sampling fraction correction (Section 5.2.2) is applied to the trigger data. The noise term in the fit is fixed using the pedestal data taken within the beam spill, and the sampling term for the trigger data is fixed to the precision readout sampling term. The results of the fits are shown in Table 5.2.

	Electron data BLS	Electron data TRG	Pion data BLS	Pion data TRG
C	0.33% (0.1%)[1]	1.52% (0.1%)	3.80% (0.2%)	4.59% (0.3%)
$S(\sqrt{GeV})$	14.6% (0.2%)	14.6%[2]	45.5% (1.1%)	45.5%[2]
N(GeV)[3]	0.44	1.3	1.7	2.7
χ^2	1.9	2.8	4.0	1.9

Table 5.2

It can be seen that the constant term difference between BLS and TRG readout is rather small. The larger constant term of the TRG is the result of the larger gain variation of the TRG. In order to get a quantitative estimate of the gain variation from the constant term of the resolution fit, one has to understand the relation between the gain variation and energy resolution.

If I assume that the fractional gain variation is σ_{gain}, and that the particle showers distribute their energy uniformly among n cells, the variation of the energy measurement due to gain variation will be $\frac{\delta E}{E} = \frac{\sigma_{gain}}{\sqrt{n}}$. For different types of particles, n will be different. In order to understand how the gain variation contributes to the energy resolution, it is necessary to know the energy distribution of the particle showers.

The BLS data were used to study the effect of the gain variation on the energy resolution, and estimate the effective n of the electron and pion showers. Assuming that the BLS data is free of gain variation after gain correction using the calibration pulser data, I artificially introduce gain variation to the BLS data by randomly generating a set of gains with fractional variation of σ_{gain} relative to the normal gain.

---

[1] The number in the parentheses is the error from the fit.
[2] Fixed to the precision readout sampling term.
[3] The noise term uses the measured noise from the pedestal data.

Figure 5.5 shows the energy distributions of 100 GeV electrons and pions with artificial gain variations of 10% and 20%.

For the electron shower, the average transverse shower size is much smaller than the calorimeter cell size[4] and longitudinal shower distribution is nearly constant. In the CCEM the longitudinal fractional energy distribution is approximately 10%, 15%, 50% and 25% among CCEM layers 1, 2, 3, and 4. So the majority of the energy from the electron shower will be deposited in 2 to 3 cells. Because of the small number of cells and the small fluctuation of the electron shower, the gain variation of cells will cause the energy distribution to deviate from a Gaussian distribution. This effect is shown in Figure 5.5. I choose an effective $n \approx 2.5$ for the electron shower.

For the pion shower the situation is more complex, because the average pion transverse shower size is larger than a few detector cells, the energy distribution is very uneven and fluctuates greatly from event to event. The simple analysis of the electron shower would not work for finding an effective n for the pion shower. The effect of the gain variation on the energy resolution can be parametrized as:

$$\sigma_\pi = \sqrt{\sigma^2_{\pi\_\text{intrinsic}} + A^2\sigma^2_{gain}}, \tag{5.2}$$

where $\sigma_{\pi\_\text{intrinsic}}$ is the intrinsic detector pion resolution without gain variation, σ_{gain} is the fractional gain variation , σ_π is the pion energy resolution with the fractional gain variation σ_{gain} , and A is a parameter ($A = \frac{1}{\sqrt{n}}$). Figure 5.6 shows a plot of the relative resolution vs. relative gain variation for the 100 GeV pions. Fitting the plot with (5.2), I get $n \approx 5$.

With the above model, I can extract gain variation information from the energy resolution fit. For the electron energy scan, the BLS and TRG constant terms are 0.3% and 1.5%. Thus the EM TRG channel's gain variation is smaller than

$\sqrt{2.5}*1.5\% \approx 2.4\%$. For the pion energy scan, the TRG constant term is 4.6% and the BLS constant term is 3.8%. Considering the gain variation as the only source of the TRG's larger constant term[1], the gain variation of the HD TRG channels will be:

$$\sqrt{5}*\sqrt{0.046^2 - 0.038^2} \approx 5.8\%.$$

This result is close to the previous estimate using the limits of the transistor's beta value and the SPICE simulation (Section 3.2.3).

In summary, using the test beam electron trigger tower scan data and the electron and pion energy scan data, I am able to eliminate the large trigger tower gain variation due to the defective trigger cable drivers, and I am able to estimate that the individual trigger channel's gain variation due to the preamplifier's beta variation is less than 2.4% for the EM channels and 5.8% for the HD channels.

5.2.5 CCEM between module crack effect

All the CC modules have a region which is about 1cm wide on each side of the modules with a weak electric field. This happens because the high voltage resistive coat on the signal board does not extend all the way to the side of the module. Figures 2.5 and 2.6 show a CCEM module and the resistive coat structure. The electric field in the liquid Argon outside the resistive coat covered area will drop very quickly as shown in Figure 5.7. The free electrons in these regions will drift with a slower speed over a longer path. The slower drift speed and longer path will change the charge pulse shape on the input of the amplifier as shown in Figure 5.7. This pulse shape change will cause the fast shaping trigger signal to lose amplitude, as shown in Figure 5.0. This effect has been observed with the electron data as shown in Figure 5.8, which is a plot of the TRG/BLS ratio vs. Y (vertical) position of the beam. It shows that the ratio drops 50%

[1] There are other factors which would cause the trigger energy resolution constant term to be larger than the precision readout, such as a larger e/π ratio and extra signal loss due to the crack effect.

when the electron is shot at the CCEM crack. The modules are arranged as in Figure 4.6, with the cracks running horizontally. Figure 5.8b confirms this arrangement. It shows that the energy in the CCEM drops nearly to zero when the incident electrons are aimed at the crack.

For the TRG electron energy measurement, the cracks have little effect because the electron transverse shower size is much smaller than the CCEM module size[4]. If one selects the electrons away from the cracks, there will be only a very small fraction of energy (<1%) deposited in the crack region. However the pion transverse shower size is larger than the CCEM or CCFH module sizes, so the trigger energy measurement could lose signal if there is a significant amount of energy deposited in the CCEM and CCFH crack regions.

It is difficult to make a good estimate of how much energy is deposited in the CCEM and CCFH crack regions from pion data, but we can use Monte Carlo simulation to study this effect. Figure 5.9 shows the average energy distribution of 50 GeV pion showers in the azimuthal (ϕ) dimension based on the plate level test beam Monte Carlo simulation (Section 6.1). The figure includes the distribution of live energy (energy deposited in liquid Argon) in the EM and HD sections, and the distribution of total energy (energy deposited in all the materials) in the EM and HD sections. The inter-module cracks show up as valleys in the live energy distributions. If I integrate the total energy over the CCEM and CCFH crack regions, I find that the energy in the crack regions is 1.5% of the total energy in the detector. Assuming that the TRG only detects half of the BLS signal, I will correct the TRG pion response by 0.7% due to the crack effect. The uncertainty on this estimate depends on the precision of the detector Monte Carlo simulation. We have done a transverse shower distribution comparison between load-one data and the detector Monte Carlo simulation. The estimated

uncertainty of the simulation is less than 10%[22]. Therefore, the crack correction has an uncertainty of less than 0.1%, which is negligible for the e/π ratio study.

5.3 Load–two electron and pion energy scan results

With the load–two configuration, we have taken energy scan data with both electron and pion beams at two positions of the CC (Figure 4.7). I will show the results of these two energy scans. The results shown here include all the cuts and corrections described in Sections 5.1 and 5.2, in addition to a pedestal correction, using the pedestal data we collected during the beam spill. We discovered that there is a small difference between the pedestals we get for calibration pedestal data and the pedestal data taken during the beam spill (inspill pedestals). This is largely due to the narrow window size used to calculate the calibration pedestal. Using the inspill pedestals to correct this small difference, the small error of the calibration pedestal can be eliminated. The TRG measurement includes the non-linearity correction, the trigger tower gain correction, the sampling fraction correction, the EM/HD crosstalk correction and the CC crack correction.

The main purpose of this dissertation is the study of the e/π ratio difference. No effort is made to optimize the detector resolution for a certain type of particle. The cluster size is chosen to minimize the systematic uncertainty of the e/π ratio measurement. In this Chapter, I will show the detector response to both electron and pion beams, and I will summarize the e/π ratio difference measurements with all the uncertainties and corrections in the next Chapter.

5.3.1 The electron energy scan data

Figures 5.10 and 5.11 show electron energy scan linearity plots at (η=0.05, ϕ=31.6) and (η=0.45, ϕ=31.6), where (η, ϕ) is in D0 index unit (Section 4.5). They include the

energy measurements using both electron and pion clusters. The trigger data is normalized to fit in the same scale. The error includes the statistical errors of both energy measurements and the inspill pedestal correction. The linearity fits and residue plots show that the detector generally has a linear response for electrons, but there are a few points that need discussion.

The BLS data show little dependence on the cluster size. There is a small difference in the electron response at the two data points. It could be caused by the non-uniformity of the Uranium plates. It is known that the Uranium plate thickness variation is a few percent and this could account for the variation of the electron response. This variation has been studied with a large set of data specially taken for the uniformity study[28].

The TRG data show that there is a small difference between energy measurements with different cluster sizes, with the larger cluster (pion cluster) having higher response. This effect is due to the crosstalk between trigger towers. I have measured and corrected the crosstalk between the EM and HD channels in the same trigger tower, but there are similar crosstalk mechanisms between trigger towers. The coupling capacitance between trigger towers is smaller, so the crosstalk signal should be smaller. The results show that it is about 1%. Since I will use the same cluster size for both electron and pion energy measurements to calculate the e/π ratio, this effect should not affect the e/π ratio measurement.

There is a small offset in the linearity fits for both the BLS and TRG data. It is equivalent to less than 300 MeV for the BLS data and 430 MeV for the TRG data. This offset is due to the small non-linearity caused by the extra material in front of the detector. Because of the nonlinear energy dependence of the longitudinal electron shower distribution, the simple correction we made by changing the EM layer one sampling fraction to compensate for this extra material still leaves us this small offset.

However, because this offset is small, its effect on the e/π ratio measurement is negligible.

5.3.2 The pion energy scan data

The pion energy scan data is shown in Figures 5.12 and 5.13. The detector response for pions is generally linear. The pion linearity fits show that there are larger offsets (~ 1 GeV) for pions than for electrons. The major reason for this larger offset is due to the detector's nonlinear hadron response, especially at low energies (kinetic energy $E_k < 5$ GeV). Figures 6.5 and 6.6 show that the e/π ratio increases as energy decreases, and that this effect is more pronounced for low energy data ($E_k < 5$ GeV)[21]. If I assume the detector response to electrons to be linear, then the detector response to pions must have a nonlinear relation to the pion energy. The response varies between two data points. This variation is similar to the variation of the electron response. This is an indication of the detector's non-uniformity. I will include this as a systematic uncertainty for the e/π ratio measurement.

5.4 Load-one energy scan results

With the load-one configuration, we took a large amount of data in order to study the uniformity, linearity, etc. The results have been published in [22]. We did not take useful data with calorimeter trigger electronics for the energy scan study. Here I only show the published energy scan results with the BLS data in order to compare with the load-two results. A detailed discussion can be found in [22].

Energy scan data for both electrons and pions were taken. The data show good linear response for both electrons and pions. The linearity fit yields a result;

for electrons: $E(ADC) = 80.2 + 267.4P$,

for pions: $E(ADC) = -565 + 257.1P$,

where P is the beam momentum in GeV/c.

5.5 Load-one and load-two electron data comparison.

The load-one electron linearity fit shows that the load-one detector has a higher electron response than load-two. If I average over the two sets of the load-two electron energy scan data, I get the load-two electron response to be:

$$255.4(^{ADC}/_{GeV}).$$

Comparing this with the load-one electron response:

$$267.4(^{ADC}/_{GeV}),$$

the load-one electron response is about 4.5% higher than the load-two response. This is larger than any systematic uncertainty I can find.

There is evidence that this difference could be caused by a local hardening effect[15]. In its simple form, the local hardening effect is the following process (referring to Section 2.4.1 for the calorimeter response to the EM showers). In the electromagnetic shower development, a large fraction of the energy goes into the production of low energy photons. For low energy photons (below 1 MeV), the photo-electric effect is the dominant interaction, and the cross section of the photo-electric effect is proportional to Z^5 of the material. As a consequence, the soft photons from the electron showers interact almost exclusively in the absorber, and most of the soft photons will transfer their energy to knock out electrons in the absorber. These electrons have very low energy (~ 10s of keV), and very short range. A fraction of the photo-electric

interactions are sufficiently close to the surface for the electrons to escape, so these electrons contribute to the measured signal. However, if some low Z material (inactive) covers the surface of the high Z absorber, these electrons would not be able to reach the detecting media, and thus would not contribute to the measured signal.

In the D0 CCEM module, about half of the Uranium plates in the EM layers 1, 2 and 3 have one surface covered with readout boards (made of 3.6mm G10 plate). On the average, over 75% of the electron energy is deposited in these three layers. Therefore, I expect that the electron energy response will be suppressed. In the ECEM calorimeter, there is no readout board covering the Uranium surface, so I would expect the load-one module (ECEM) to have higher electron response than the load-two module (CCEM). There are only a total of three readout boards in the CCFH module (with 50 Uranium plates), so I do not expect any significant effect on the pion energy measurement caused by the readout boards.

The local hardening effect has been measured by the SICAPO collaboration[15] with the U/G10/Si sampling calorimeter. From their measurement, and if I assume that liquid Argon readout is similar to Si readout for detecting these photo-electrons, I expect about 19% signal suppression of an electron shower with one surface of every Uranium plate covered with 5mm G10 plates. If I assume that 3.6mm G10 plate is about 50% to 100% as effective as the 5mm G10 plate used in the SICAPO calorimeter, then I can estimate that the suppression of the electron signal will be 3.6% to 7.1%. This rough estimate agrees with the load-one and load-two electron energy scan data.

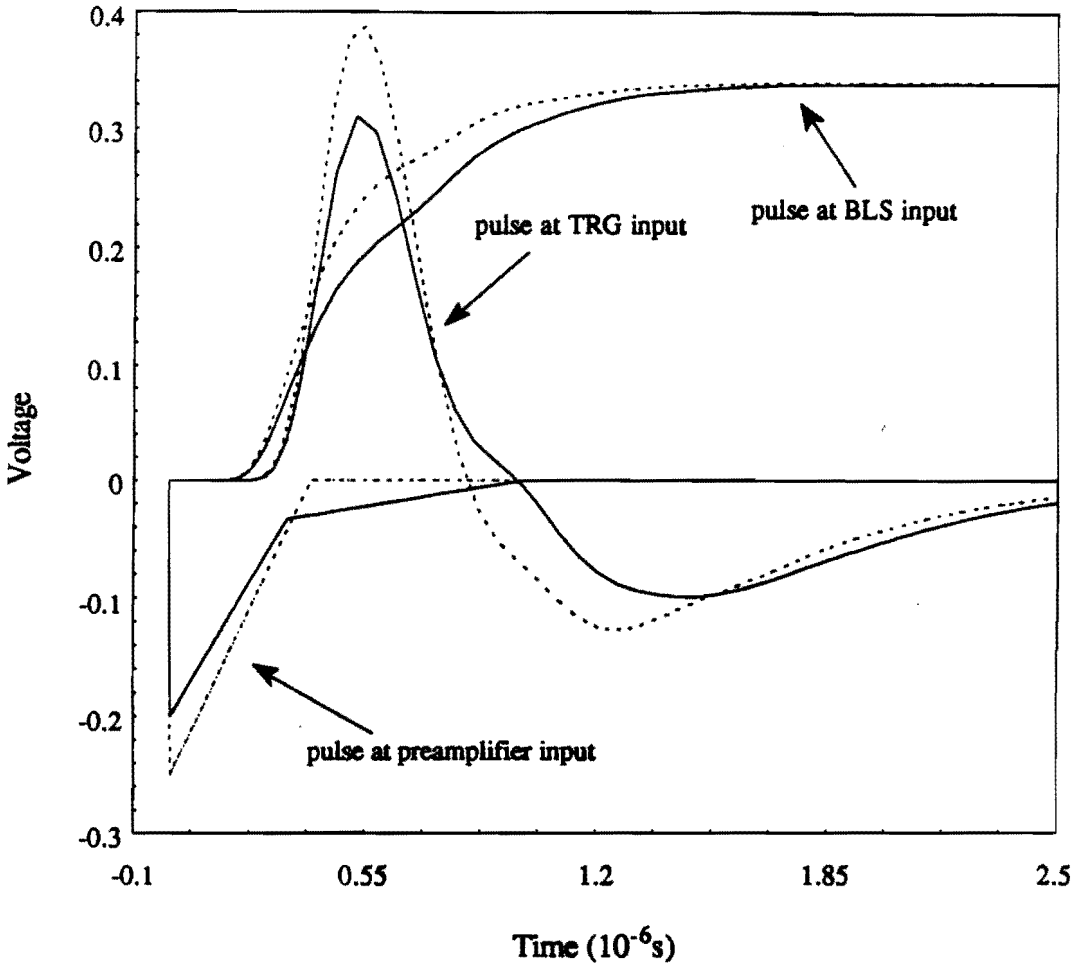

Figure 5.0 SPICE simulation of TRG readout and precision readout (BLS) responses to fast and slow showers

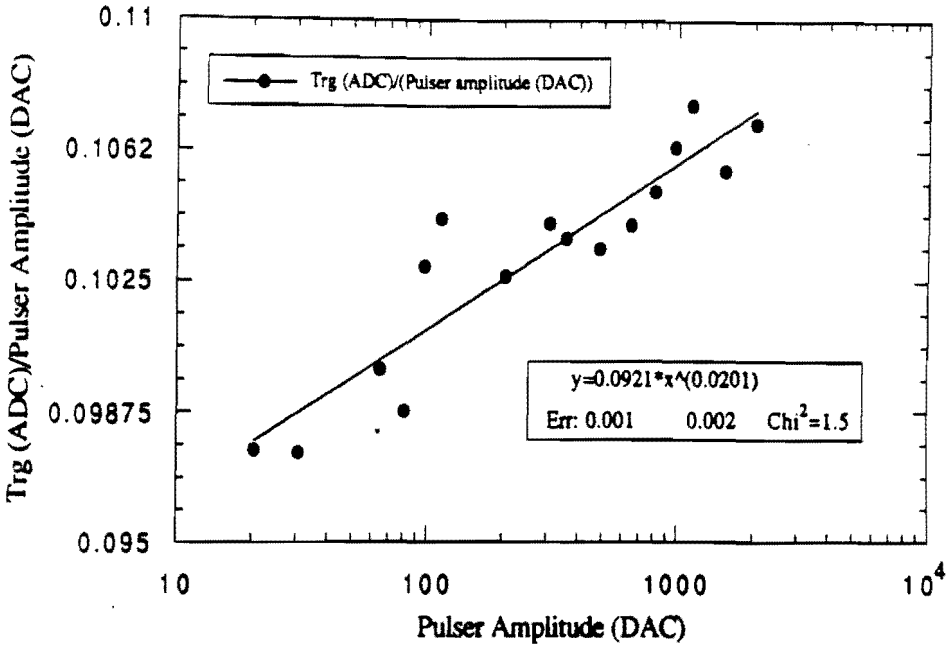

Figure 5.1a NWA trigger driver linearity study using calibration pulser

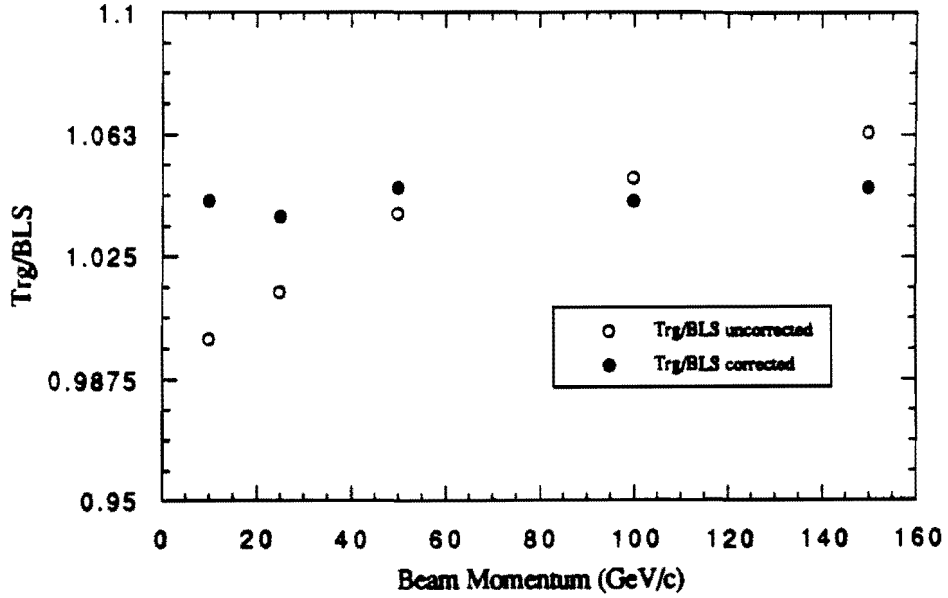

Figure 5.1b Electron energy scan, Trg/BLS with & without linearity correction

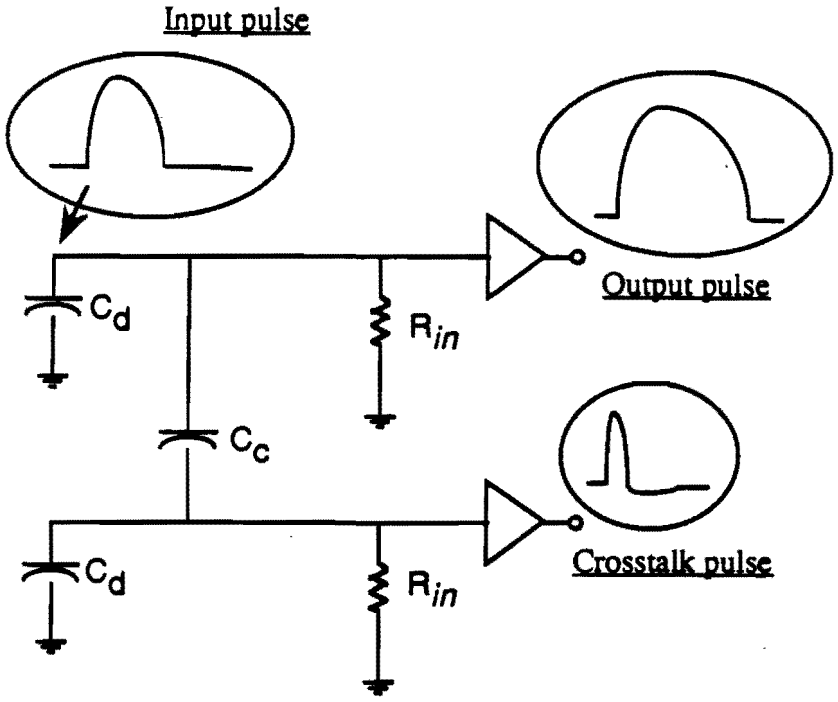

Figure 5.2 Calorimeter electronics crosstalk schematics

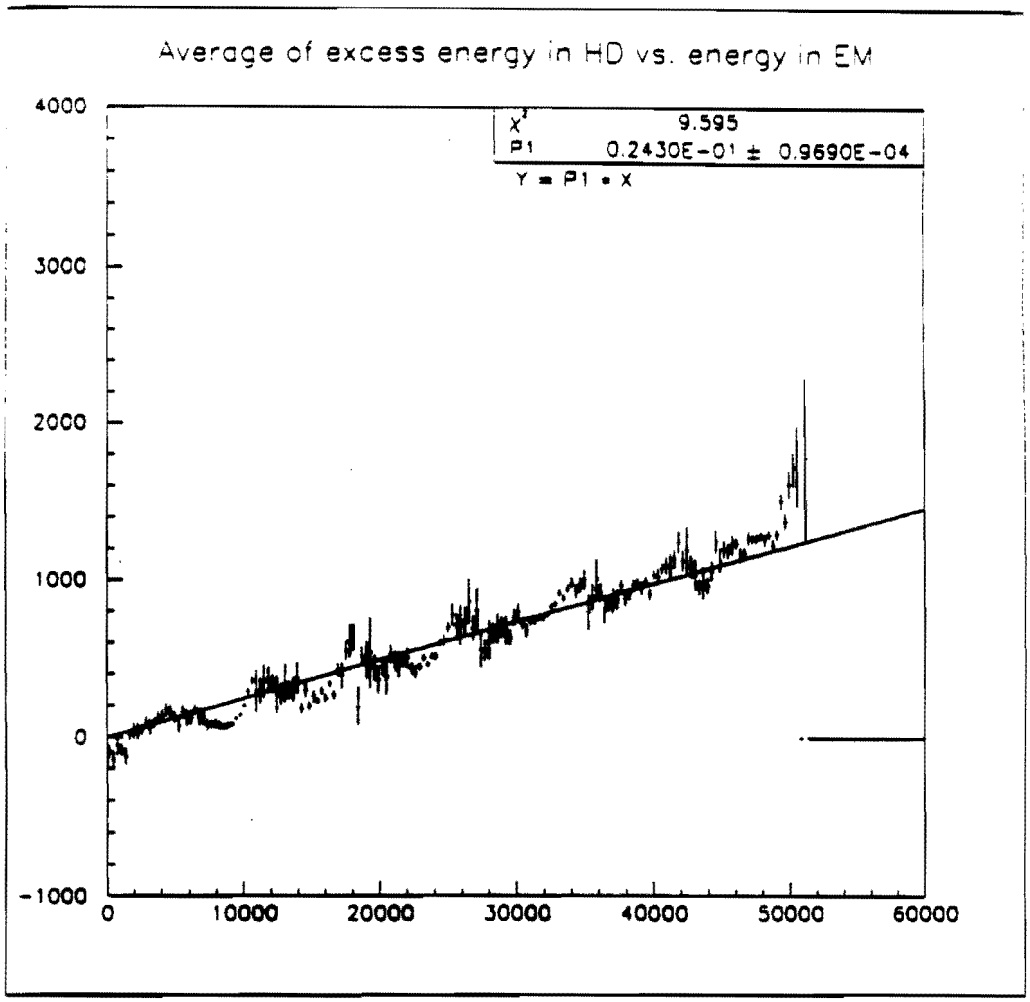

Figure 5.3 **The excess energy in the level-one calorimeter trigger HD channel vs. energy in the EM channel.**

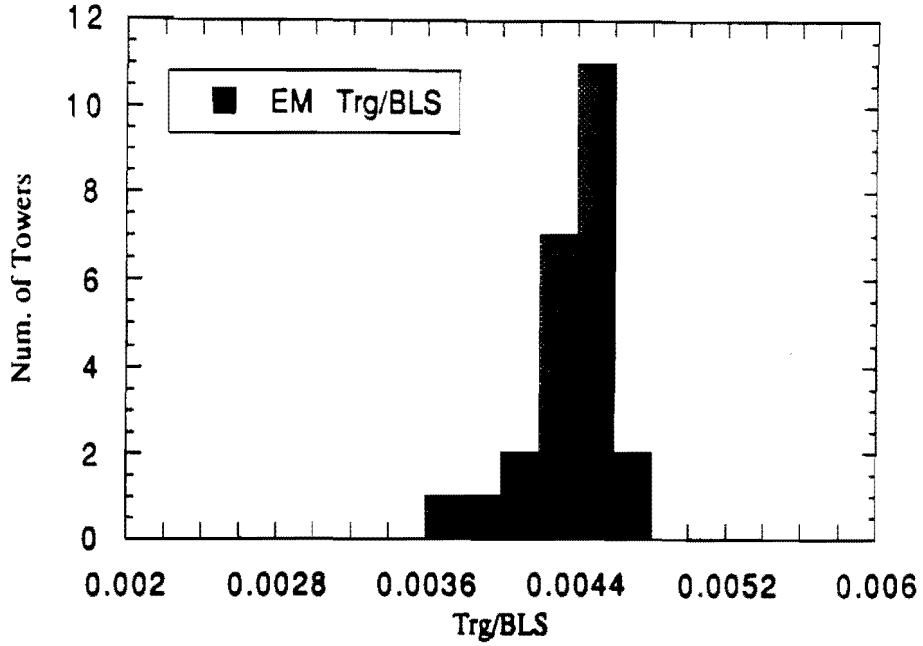

Figure 5.4a Electron trigger tower scan, EM trigger tower gain distribution

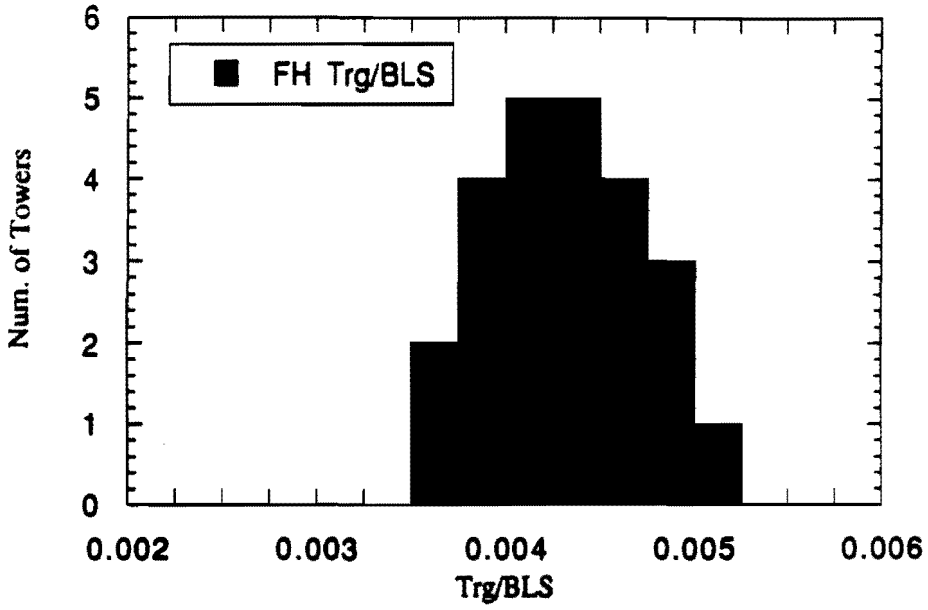

Figure 5.4b Electron trigger tower scan, FH trigger tower gain distribution

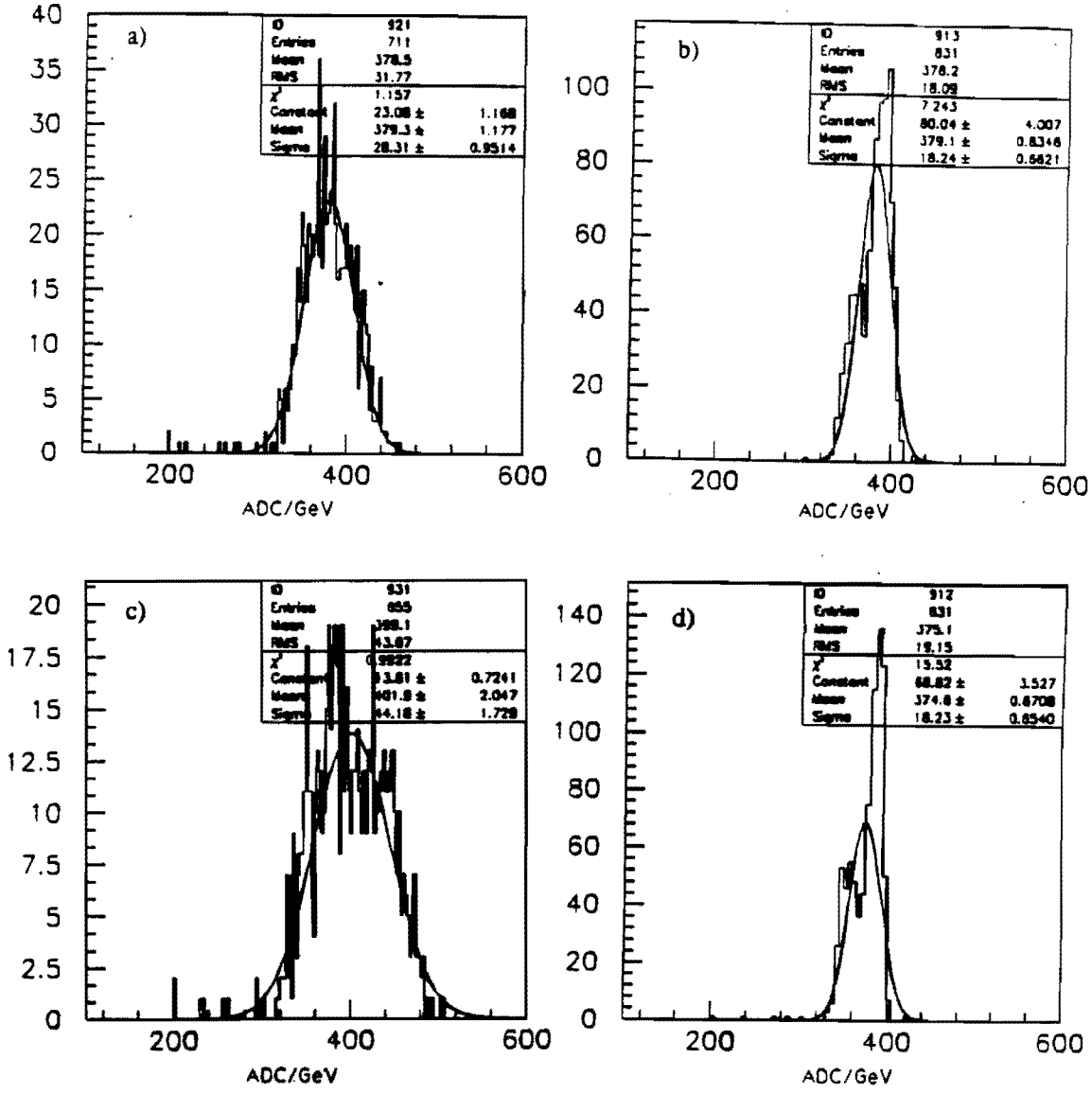

Figure 5.5 The energy distributions with different gain smearing. a) 100 GeV pion with 10% gain smearing, b) 100 GeV electron with 10% gain smearing, c) 100 GeV pion with 20% gain smearing, d) 100 GeV electron with 20% gain smearing.

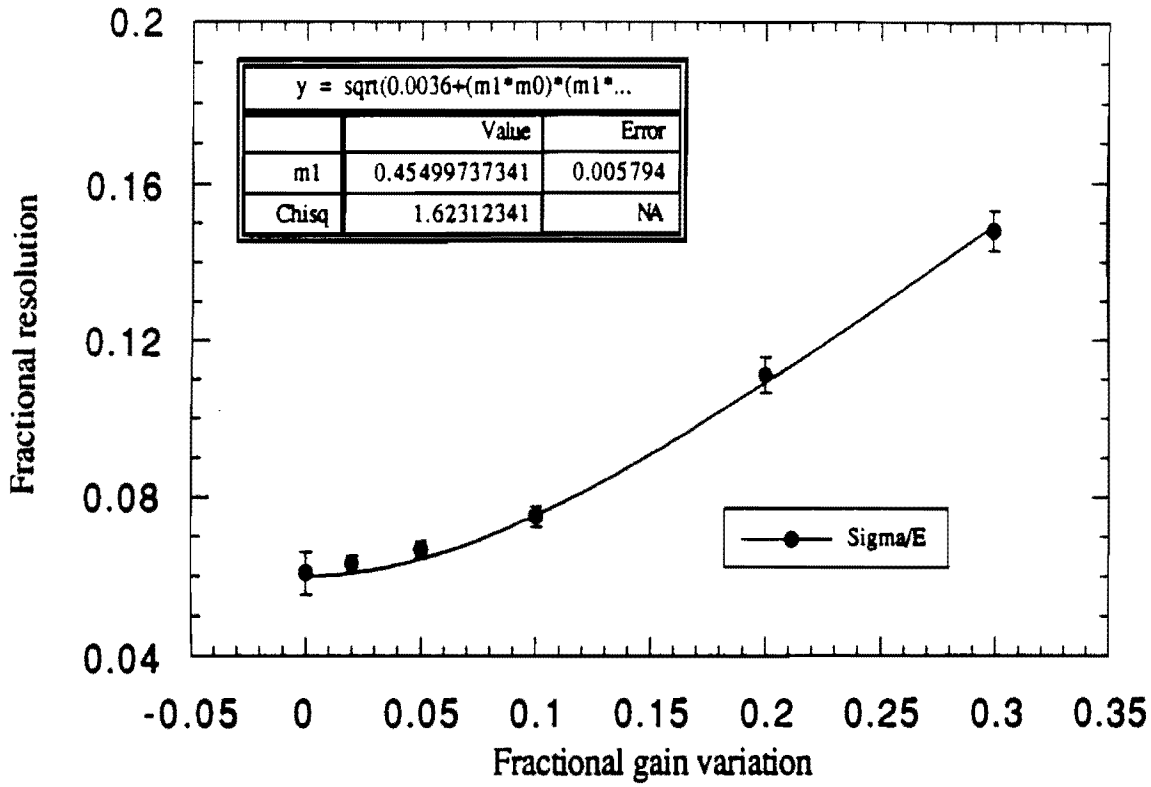

Figure 5.6 Trigger gain variation study with 100 GeV pions.

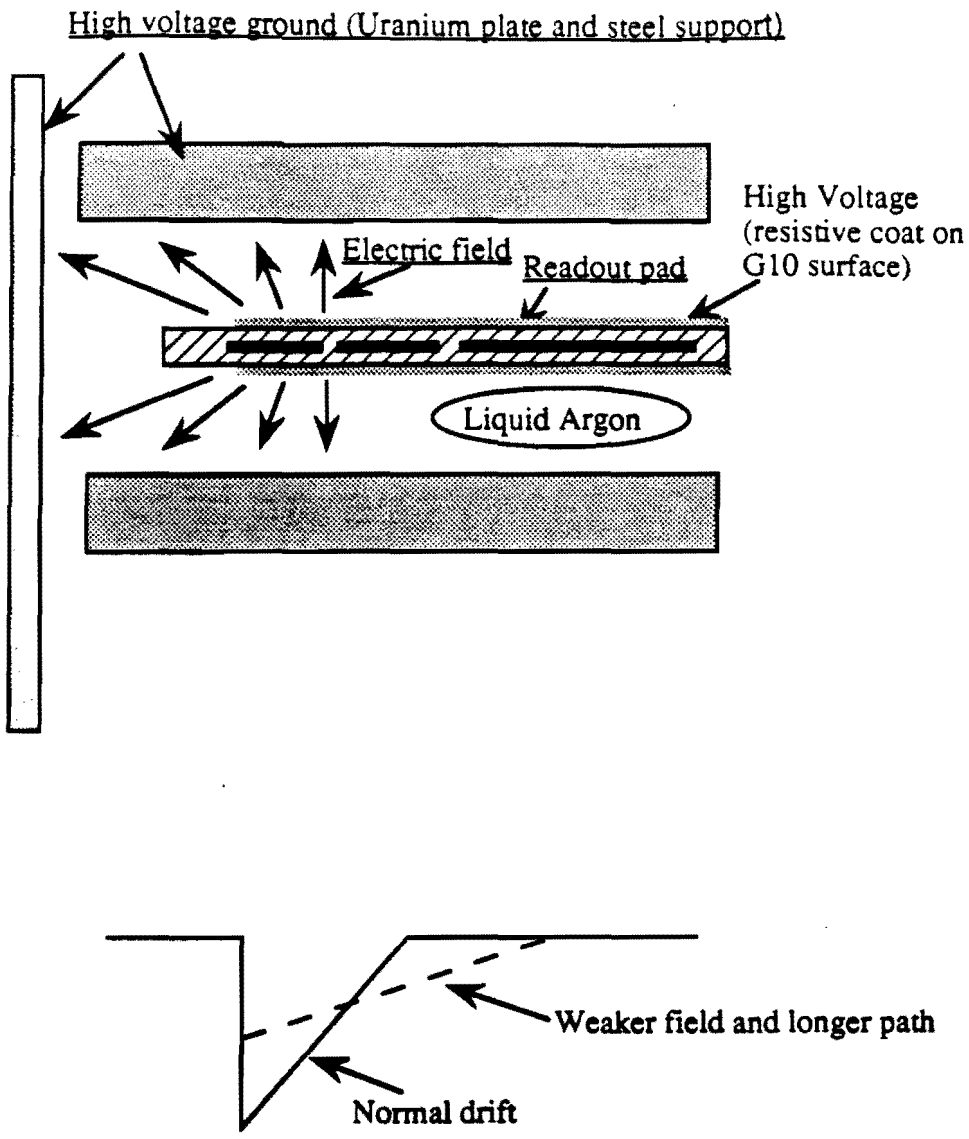

Figure 5.7 Electric field at CCEM crack and charge pulse shape

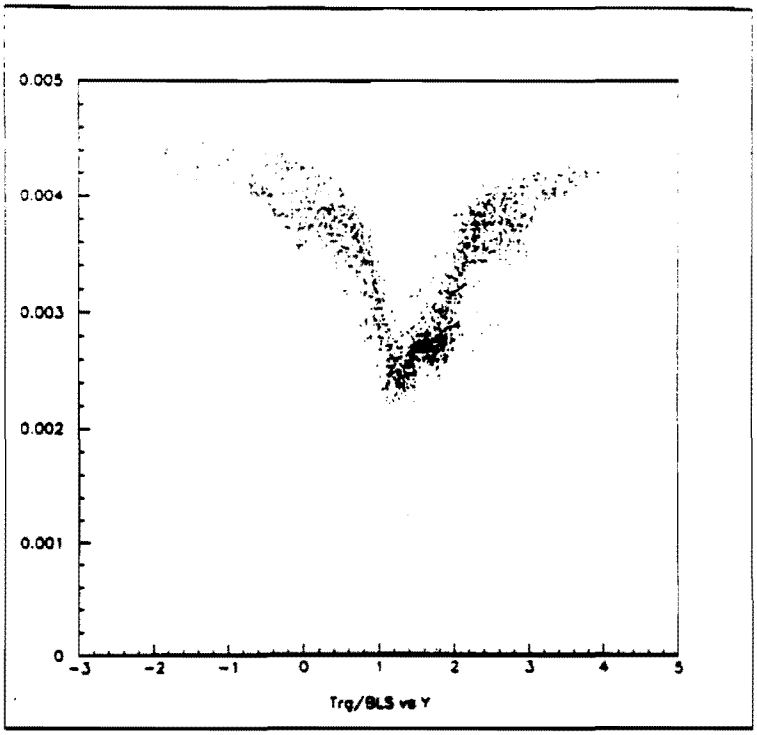

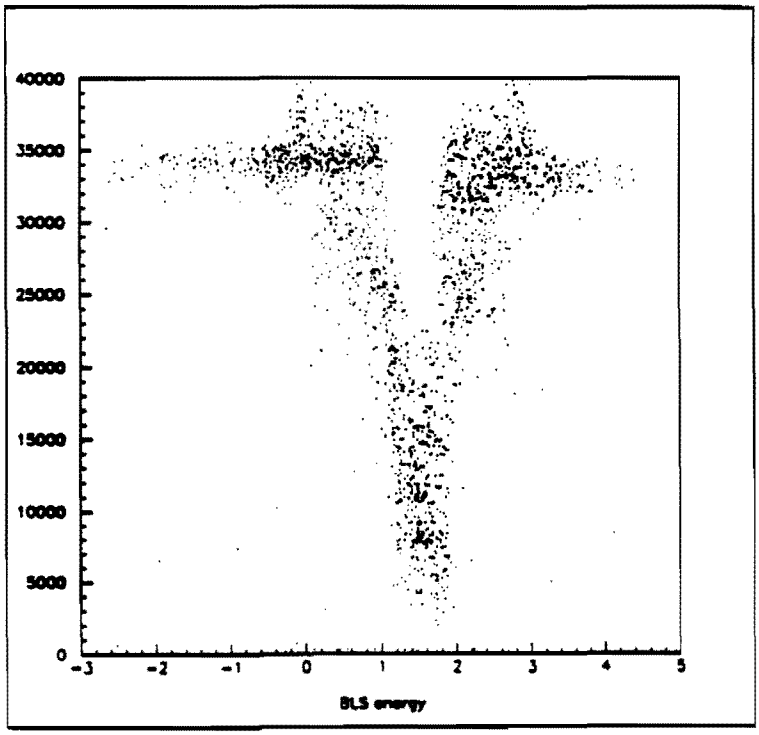

Figure 5.8 a) Ratio of the TRG and BLS vs. the vertical position (cm) of the 50 GeV electron beam.
b) Energy response of the BLS vs. the vertical position (cm) of the 50 GeV electron beam.

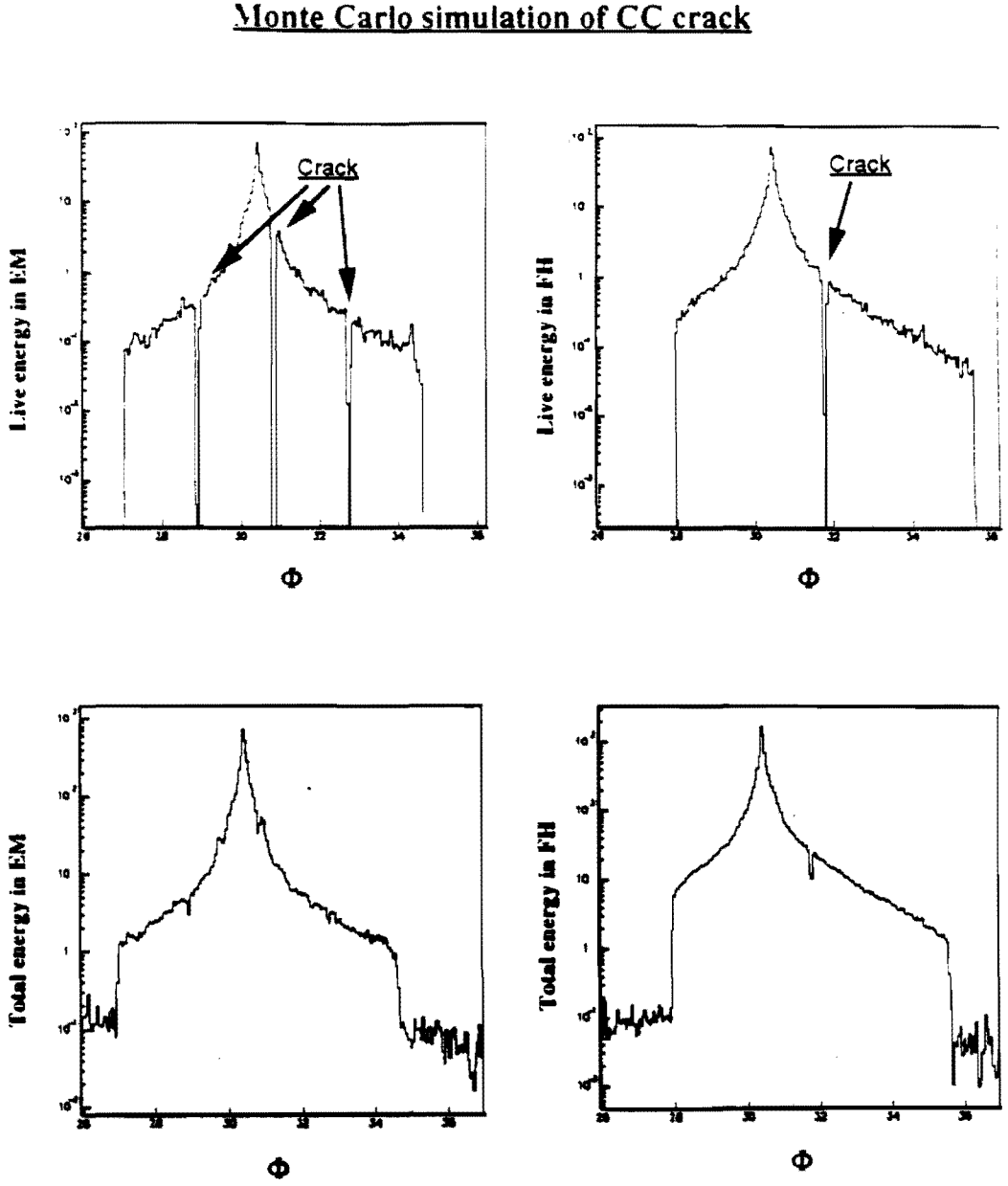

Figure 5.9 Monte Carlo simulation of the energy distribution of the 50 GeV pion showers in the D0 central calorimeter.

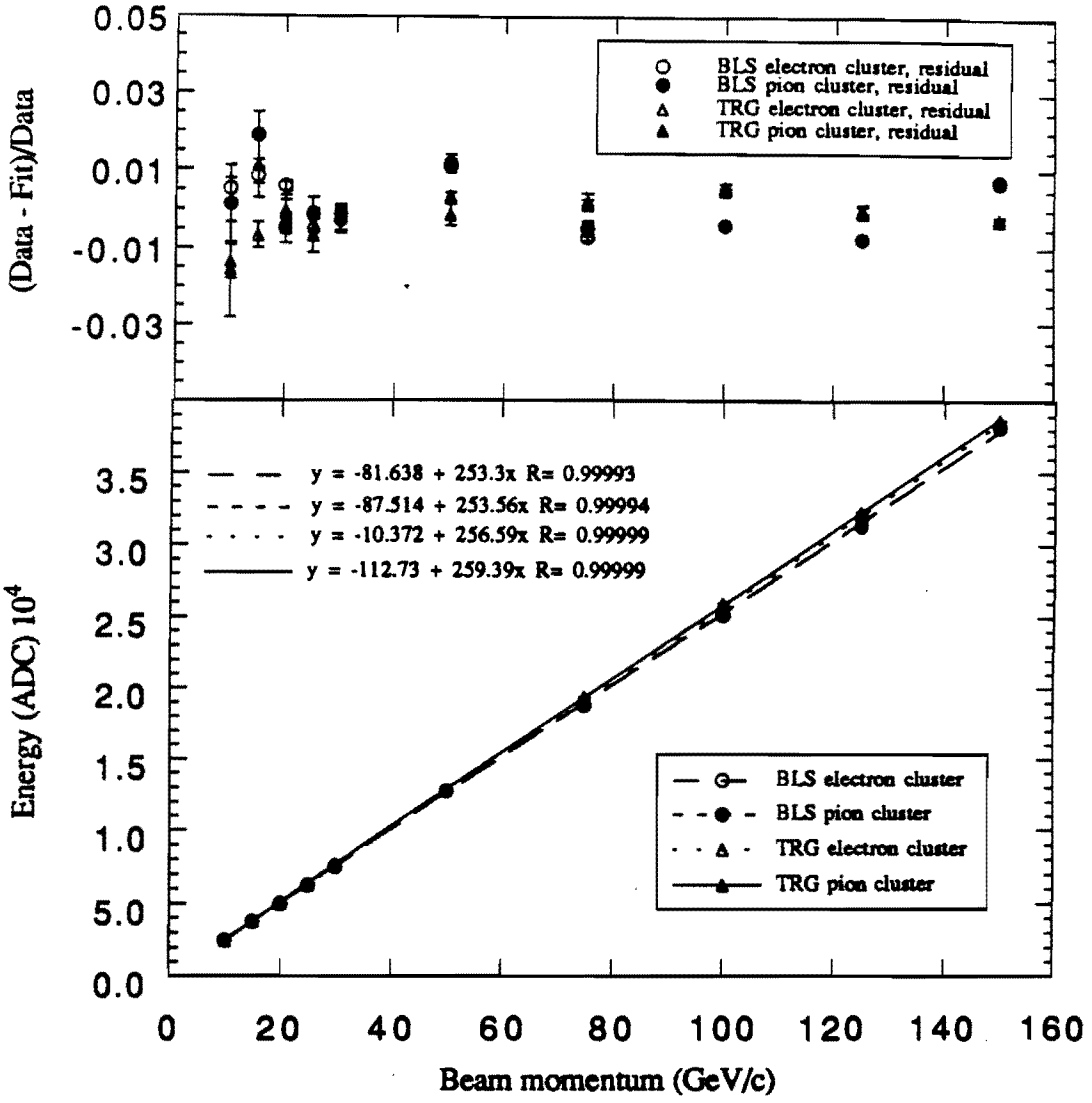

Figure 5.10 Electron energy scan, eta=0.05, phi=31.6

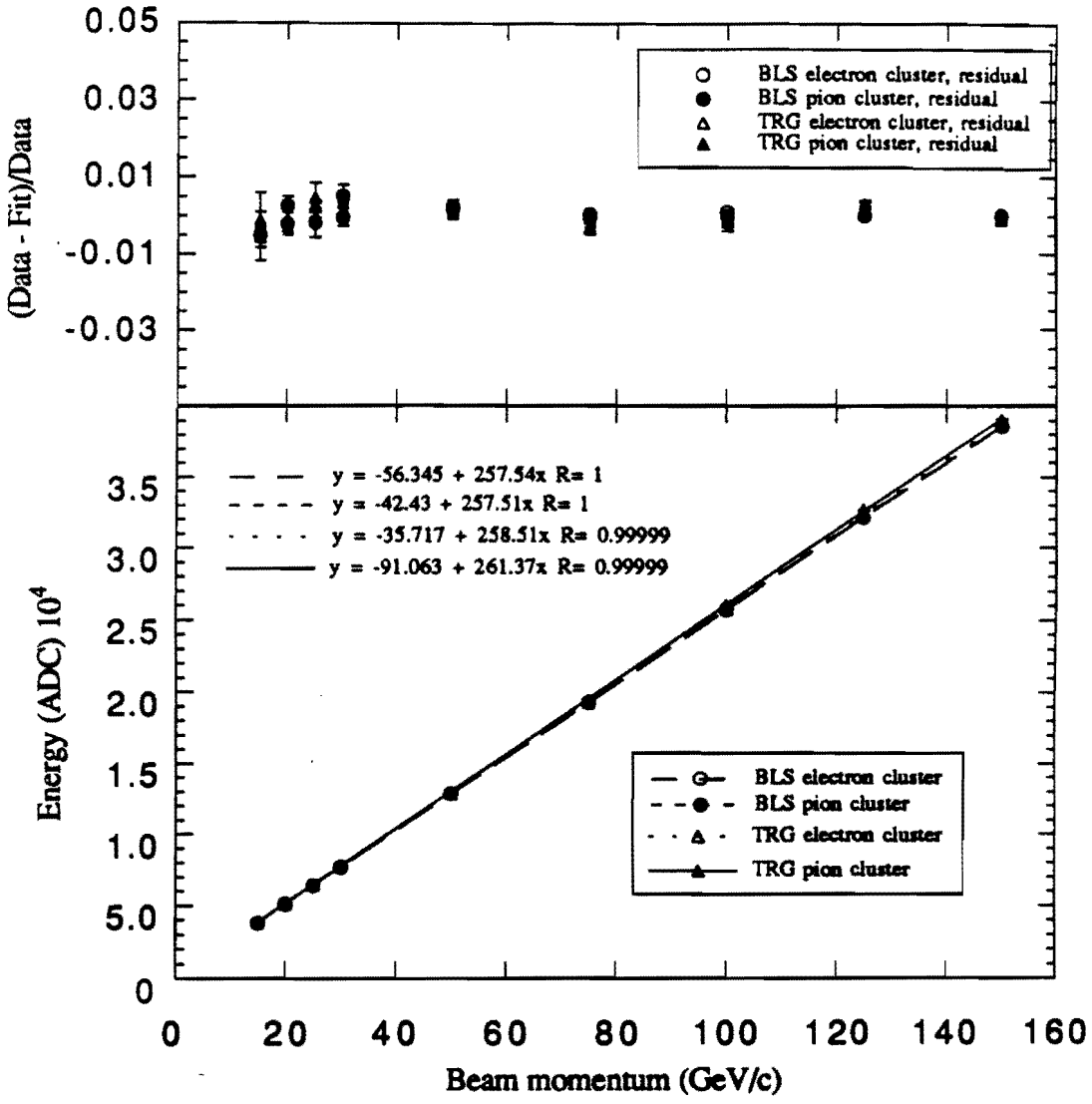

Figure 5.11 Electron energy scan, eta=0.45, phi=31.6

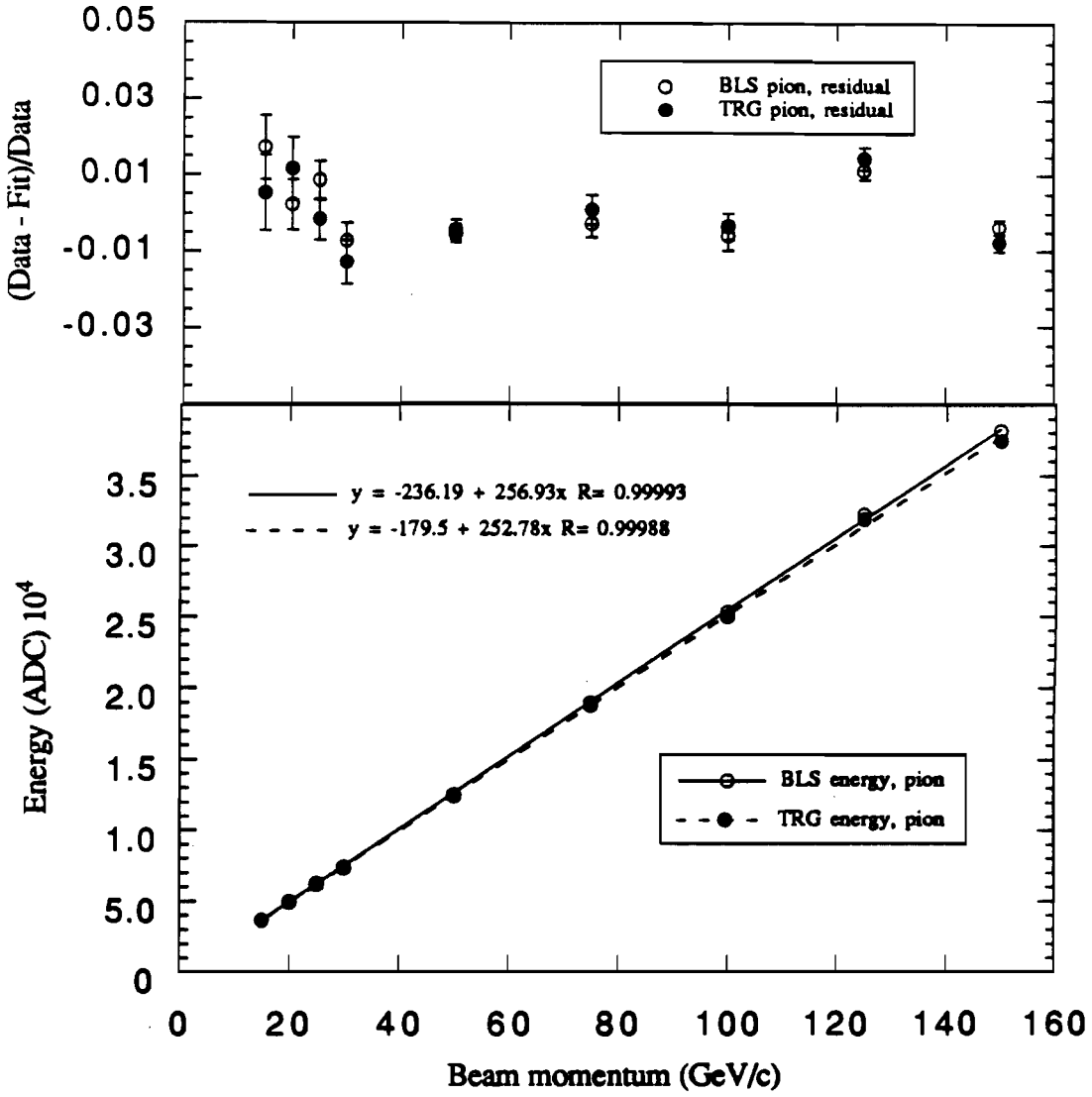

Figure 5.12 Pion energy scan, eta=0.05, phi=31.6

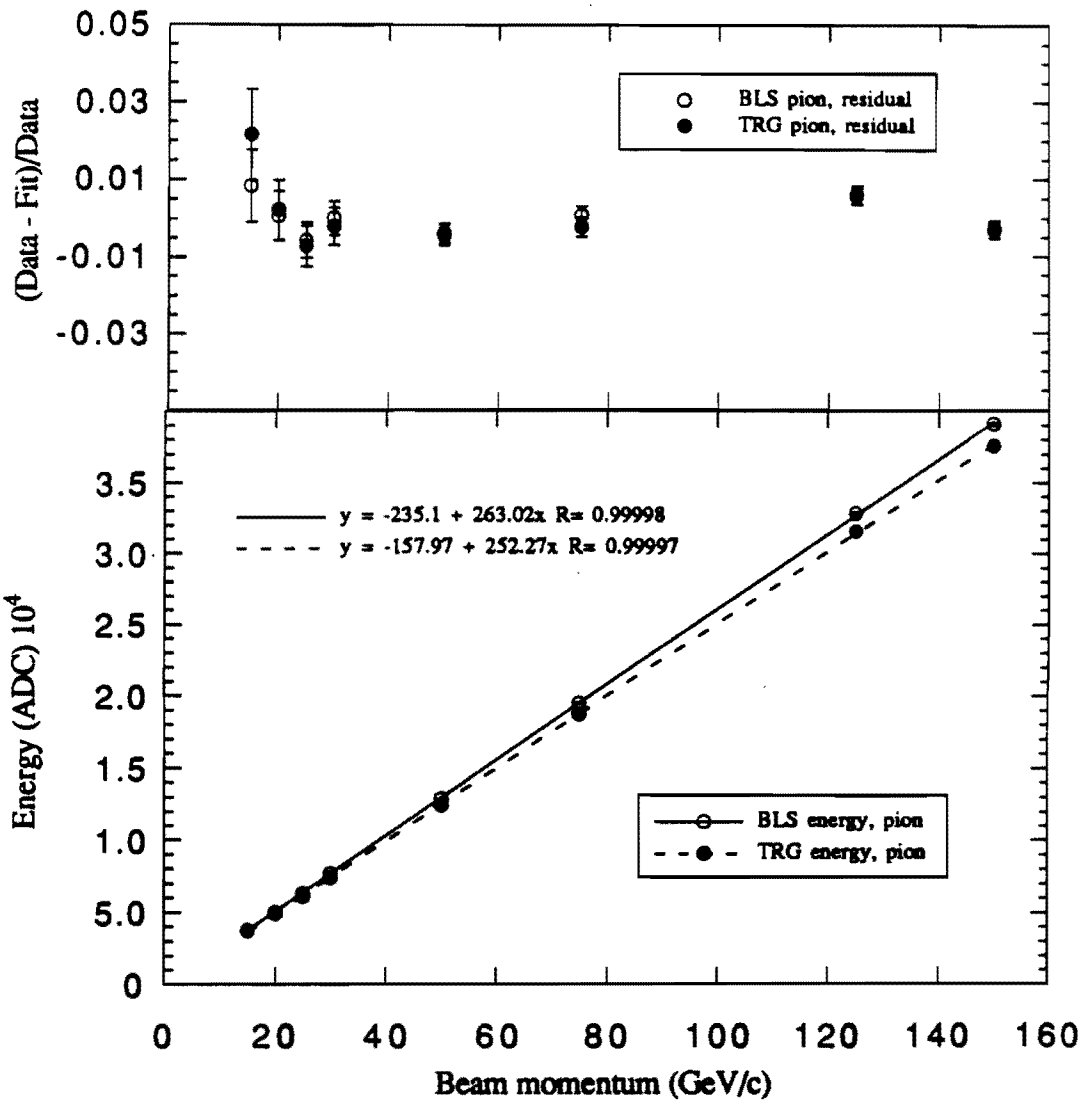

Figure 5.13 Pion energy scan, eta=0.45, phi=31.6

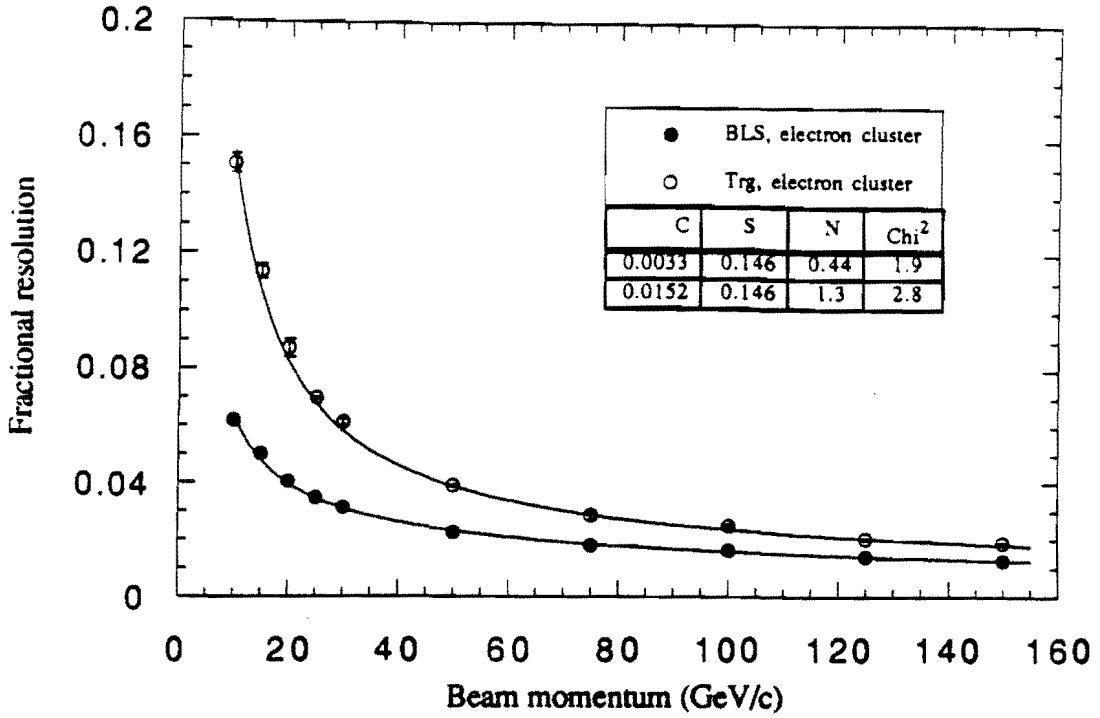

Figure 5.14a Electron energy resolution, eta=0.05, phi=31.6

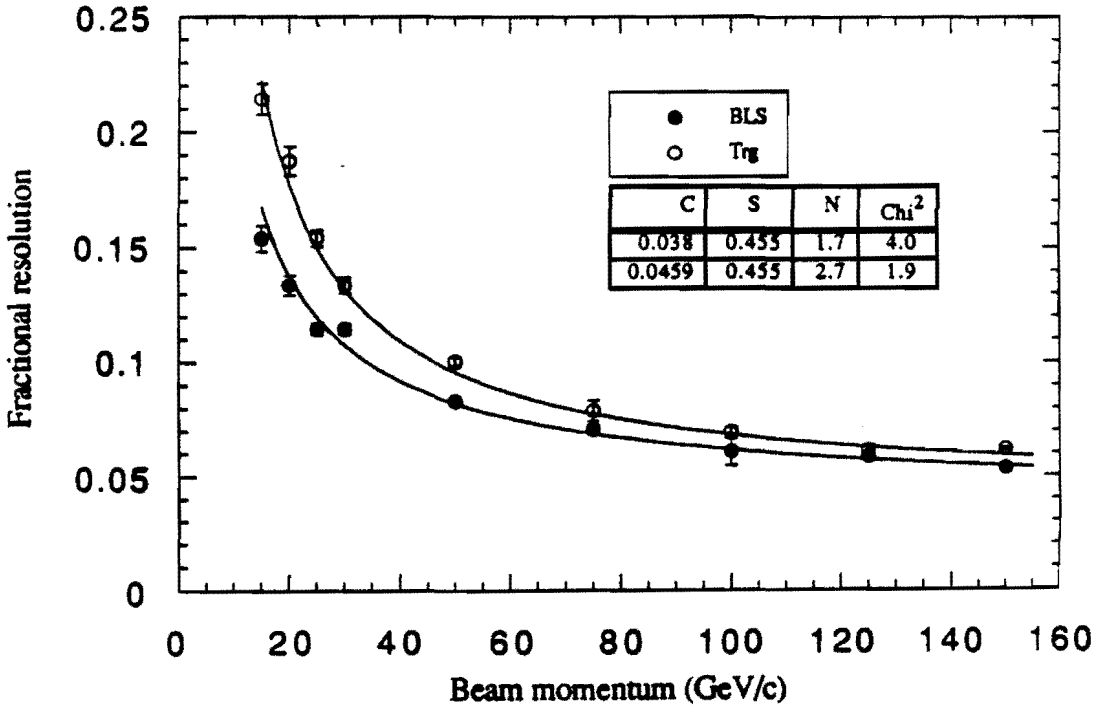

Figure 5,14b Pion energy resolution, eta=0.05, phi=31.6

Chapter 6
Results and Monte Carlo simulation.

The final analysis of the load-two e/π ratio measurement with both fast trigger (TRG) and precision (BLS) readouts will be presented in this Chapter. To understand the detector response to good precision, we have to understand the small effects caused by the imperfections of the detector. In Section 5.2.5, an example was given on using the Monte Carlo simulation to study the detector crack effect. In this Chapter, I will present the detector Monte Carlo simulation and the comparison with test beam data. Another example will be given on using the Monte Carlo simulation to study the pion shower leakage in the load-two test beam configuration. Finally, there will be a discussion of the results and the questions that need to be studied further. Conclusions will be presented.

6.1 General information about the GEANT Monte Carlo simulation

GEANT V3.14[3] is an integrated Monte Carlo package supported by CERN. It is designed to help simulate the behavior of large complex particle detector systems like the D0 detector. It includes a geometry package, a memory handling package, and a physics interaction simulation package. The physics processes package includes EGS4[23] for the electromagnetic shower simulation, and GHEISHA[24] and NUCRIN[25] for the hadronic shower simulation. All the primary and secondary particles are transported through the detector geometry until their energies fall below some kinematics cut or they move out of the detector.

The D0 experiment uses GEANT V3.14 as a framework for its detector simulation. The simulation includes all the detector subsystems, and it is done with geometric detail as close to reality as possible. For example, the calorimeter simulation is done with geometric detail to the individual absorber and readout plate level. Such a detailed simulation enables us to simulate many geometric features of the detector, e.g. the inter-module cracks. There have been many tests[22,17] to verify the detector simulation with test beam data, and large progress has been made to tune the Monte Carlo simulation to match the test beam results.

A special test beam version of the calorimeter Monte Carlo program was written to include all the test beam geometric information, including all beam line materials and cryogenic materials. The load-two test beam geometry is shown in Figure 6.0a. The following comparison of the test beam data and Monte Carlo simulation is done with this test beam version Monte Carlo simulation. The hadronic shower simulation uses GHEISHA, and the kinematics cuts of all the particles are set to a minimum of 10 keV for maximum accuracy.

6.1.1 Monte Carlo simulation of electron and pion energy scan

A set of Monte Carlo energy scan data has been generated for both electrons and pions with different energies, at (η=0.05, ϕ=31.6) which is the bench mark position of the load-two test beam. The Monte Carlo data are analyzed the same way as the beam data. Figure 6.1 shows the linearity of the Monte Carlo data. In this figure, the Monte Carlo data are normalized to approximately the same scale as the beam data. Comparing with Figures 5.10 and 5.12, the Monte Carlo data show similar linearity behavior as the beam data. For example, both the Monte Carlo data and the beam data show good linearity for electrons and pions, and the offset for the electron fit is smaller than the offset for the pion fit. However, there is a discrepancy between the Monte Carlo and

beam data on the relative response of electrons and pions. I will discuss this in Section 6.4.

One of the important requirements for the Monte Carlo simulation is the ability to simulate the random fluctuation of the electron and pion showers. To test this, I will compare the energy resolution of the Monte Carlo simulation with test beam data for both electron and pion energy scans. Figure 6.2 shows the energy resolution plot of both electron and pion energy scans. Since the Monte Carlo simulation does not include any external noise, the energy resolution from the Monte Carlo data is better than the energy resolution of the test beam data (Figure 6.2a). This effect is more visible at the low energy points where the noise dominates the energy resolution. To include the noise effect, I add the average noise measured from test beam pedestal data (Table 5.2) to the Monte Carlo data. It shows that the energy resolution of the Monte Carlo data with noise added is very close to that of the beam data (Figure 6.2b).

6.1.2 Monte Carlo simulation of pion shower leakage

In order to measure the e/π ratio accurately, a precision measurement of the pion energy is required. Because of the limited size of the test beam calorimeter, the pion showers are expected to leak a small percentage of their energy outside the detector. In the load–two configuration, the CC modules have only 7 interaction lengths and the transverse size is limited as well. Both longitudinal and transverse energy leakage of the pion showers needs to be studied. Based on the test beam Monte Carlo geometry, two more FH modules were added on the sides of existing FH modules and a large piece of Uranium was added at the back (Figure 6.0b). The leakage energy can be collected in these extra modules. The fractional pion energy leakage is listed in Table 6.1. The fractional energy leakage is defined as:

$$f_{leakage} = \frac{\left(\overline{E}_{total} - \overline{E}_{Stand}\right)}{\overline{E}_{Stand}}$$

where the $\overline{E}_{total}$ is the average total energy (energy in the test beam modules + energy in the extra modules), and $\overline{E}_{Stand}$ is the average standard energy (energy in the test beam modules only). The uncertainty in the table is 10% of the leakage energy. The 10% is the estimated precision of the Monte Carlo pion shower simulation, deduced by comparing the pion transverse shower shape of the load-one data with the Monte Carlo simulation[22].

Beam energy (GeV)	Load–two fractional[1] energy leakage(%)	Fractional[2] uncertainty of the leakage (%)
15	2.39	0.24
25	2.39	0.24
50	2.85	0.29
75	3.00	0.30
100	2.74	0.27
125	2.64	0.26
150	2.82	0.28

Table 6.1

6.2 Summarized results of the load-two e/π ratio difference at different integration times.

To determine the e/π ratio difference between short (TRG) and long (BLS) integration times, I subtract the BLS e/π ratio from the TRG e/π ratio. This way, many systematic uncertainties in the energy measurement (pion shower leakage, non-uniformity, etc.) are

[1] Fraction of total energy in the detector.
[2] The error of the energy leakage divided by the total energy in the detector.

canceled. The remaining systematic uncertainty is dominated by the uncertainty in the trigger electronics' gain. Figure 6.3a shows the e/π ratio difference between the TRG and BLS. All the relevant corrections for the electron and pion energy measurements have been applied in the calculation of the e/π ratios. Table 6.2 is a list of all the statistical and systematic uncertainties (in fractional percentage units) caused by the various sources. The total uncertainty is the sum of all the uncertainties in quadrature. I will briefly discuss each of the terms below.

Beam Momentum (GeV/C)	15	20	25	30	50	75	100	125	150
Trigger Drv. non-linearity	0.46	0.46	0.46	0.46	0.46	0.46	0.46	0.46	0.46
TRG sampling fraction	0.5	0.5	0.5	0.5	0.5	0.5	0.5	0.5	0.5
Trigger cross-talk	0.65	0.65	0.65	0.65	0.65	0.65	0.65	0.65	0.65
Trigger gain variation	3.0	3.0	3.0	3.0	3.0	3.0	3.0	3.0	3.0
CCEM crack effect	0	0	0	0	0	0	0	0	0
Pion shower leakage	0	0	0	0	0	0	0	0	0
Statistical uncertainty	1.3	0.8	0.6	0.5	0.3	0.3	0.3	0.3	0.2
Trigger FADC uncertainty	2.01	1.52	1.22	1.01	0.60	0.40	0.30	0.24	0.20
Total uncertainty of $\left(\frac{e}{\pi}\right)_{TRG} - \left(\frac{e}{\pi}\right)_{BLS}$	4.0	3.6	3.3	3.3	3.2	3.2	3.2	3.2	3.1

Table 6.2

(1). Trigger non-linearity correction: This is a small correction. The 10% uncertainty on the correction exponent affects the e/π ratio measurement by 0.46%[Section 5.2.1].

(2). Sampling fraction correction: The difference between the sampling fraction used to calculate trigger resistors and the precision sampling fraction is less than 10%,

and the energy difference between the TRG and BLS is less than 5%, therefore, I estimate the uncertainty of the sampling fraction correction to be 0.5%[Section 5.2.2].

(3). Trigger crosstalk correction: Since the crosstalk correction is small, the uncertainty of the crosstalk comes mostly from the uncertainty in the crosstalk mechanism. I use the difference of the two mechanisms as the uncertainty in the correction. This difference is 0.6% for the EM and 0.65% for the HD energy measurement. Since it is a systematic uncertainty I will use the larger one (HD channel's) for the e/π uncertainty estimate[Section. 5.2.3].

(4). Trigger gain variation: This is the largest systematic uncertainty for the TRG energy measurement. From resolution studies, I estimate the worst case gain variation as 2.4% for the EM, and 5.8% for the HD channels. Because the electron and pion showers are deposited in many preamplifier channels, this gain variation only affects the average TRG energy measurement by 1.5% for the EM and 2.6% for the HD[Section. 5.2.4]. I combine both uncertainties in quadrature and get that the total uncertainty of the e/π ratio caused by the trigger gain variation is 3.0%.

(5). CCEM crack effect: Because the crack effect correction is very small (less than 1%), the uncertainty of the correction is negligible[Section. 5.2.5].

(6). Pion shower leakage: Because both the TRG and BLS share the same leakage correction, it does not introduce any uncertainty in the difference between the TRG and BLS e/π ratio measurement.

(7). Trigger FADC digitizing uncertainty: The FADC used in the calorimeter trigger has a maximum uncertainty of $\pm$ 0.5 ADC counts on the digitized output data. I use the worst case of 0.5 ADC count as the systematic uncertainty contributed from FADC digitization.

In Table 6.2, the total uncertainty of $\left(\frac{e}{\pi}\right)_{Trg} - \left(\frac{e}{\pi}\right)_{BLS}$ is the uncertainty of the individual measurements. There are two sets of independent measurements of the e/π ratio difference at two different detector points (η=0.05 and η=0.45). Since these two sets of data are measured with different trigger electronics channels and FADC digitizers, by combining these two sets of data one can get a better uncertainty estimate. To calculate the combined uncertainty of two individual measurements, one has to separate the common uncertainties and independent uncertainties in the two measurements. In our case, the uncertainties caused by trigger driver non-linearity, trigger sampling fraction and trigger crosstalk are common uncertainties. They are correlated in the two measurements, so combining the two measurements will not improve these uncertainties. However, the uncertainties caused by the trigger gain variation, statistics and the trigger FADC are independent uncertainties. These uncertainties are not correlated in the two measurements. Combining the two measurements, I can improve these uncertainties.

Beam Momentum (GeV/C)	15	20	25	30	50	75	100	125	150
Average $\left(\frac{e}{\pi}\right)_{Trg} - \left(\frac{e}{\pi}\right)_{BLS}$	0.027	0.033	0.047	0.045	0.041	0.052	0.057	0.055	0.049
Combined uncertainty $\left(\frac{e}{\pi}\right)_{Trg} - \left(\frac{e}{\pi}\right)_{BLS}$	0.028	0.026	0.025	0.024	0.024	0.023	0.023	0.023	0.023

Table 6.3

Table 6.3 is a list of the averages and uncertainty of the e/π ratio difference by combining the two sets of data. Since the uncertainties for the two independent measurements are the same, the combined result is the average of the two different results. The combined uncertainty is calculated as:

$$\sigma_{Comb} = \sqrt{\sigma^2_{TrgDrv} + \sigma^2_{TrgSmp} + \sigma^2_{TrgCross} + \frac{\sigma^2_{TrgGain} + \sigma^2_{Stat} + \sigma^2_{TrgFADC}}{2}}.$$

In this formula, σ_{Comb} is the total combined uncertainty. σ_{TrgDrv}, σ_{TrgSmp} and $\sigma_{TrgCross}$ are the uncertainties cause by trigger driver non-linearity, trigger sampling fraction and trigger crosstalk. $\sigma_{TrgGain}$, σ_{Stat} and $\sigma_{TrgFADC}$ are the uncertainties caused by the trigger gain variation, statistics and the trigger FADC. Since these uncertainties are not correlated in the two measurements, the contributions of the $\sigma_{TrgGain}$, σ_{Stat}, and $\sigma_{TrgFADC}$ to the combined uncertainty are a factor of $\sqrt{2}$ smaller than they are in each individual measurement. Figure 6.3b is the combined results (Table 6.3) of the two measurements. The results show that there is about a 5% difference in the e/π ratio between the short (TRG) and long (BLS) integration times with particle energy greater than 25 GeV. At lower energy, the systematic uncertainty increases and the difference appears to be less significant.

6.3 Precision readout (BLS) e/π ratio result

The load-two e/π ratio measurements from the precision readout (BLS) system are listed in Table 6.4. The result includes Monte Carlo estimated pion shower leakage. The uncertainty includes statistical uncertainty, pion leakage correction uncertainty and the uncertainty caused by the detector non-uniformity. The fractional energy uncertainty caused by the non-uniformity of the detector is estimated to be 1.6% by analyzing the uniformity scan data[28]. This analysis has not been completed, and the 1.6% uncertainty is a preliminary result. Since the uncertainty caused by the detector non-uniformity is the dominant uncertainty, its effect on the e/π ratio is preliminary too. Figure 6.4 shows the load-two e/π ratio results with two sets of energy scan data The Monte Carlo result in the figure comes from the data generated at (η=0.05, ϕ=31.6).

The Monte Carlo simulation and test beam data have a relative offset that will be discussed in the next Section.

Beam Momentum (GeV/c)	15	20	25	30	50	75	100	125	150
e/π ratio at η=0.05	1.036	1.016	1.007	1.018	1.022	1.000	1.001	0.980	1.008
uncertainty at η=0.05	0.021	0.019	0.018	0.018	0.017	0.017	0.017	0.017	0.017
e/π ratio at η=0.45	1.023	1.021	1.020	1.016	1.007	0.994	1.000	0.986	0.994
uncertainty at η=0.45	0.020	0.018	0.018	0.017	0.017	0.017	0.016	0.017	0.017

Table 6.4

The published result from the load-one data is shown in Figure 6.5. It includes the Monte Carlo simulation results with the load-one detector simulation. The uncertainty in the load-one measurement includes the statistical uncertainty and the pion leakage correction uncertainty. The dominant uncertainty is caused by the poor statistics of the inspill pedestal data. The load-one module has better uniformity, therefore the uncertainty caused by the detector non-uniformity does not contribute to the load-one e/π ratio measurement.

6.4 Discussion

There are a few points I want to discuss regarding the Monte Carlo simulation and the load-two results.

1) Local hardening effect

With particle energy greater than 20 GeV, the Monte-Carlo simulation agrees well with the load-one BLS e/π ratio measurement[22], but the simulation shows a few percent (4%-6%) higher e/π ratio than the load-two BLS measurement. Furthermore, the

measured load-one e/π ratio is a few percent higher than load-two, and there is a discrepancy between the load-two Monte Carlo simulation and the beam data. There is evidence that this could be the result of a local hardening effect as I stated previously in Section 5.5, which is not well simulated by the current GEANT Monte Carlo. The local hardening effect is mostly caused by the suppression of the signal coming from the photo-electrons. These photo-electrons produced by soft γ's through the photo-electric effect have energies of 10's of keV or less with a very short range. GEANT Monte Carlo only tracks particles with energy above a cutoff energy (10 keV minimum), and particles with energy below the cutoff energy will deposit their energy locally. To give an example of this effect, Figures 6.7, 6.8, and 6.9 show the longitudinal energy distributions of 5 GeV electron showers in a few U/LAr gaps, with cutoff energies of 10 keV, 100 keV and 1.0 MeV.. The longitudinal energy distributions in all materials (U, LAr and G10), in LAr only and in G10 only are shown in these Figures. The spikes at the medium boundaries are artifacts of GEANT Monte Carlo, which stops particles near the medium boundaries and deposits their energies locally. In reality, some of this energy would be transported to the next medium. The relative size of the spikes increases with the cutoff energy, and even with a 10 keV cutoff energy, there are still spikes at each medium boundary. This indicates that GEANT Monte Carlo can not precisely simulate the very low energy phenomena near the medium surface.

The construction of load-two and load-one modules is essentially the same except for differences in the Uranium plate thicknesses between CCEM and ECEM (3mm in CCEM, and 4mm in ECEM) and the extra readout boards in the CCEM. Since the local hardening effect has not been simulated in the Monte Carlo, the Monte Carlo shows approximately the same e/π ratio for both load-one and load-two. This is an expected result[11] without the local hardening effect. However, the load-one modules have no G10 covered Uranium surfaces, so there is no local hardening effect, whereas the local

hardening effect in the load-two CCEM modules suppresses the load-two electron response. This results in a smaller load-two e/π ratio than in load-one. Figure 6.6 shows that after shifting up load-two ratio by 0.045[1] , the e/π ratio for load-two becomes similar to that for load-one.

2) The slow signal component in the hadron showers

The GEANT Monte Carlo provides time information of energy deposition. I have done simulations to study the difference of the energy deposition between a 200ns cutoff time and a 2.2 μs cutoff time in the 100 GeV pion shower. The Monte Carlo shows very little difference (< 1%) between the two cutoff times. The measurement of the e/π ratio difference between short and long integration readout shows about a 5% difference. Other experiments[29,30,31,31] show a similar effect indicating that there is a slow signal component in hadron showers. These results indicate that the GEANT Monte Carlo needs improvement in its hadron shower simulation, particularly the neutron-nucleus interaction simulation, because neutron-nucleus processes are the major contributors to the slow signal component. In recent years, other groups have made progress in improving the neutron-nucleus interaction simulation. They have shown the effect of the slow hadronic shower component[32].

6.5 Conclusions

This dissertation presents a systematic measurement of the e/π ratio difference at two different time scales. The final result indicates that there is a 5% difference in the e/π ratio between short (250ns) and long (2.2μs) integration time with beam energies ranging between 25 and 150 GeV. The estimated uncertainties on this measurement are 2.3%. Below 25 GeV however, the systematic uncertainty of the measurement

[1] It is the difference of the load-one and load-two electron responses that we believe to be caused by the local hardening effect

increases to 3%, and the measured difference decreases to 3%, making the difference measurement less significant. This measurement confirms the prediction from the theoretical analysis of hadronic shower processes[11,18] that there is a slow signal component in the hadron showers, and that the time scale of this slow signal component is approximately 1 μs. This measurement is an improvement on the previous experimental result of HELIOS[14], the only previous experiment using a Uranium-liquid Argon calorimeter, which show a 2% to 5% difference between different integration times and energies.

This analysis had to overcome difficulties with the fast calorimeter trigger electronics to achieve a systematic uncertainty sufficiently small for a meaningful measurement. With more data, the systematic uncertainty could be further reduced. The experience gained from this analysis benefits the commissioning of the D0 calorimeter trigger. This analysis shows a good agreement of the measured calorimeter energy resolution of the load-two data with the GEANT Monte Carlo simulation. It also shows a small discrepancy between the load-two data and the GEANT Monte Carlo simulation in the e/π ratio and ratio difference. This provides a guide to fine tune the Monte Carlo simulation.

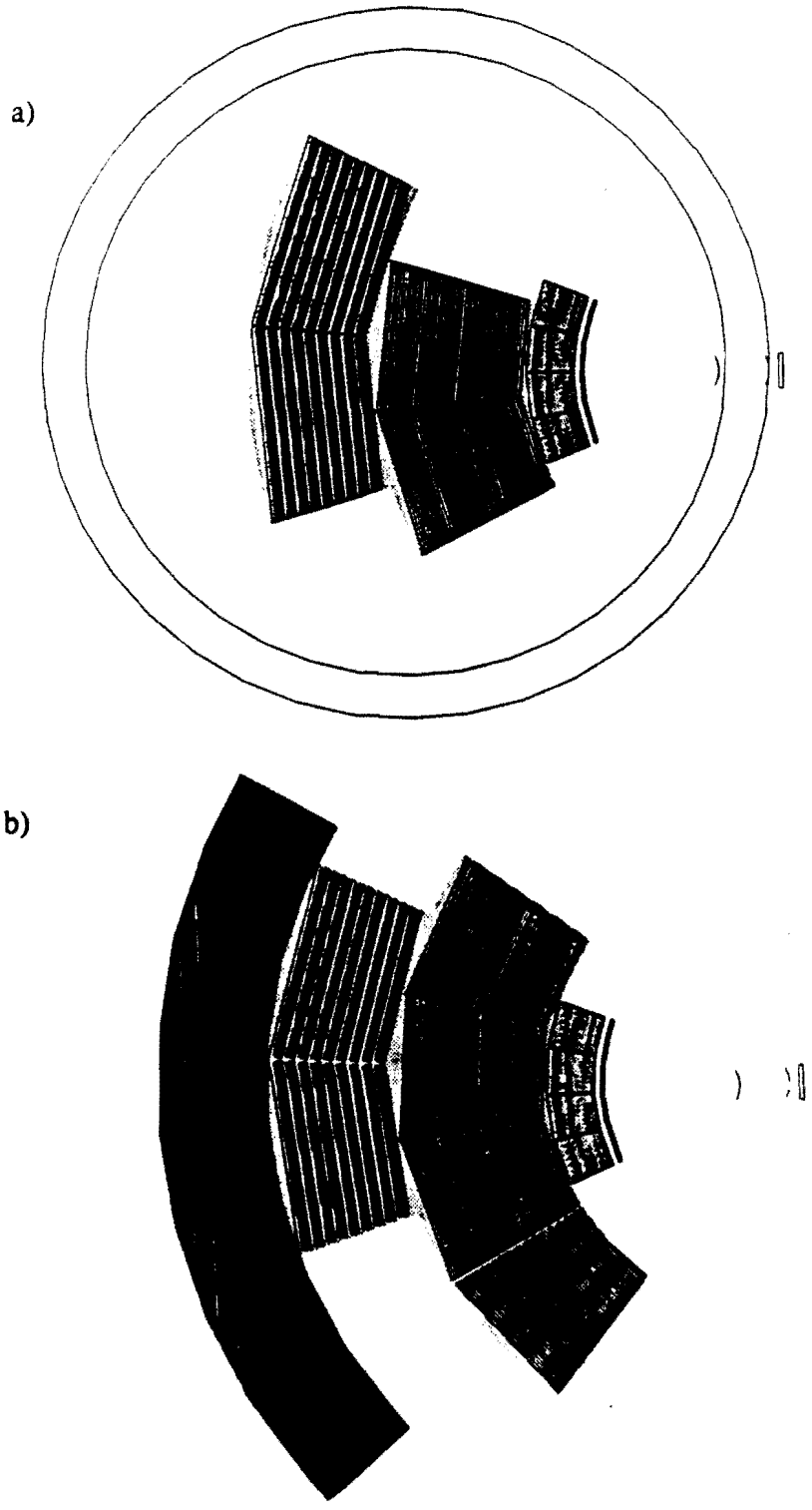

Figure 6.0 Geometry information for Monte-Carlo simulation of the load-two test beam. a) standard test beam configuration, b) with extra modules to study the pion shower leakage.

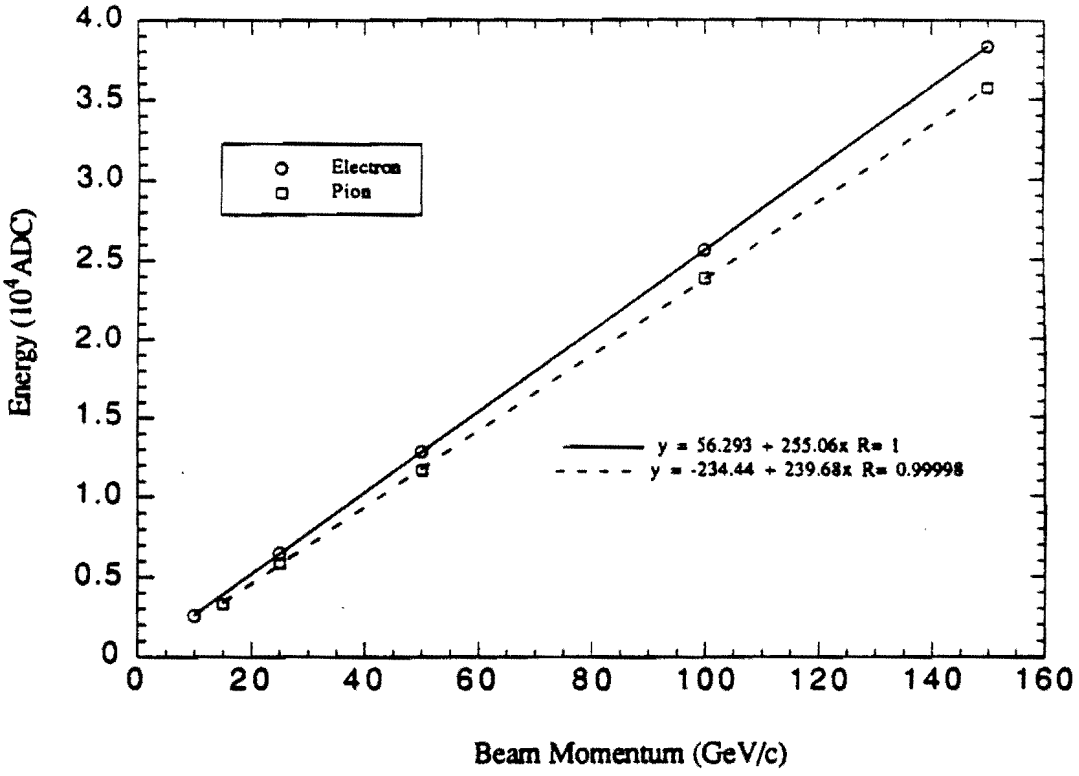

Figure 6.1 Monte Carlo simulation of the load-two electron and pion energy scan

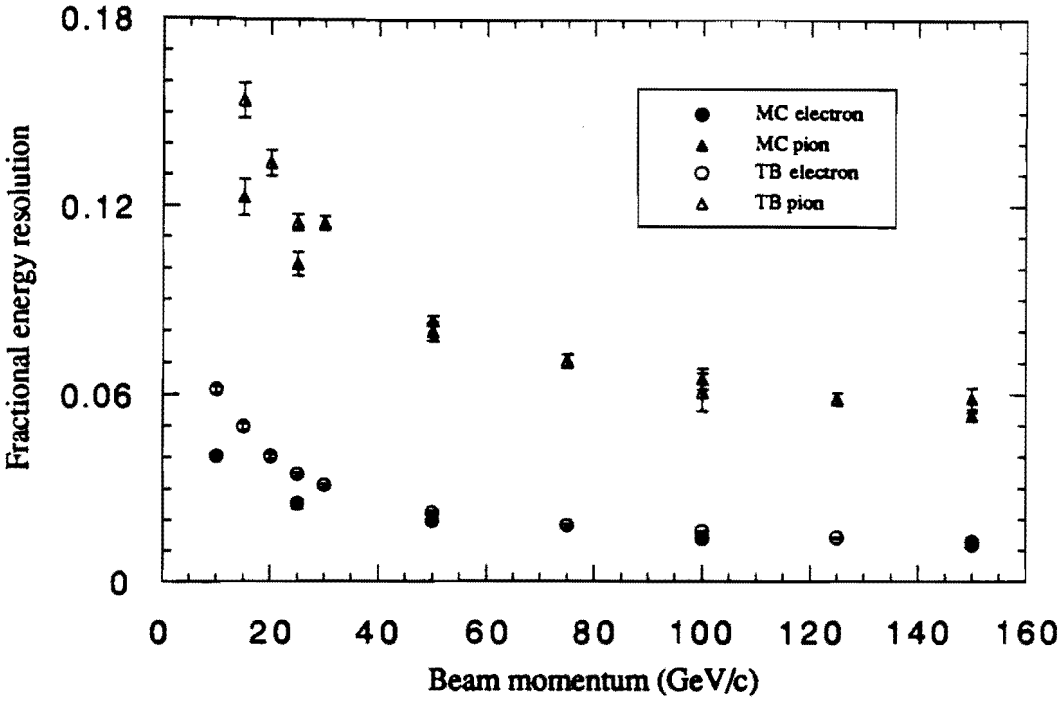

Figure 6.3a Monte Carlo and test beam data energy resolution comparision. No electronics noise in MC data

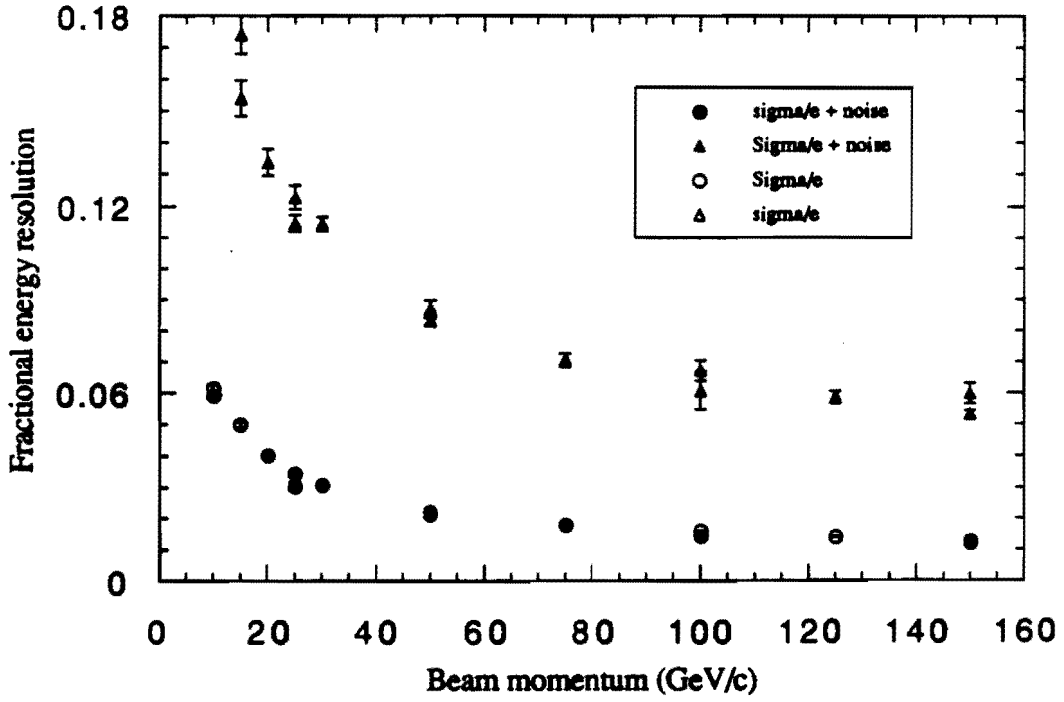

Figure 6.2b Monte Carlo and test beam data energy resolution comparison. Includes average electronics noise in Monte Carlo data

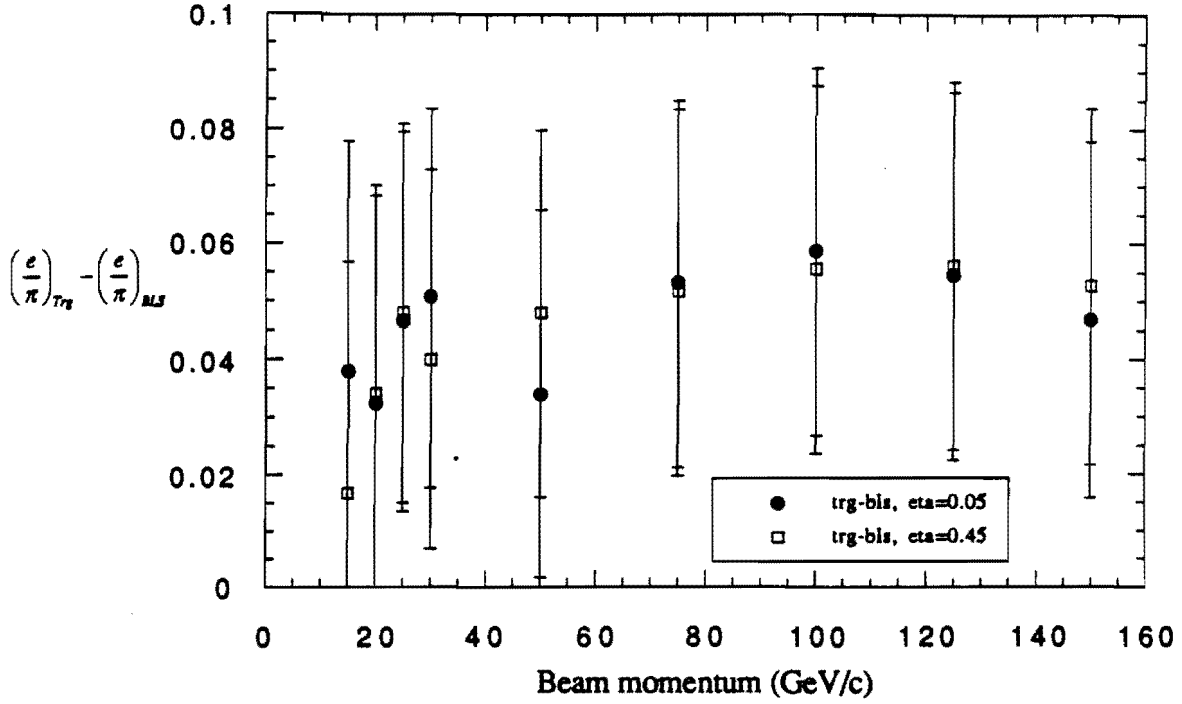

Figure 6.3a Electron/pion ratio difference between short (Trg) and long (BLS) integration times.

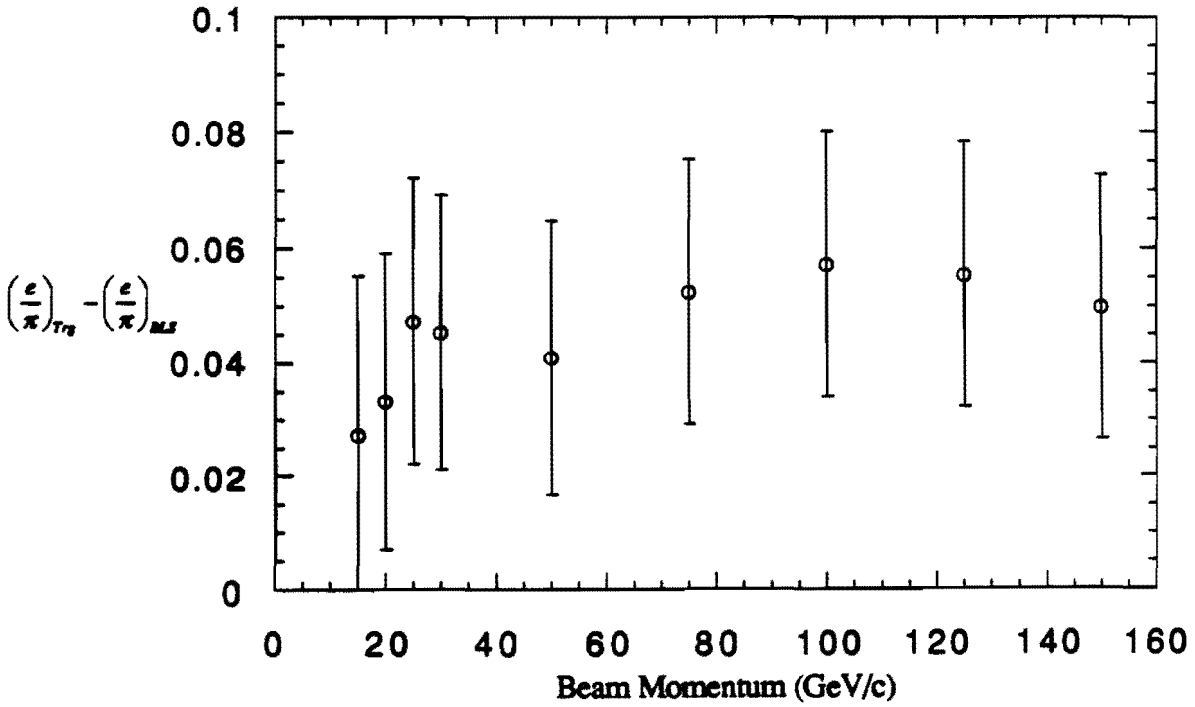

Figure 6.3b Average electron/pion ratio difference between short (Trg) and long (BLS) integration times.

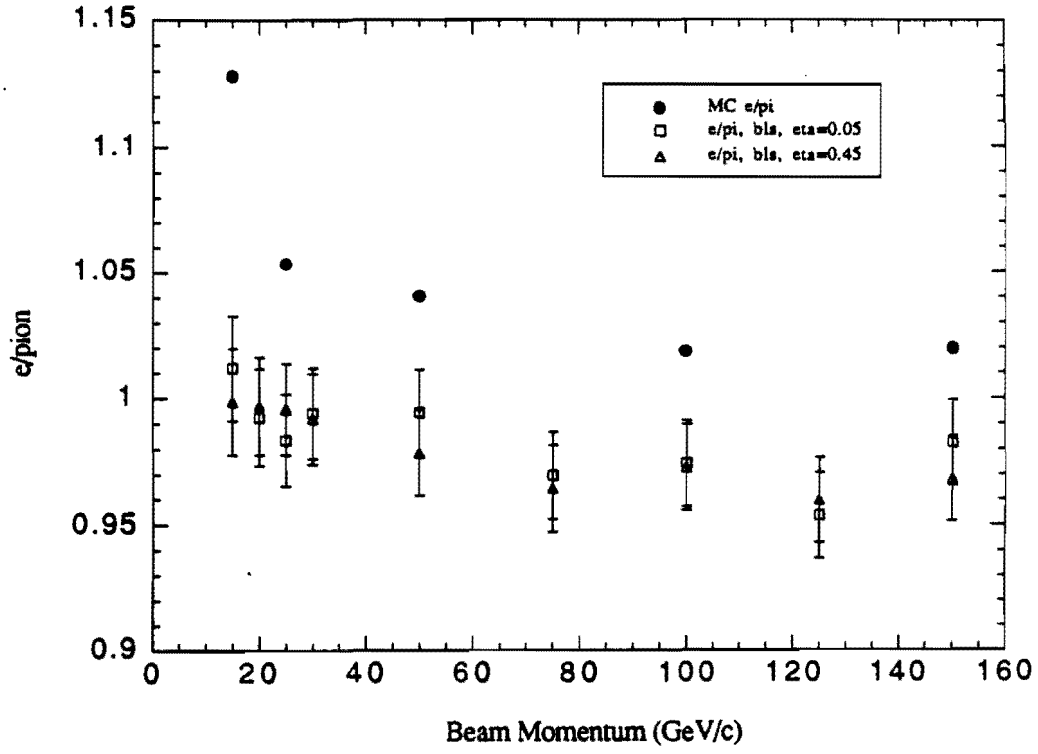

Figure 6.4 Load-two BLS electron/pion ratio.

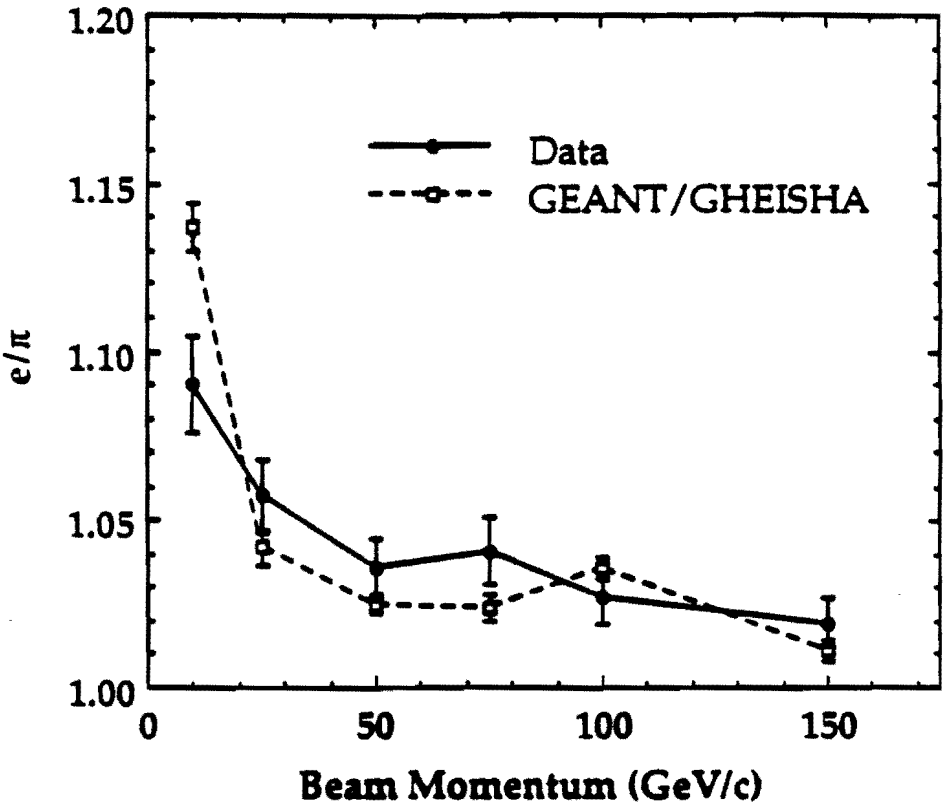

Figure 6.5 Load-one BLS e/π ratio.

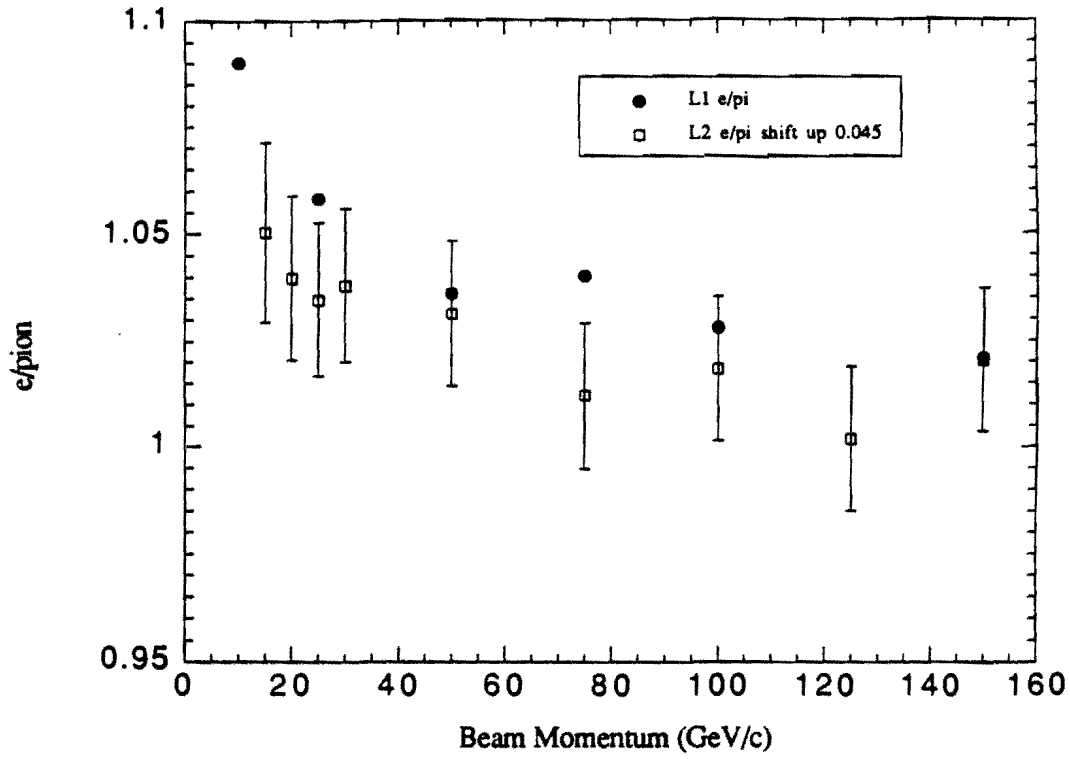

Figure 6.6 Load-one and load-two e/pion ratio comparison. Load-two result is the average of two sets of energy scan data shifted up by 0.045

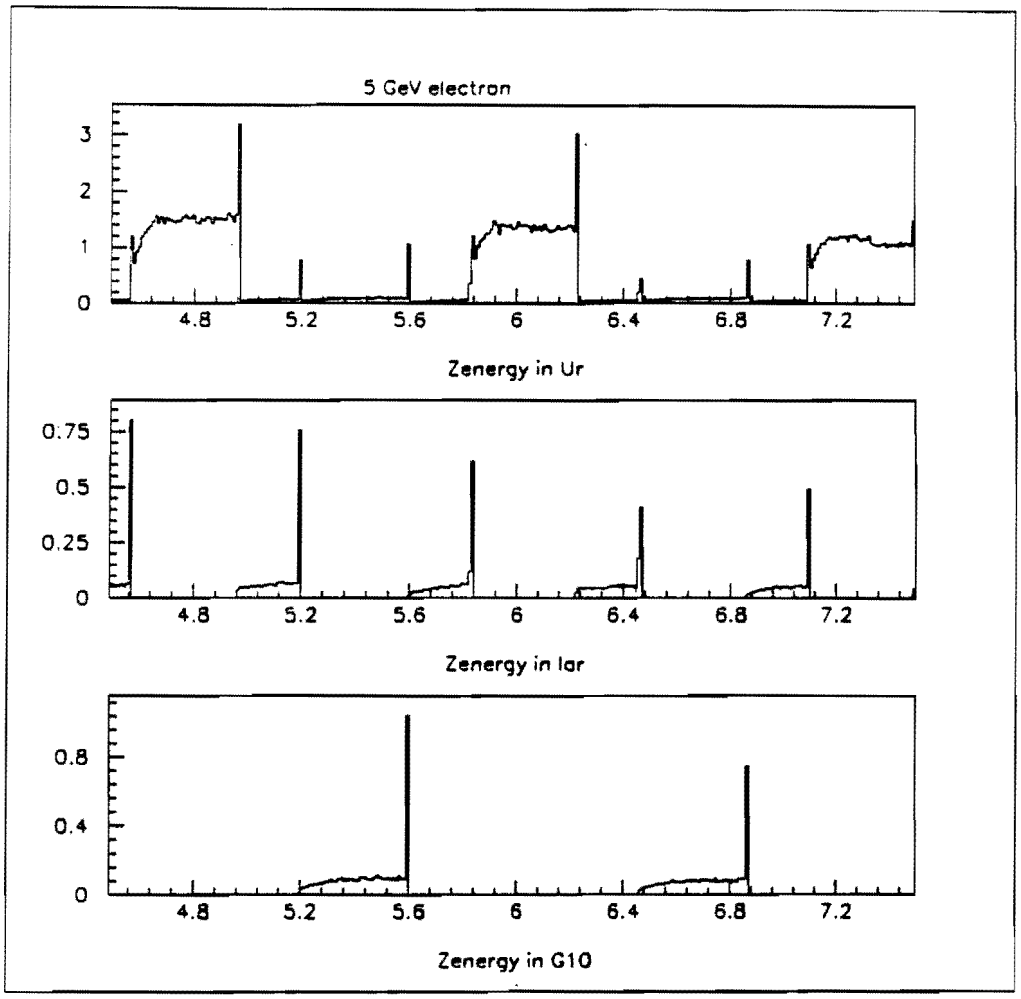

Figure 6.7 The longitudinal energy distribution of 5 GeV electrons in U/LAr gaps with 10 keV cutoff energy. The top is energy in all materials (U, LAr and G10), the middle is energy in LAr only, the bottom is energy in G10 only.

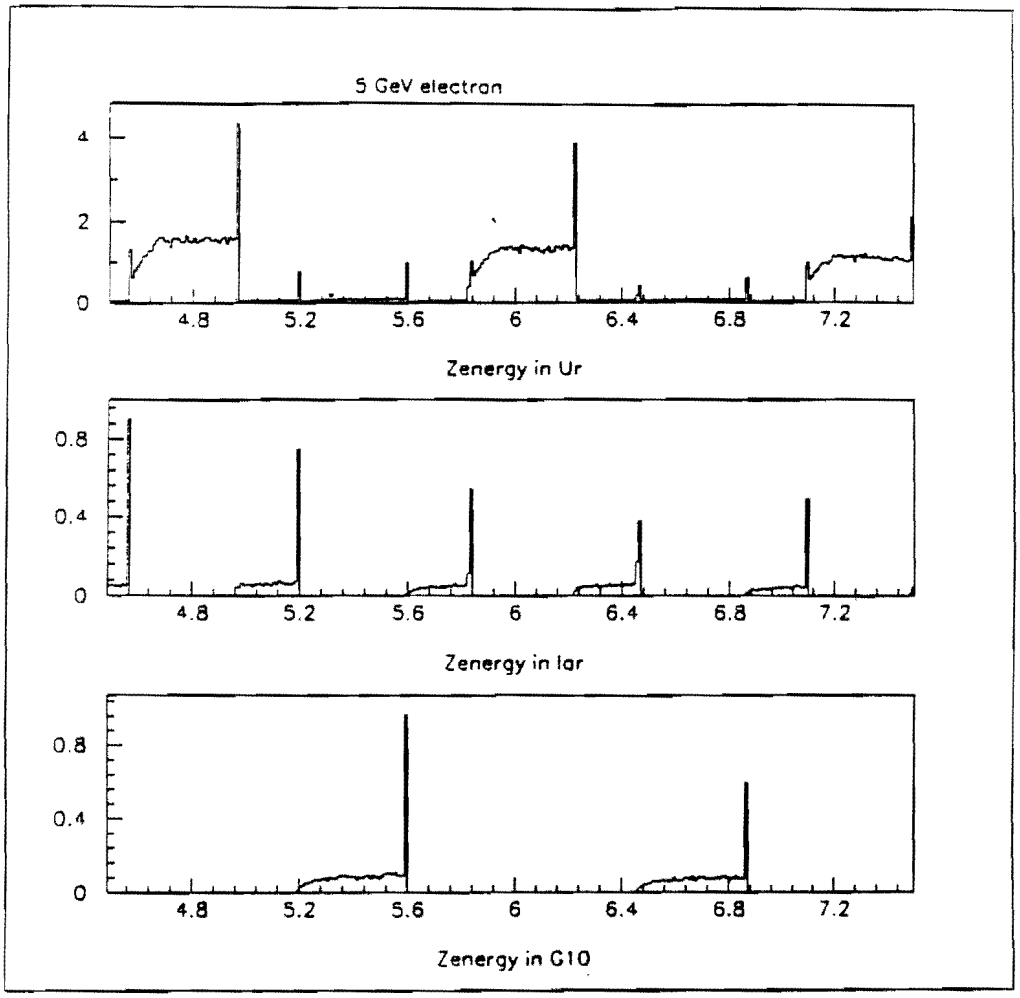

Figure 6.8 The longitudinal energy distribution of 5 GeV electrons in U/LAr gaps with 100 keV cutoff energy. The top is energy in all materials (U, LAr and G10), the middle is energy in LAr only, the bottom is energy in G10 only.

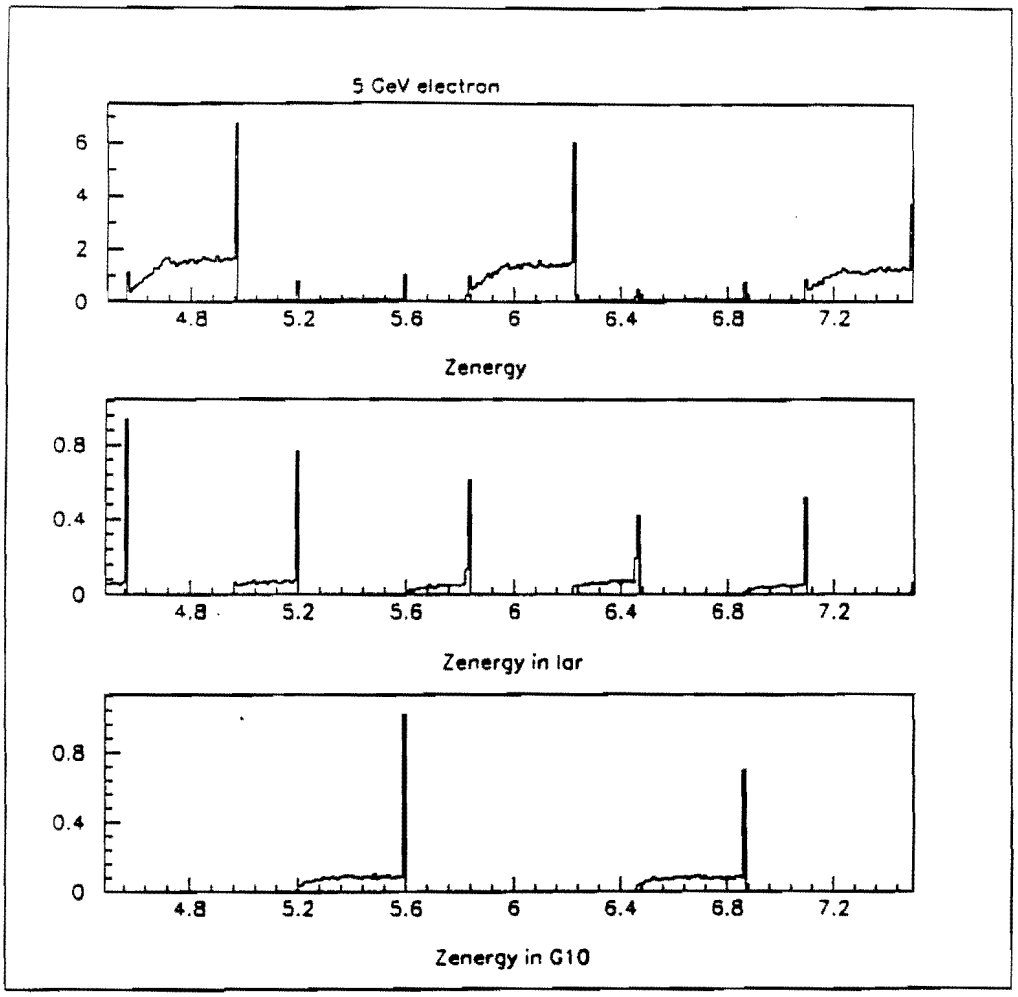

Figure 6.9 The longitudinal energy distribution of 5 GeV electrons in U/LAr gaps with 1.0 MeV cutoff energy. The top is energy in all materials (U, LAr and G10), the middle is energy in LAr only, the bottom is energy in G10 only.

Bibliography

[1] Fermi National Accelerator Laboratory. *Design Report Tevatron I Project.* Fermi National Accelerator Laboratory, September, 1984.

[2] M. Abolins, et al. *Design Report: the D0 experiment at the Fermilab Antiproton-proton Collider.* Fermi National Accelerator Laboratory, Nov., 1984.

[3] R. Brun, et al. *GEANT3.* CERN, DD/EE/84-1, Sept., 1987.

[4] R. R. Roy, et al. *Interaction of Photons and Leptons with Matter.* Academic Press, 1968.

[5] E. Merzbacher. *Quantum Mechanics.* John Wiley & Son, 2nd Edition, 1970.

[6] D. Schamberger, et al. *D0 Calorimeter Eectronics.* Nucl. Phys. B 23A, p191, 1991.

[7] T. L. Quarles. *SPICE3 Version 3C1 Users Guide.* UCB/ERL M89/46, April, 1989.

[8] C.W. Fabjan, et al. *Energy Measurement of Elementary Particles.* Rep. Prog. Phys., 52, p1519, 1989.

[9] R. Wigmans. *Advances in Hadron Calorimetery*. Annual Review of Nuclear and Particle Science, 41:133-85, 1991.

[10] R. Wigmans. *On the Energy Resolution of Uranium and Other Hadron Calorimeters*. Nucl. Instr. and Meth., A259, p389, 1987.

[11] R. Wigmans. *High Resolution Hadron Calorimetry*. Nucl. Instr. and Meth., A265, p273, 1988.

[12] R. Wigmans, et al. *An Experimental Study of the Contribution of Nuclear Fission to the Signal of Uranium Hadron Calorimeters*. Nucl. Instr. and Meth., A252, p4, 1986.

[13] V. Radeka, et al. *Speed and Noise Limits in Ionization Chamber Calorimeters*. Nucl. Instr. and Meth., A265, p228-242, 1988.

[14] B. Yu, et al. *A Uranium-Liquid Argon Calorimeter for Experiment NA34 (HELIOS) at the CERN SPS*. Chapter 1.4, p15, SSC Detector R&D at BNL, April 1990 Status Report. BNL 52244.

[15] SICAPO collaboration. *The Local Hardening Effect on Electromagnetic Showers: A Way for Signal Equalization in Si/High-Z Hadron Calorimeters*. Phys. Lett., B222, p518, 1989.

[16] M. Abolins, et al. *The Fast Trigger for the D0 Experiment*. Nucl. Instr. and Meth., A289, p543, 1990.

[17] M. Abolins, et al. *Hadron and Electron Response of Uranium Liquid Argon Calorimeter Modules for the D0 Detector*. Nucl. Instr. and Meth., A280, p36, 1989.

[18] H. Brueckmann, *Calculation of Hadronic Shower.* Proc. of Workshop on Compensated Calorimetry, Pasadena 1985, CALT-68-1305.

[19] C.W. Fabjan, et al. *Uranium Liquid Argon Calorimeter.* Nucl. Instr. and Meth., 141, p61, 1977.

[20] J. P. Richer, et al. *Cross Talk in Multielectrode Particle Detectors.* IEEE Trans. Nucl. Sci. NS-31, No 1, Feb., 1984.

[21] R. Hirosky. Private Conversation on the Analysis of D0 Liquid Argon Purity Test Cell Data and Calorimeter High Voltage Scan Data.

[22] M. Abolins, et al. *Hadron and Electron Response of D0 Uranium Liquid Argon End Calorimeter Modules.* Submitted to Nucl. Instr. and Meth.

[23] The EGS4 code system. SLAC Report 265.

[24] H. Fesefeldt. *GHEISHA: The Simulation of Hadronic Showers "- Physics and Application -".* PITHA 85/02.

[25] K. Hanssgen et al. *The Monte Carlo Code NUCRIN to Simulate Inelastic Hadron-Nucleon Interaction at Laboratory Energies Below 5 GeV.* Comp. Phys. Comm., 39, p53, 1986.

[26] D. Huffman. *Precision Calibration of Calorimeter Electronics in the D0 Liquid Argon/Uranium Particle Detector.* IEEE Nuclear Science Symposium, Nov 2-9, 1991.

[27] R, Angstadt, et al. *Modeling of the D0 Data Acquisition System.* IEEE Nuclear Science Symposium, Nov 2-9, 1991.

[28] W. Dharmaratna. Private Communication on the CC Uniformity Scan Data Analysis.

[29] M. DeVincenzi, et al. *Experimental Study of Uranium-Scintillator and Iron-Scintillator Calorimeter in the Energy Range 135-350 GeV.* Nucl. Instr. and Meth., A243, p348, 1986.

[30] M.G. Catanesi, et al. *Hadron, Electron and Muon Response of a Urnium-Scintillator Calorimeter.* Nucl. Instr. and Meth., A260, p43, 1987.

[31] T. Akesson, et al. *Performance of the Uranium/Plastic Scintillator Calorimeter for the HELIOS Experiment at CERN.* Nucl. Instr. and Meth., A262, p243, 1987.

[32] T. A. Gabriel, et al. *CALOR89: Calorimeter Analysis and Benchmarking.* Proceeding of the First International Conference on Calorimetry in High Energy Physics.

[33] Particle Data Group. *Review of Particle Properties, Passage of Particles Through Matter.* Phys. Lett. B239, pIII.13, April, 1990.